PhD Thesis

Inorganic–Organic Hybrid Nanocrystalline Materials in Zero to Three Dimensions

Subhojit Das

Department of Chemistry
Indian Institute of Technology Guwahati

September, 2013

Inorganic–Organic Hybrid Nanocrystalline Materials in Zero to Three Dimensions

A thesis submitted by

Subhojit Das
Roll No. 07612221

to

Indian Institute of Technology Guwahati

for the award of the degree of

Doctor of Philosophy

Department of Chemistry
Indian Institute of Technology Guwahati
Guwahati – 781 039
India

September, 2013

Statement

The work contained in this thesis, entitled, '**Inorganic–Organic Hybrid Nanocrystalline Materials in Zero to Three Dimensions**' has been carried out by me under the supervision of Dr. Arun Chattopadhyay, Professor and Head, Department of Chemistry, Indian Institute of Technology Guwahati. This work has not been submitted elsewhere for the award of any degree.

Subhojit Das

IIT Guwahati
September, 2013

Certificate

It is certified that the work contained in the thesis, entitled, '**Inorganic–Organic Hybrid Nanocrystalline Materials in Zero to Three Dimensions**' has been carried out by Subhojit Das, a student of the Department of Chemistry, Indian Institute of Technology Guwahati, for the award of the degree of Doctor of Philosophy under my supervision. This work has not been submitted elsewhere for any degree.

Arun Chattopadhyay

Professor and Head,
Department of Chemistry
IIT Guwahati
Guwahati – 781 039, India

September, 2013

Dedicated to my beloved parents

Late Mr. Himangshu Das
and
Mrs. Shipra Das

Acknowledgements

This space of the thesis is as essential as any other. It is imperative, at this point, that I express my heart-felt thanks and gratitude to all the people that have direct or indirect connect in lending their warmth and support during the course of my PhD studies and also being so quintessentially related to me in my ups and downs of life. May I also state that the names of those that are not been mentioned here, for space limitation, should not feel they are unimportant to me. They mean to me as much as others and I have immense respect for them too.

First of all, I would like to thank my supervisor, Prof. Arun Chattopadhyay for his guidance, support and advice throughout my doctoral studies. He lent me ample freedom to make creative and original thinking and this had helped nurture my own ideas of research. I am especially thankful to him for giving me all the opportunities to learn and operate sophisticated instruments that had helped in carrying out smoothly otherwise most arduous of the works. It was my privilege to have him as a mentor that I could share of his exceptional scientific knowledge and also of his human qualities. Virtues that I had imbibed from him will forever stay with me and be a cynosure in my every walk of life.

I express sincere thanks to my doctoral committee chairman Dr. Sandip Paul and other committee members Dr. Aiyagari Ramesh and Dr. Mohammad Qureshi for their periodic assessment of the findings of my research and their constructive suggestions that had helped a great deal in shaping the thesis in the present form. Thanks also to other faculty members of the department for their concern and motivation towards my endeavor.

The guidance of Prof. Siddhartha Sankar Ghosh and Dr. Anumita Paul during my collaborations with them are held at high esteem. I am so very indebted to Anumita Ma'am for her time and patience during my discussion sessions with her in working out the intricacies of a problem. In particular, I would like to thank her for the suggestions she made in reference to Chapter 3 of this thesis.

My hearty thanks to Dr. Devasish Choudhury of IASST, Guwahati. He had been like my teacher and friend in my initial years of research career. I have had the privilege of involving in collaborative works with him, and during which time I learned to operate scanning probe microscopes, for which I shall always be thankful to him. Genuine thanks also to Dr. Devashish Sengupta of Assam University, Silchar for his friendly help, advice and suggestion ever since I had known him.

Deepest thanks to all the staff members of the Department of Chemistry for their help in every which way. The staff members of the Centre for Nanotechnology and Central

Instruments Facility are highly acknowledged for lending help and cooperation whenever it was the need of the hour. My special thanks to Indrajit da, Kaustubh da, Kula da, Chandan da, and Madhurjya da for whom I could learn to operate the instruments needed for my research.

My thanks to the Sophisticated Analytical Instruments Facility (SAIF) at NEHU, Shillong for enabling me use instrumental facilities. Thanks also to the Department of Physics, IIT Guwahati (Mr. Bhargab Deka) for giving me access to make magnetic measurements of my samples.

I acknowledge CSIR, New Delhi for the PhD fellowship that had allowed me to undertake this research. I must also thank IITG (for its national funding) and DST, New Delhi (for providing the international travel support) for giving me the opportunity to attend conferences and also meet so many interesting people from different quarters of the world.

My stay in the lab of Prof. Chattopadhyay for 5 odd years was all the more a fun. Meeting many people, of different ages, with the same goals and ambitions as me made this journey very enjoyable. It was pleasant to have fellow mates as B. R. Panda, A. Murugadoss, Sonit Gogoi, Jashmini, Krishna, Sadhu, Raihana, Rumi, Palash, Satya, Sunil, Rama, Anushree, Shilaj, Uday, Sabyasachi, and Kafeel. The company of Dr. Sankar Moni Bora and Dr. Nirmala Devi was also pretty heartening. Frequent interactions with our other members and collaborators such as Shilpa, Amaresh, Upashi, Amit, Bandhan was equally amusing. Special thanks to Amaresh for his collaborations. I was blessed to have worked in the environ of such a diverse community that supported each other at all times.

Completing this work would have been all the more difficult were it not for the support and friendship provided by Francis, Pankaj, Sadhu, Atul, Chaitanya, Manish, Sandeep, Swamy, Rajesh, Ravi, Rajib, Mohan, Vijendra, Sakthivel, Himanshu, Moushumi, Anasuya, among others. I am indebted to them. Thank are also to my friends outside of IITG (Chanchal, Paritosh, Tamojit, Rajdeep, Sanjoy, Sudip, Salma, Biraj, Gautam, Bhaskar, Partho, Saurabh, Sajal, Barisha, Bijeta, Momo, and others) for their love and wishes throughout my studies.

Last, but not the least, thanks to my family members and relatives who have always been by me through thick and thin and for their help in ways not known to them. I owe sincere thanks for the selfless continued support and encouragement of my mother and elder brother toward my academic pursuit.

Subhojit

Contents

Chapter 1

Introduction

"*Small is beautiful*" is the topic of everyday speech, atleast in the scientific community, in the present days. But with the thrust of research activities being carried out and the plethora of articles published in the field of nanoscience and nanotechnology, it has been realized that "*small*" is not only beautiful but also *powerful*! The term "*small*" refers to here explicitly the objects that have at least one dimension less than or equal to 100 nm, which complies with the definition of nanomaterial (or nanoscale material) in general, and nanoparticle (NP) in particular. At this length scale the surface-to-volume ratio of a particle dramatically increases as the size of a crystal decreases to the nanometre regime, a phenomenon not observed in a bulk crystal. Interestingly, new properties are acquired by materials at the said scale and, equally important, that these properties change with their size and shape. These attributes make NPs ideal for use in a wide variety of areas like catalysis, biomedicine, optics, electronics, etc.

1.1. NANOPARTICLES

NPs are a number of atoms or molecules bonded together (usually contain ≤ 10^6 atoms) and are intermediate in size between individual atoms and bulk material [1, 2]. They, therefore, show behavior intermediate between that of a macroscopic solid and an atomic or molecular system. There are three major factors that are responsible for these differences: high surface-to-volume ratio [2–5], quantum size effect [6], and electrodynamic interactions [7]. It may be mentioned here that when all the three dimensions of a particle are confined in the nanometer size regime, it is referred as zero-dimensional (0D) NP, if two dimensions are confined it is one-dimensional (1D) nanomaterial, and if only one dimension is confined it is called two-dimensional (2D) nanomaterial. Finally, when all the three dimensions of a material (composed of NPs) extend beyond the nanometer size, the material is said to be three-dimensional (3D).

NPs encompass particles of various shapes such as spheres, rods, stars, plates, cubes, etc and that are made up of metals, oxides and sulphides of metals, organic molecules, and so on. Further, hybrid and alloyed NPs are also of relevance in the context of varying structures/shapes of NPs. These include core–shell type, and multiple shell type particles

and having final spherical as well as non-spherical shaped structures. These particles, individually, as well as in their core–shell architectures give rise to attractive chemical, optical, magnetic, electronic, and biochemical properties in the presence of light, magnetic field, electric potential and biological environments. Many applications (such as sensors, medical diagnostics, homogeneous catalysis, etc.) make use of the properties of the individual or core–shell NPs.

1.1.1. Metal Nanoparticles

Metallic NPs possess unique optical, electronic, chemical, and magnetic properties. The intrinsic properties of metal NPs are mainly governed by their size, shape, composition, crystallinity, and structure. In principle, one could control any one of these parameters to fine-tune the properties of NPs.

The physical origin of the light absorption by metal NPs is the coherent oscillation of the conduction band electrons induced by the interacting electromagnetic field (Scheme 1.1). An extinction band results when the incident photon frequency is resonant with the collective oscillation of the conduction band electrons and is known as the surface plasmon resonance (SPR). Coinage metal (Cu, Ag, Au) NPs, due to their d–d band transitions, exhibit strong SPR bands in the visible spectrum and are responsible for the deep colors, reminiscent of molecular dyes. For NPs of metals, such as, Pb, In, Hg, Sn, and Cd, the plasma frequency lies in the ultraviolet (UV) part of the spectrum and, therefore, they do not display strong color effects. Hence, surface plasmon experiments are most commonly carried out with Cu, Ag, and Au. The resonance frequency of this SPR is strongly dependent upon the size, shape, interparticle interactions, dielectric properties, and local environment of the NP [8–13].

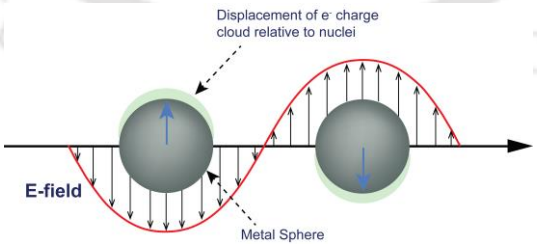

Scheme 1.1. Representation of plasmon oscillation on a metal sphere in the presence of an electromagnetic radiation.

Nanometre-scale metal particles exhibit optical properties of great aesthetic, technological, and intellectual value [14]. Because they show characteristic colors,

colloidal solutions of Cu, Ag, and Au have received considerable attention in the recent times.

1.1.1.a. Gold nanoparticles

Due to their unique optical, electronic, and molecular-recognition properties, Au NPs have been the subject of intense interest over the last couple of decades. Colloidal Au, however, is not the subject of the present time. It gained the interests of mankind since antiquity. Though the extraction of metallic Au started in the 5th millennium B.C. (in Bulgaria), "soluble" Au appeared around the 5th century B.C. in Egypt and China [15]. In the mid 17th century, Andreus Cassius's preparation of the "Purple of Cassius" was widely used as a pigment in enamel, chinaware and silk fabric as well as in glass. The most famous example of the early use of metal NPs embedded in glass is the Lycurgus Cup from the 5th century B. C. [16]. It appears green in day light (reflected light), but red when it is illuminated from the inside (transmitted light). Until the Middle Ages, the soluble form of Au was used for curative purposes for various diseases. In all such preparations, the brilliant colour was due to the presence of Au NPs. This fact was, however, not recognized until the work of Michael Faraday in 1857 [17].

The synthesis of colloidal Au dates back to Faraday's work [17], wherein he reported the formation of a deep red solution of colloidal Au by reduction of an aqueous solution of chloroaurate ($AuCl_4^-$) using phosphorus in CS_2. In 1908, Gustav Mie came forward to explain the red color of the Au NPs in solution [18] by solving Maxwell's equations [19, 20]. Rayleigh originally solved the problem for a sphere smaller than the wavelength of light; thereafter Mie made a solution to the problem for a sphere of a size comparable to the wavelength [21–23]. Later in 1951, Turkevich developed one of the most popular approaches for the synthesis of Au NPs, using citrate reduction of chloroauric acid ($HAuCl_4$) in water [24, 25]. Further studies by G. Frens enabled control over Au NPs' size by varying the feed ratio of $HAuCl_4$ to sodium citrate [26]. After Mulvaney's initial attempt of stabilizing Au NPs with alkanethiols [27], a breakthrough in the field of Au NP synthesis was achieved by Brust and Schiffrin in 1994 [28]. They reported a two-phase synthetic strategy utilizing strong thiol–Au interactions to generate Au NPs, of size 1.5–5 nm, that display enhanced stability.

Among all the metals, the optical properties of Au NPs have been most extensively studied [29–31]. NPs of Au having ruby red color show strong absorption of green light at about 520 nm [2, 32], corresponding to the frequency at which a plasmon resonance occurs with the Au. The strong extinction of light by Au NPs, compared to conventionally used dyes, has been due to their high molar extinction coefficient. For instance, Au NPs

with a diameter of 40 nm have a molar extinction coefficient (ε) of 7.66×10^9 M^{-1} cm^{-1} at λ_{max} 528 nm. This value is much larger than that of the strongly absorbing dyes, such as the likes of indocyanine green (ε= 1.08×10^4 M^{-1} cm^{-1} at 778 nm) [33], rhodamine-6G (ε= 1.16×10^5 M^{-1} cm^{-1} at 530 nm) [34], and malachite green (ε= 1.49×10^5 M^{-1} cm^{-1} at 617 nm) [34].

The properties and applications of Au NPs strongly depend upon their size and shape. For example, Au nanorods (NRs) have two resonances: one along the short axis (transverse mode) and the other along the long axis (longitudinal mode) [35–37]. In many biological applications the near-infrared (NIR) region of the spectrum (~ 650–900 nm) is ideal for the fact that tissue, blood, and water are transparent in this window [38]. For such cases, Au NRs prove to be wondrous for tuning the localized SPR (LSPR) as their longitudinal resonance can shift from the visible to the NIR region, depending on the aspect ratio of NRs. An important aspect of Au NPs has been the breadth of their impact; applications range from photonic device fabrications, to sensing of organic and biomolecules, to charge storage systems.

1.1.1.b. Silver nanoparticles

In the first half of the 20th century, scientific interest in metal NPs was not limited to their optical properties. For example, Au NP dispersions were model systems for the study of colloidal stability and nucleation [39]. The application of colloidal Ag particles was also the subject of study before the advent of sulfa drugs in the 1930s [40].

Ag NPs are known to be the most important material in plasmonics. They offer many advantages over Au, Cu, Li, and Al – other metals that support surface plasmons in the visible and NIR regions [41, 42]. This is because Ag NP is able to support a strong surface plasmon across the spectrum from 300 to 1200 nm [43, 44].

In the case of Ag NPs, the first synthetic methods described were the Lee–Meisel method [45] and the Creighton method [46]. The former consists of a modification of the Turkevich method for the synthesis of Au NPs, using $AgNO_3$ instead of $HAuCl_4$ as metallic precursor and sodium citrate as the reducing agent. In this method the obtained NPs display a broad size distribution. The Creighton method, on the other hand, consists of the reduction of $AgNO_3$ with $NaBH_4$ as the reducing agent. By this method, Ag NPs of ca. 10 nm with a narrow size distribution can be generated.

Among the commercially available nano-sized materials, Ag NPs are by far the most used nanocompounds [47] owing to their potent antimicrobial activity [48]. Indeed, Ag NPs have been used in commercial products such as personal care, household and medical products, as well in textiles and food production [49, 50].

1.1.2. Magnetic Nanoparticles

Magnetic NPs (including MFe_2O_4, Fe, Co, Ni, etc) are a class of NPs which can be manipulated using magnetic field. Such NPs have a large constant magnetic moment and behave like a giant paramagnetic atom with a fast response to applied magnetic fields with negligible remnance and coercivity. In the size range from 1 to 100 nm the NPs become superparamagnetic [51] which prevents them from self-agglomeration, since they exhibit their magnetic behavior only when an external magnetic field is applied. With the external magnetic field switched off, the remnance falls back to zero [52].

The ferrite colloids, magnetite (Fe_3O_4: $[Fe^{3+}]_{Td}[Fe^{3+}Fe^{2+}]_{Oh}O_4$) and its oxidized form maghemite (γ-Fe_2O_3: $0.75[Fe^{3+}]_{Td}[Fe^{3+}{}_{5/3}V_{1/3}]_{Oh}O_4$), are the main representatives of the magnetic NPs. They are characterized by a spinel crystal structure with oxygen ions forming a close-packed cubic lattice and Fe ions located at the interstices [53]. The magnetization of Fe_3O_4 arises from antiferromagnetic coupling (superexchange through oxygens) between the Fe^{3+} ions in octahedral and tetrahedral interstices, leaving the magnetic moments of the Fe^{2+} ions (in octahedral positions) as responsible for the magnetization of the unit cell [54].

In most applications, the particles are deemed to perform best when their size is typically around 10–20 nm. Each NP then becomes a single magnetic domain and shows superparamagnetic behavior when the temperature is above the blocking temperature, T_B. These features make the NPs very attractive for a broad range of biomedical applications. For example, stable NP dispersions find applications in site specific treatments such as targeted drug delivery, localized heating of cancerous cells (hyperthermia), and magnetic resonance imaging (MRI) contrast enhancement [53, 55–57]. In the field of disease therapy, the development of “theranostics,” which facilitates simultaneous drug delivery and imaging, represents an important breakthrough of magnetic NP technology [58]. Other potential uses of magnetic NPs include catalysis [59], data storage [60, 61], environmental remediation [62], nanofluids [63, 64], and optical filters [65].

Most of the above applications require coating of the NPs by long chain molecules, such as long-chain fatty acids, alkyl-substituted amines and diols. Further, coating of Fe oxide NPs with inorganic materials, like silica [66, 67], Au [68], etc., provide enhanced stability to the NPs in solution. These coatings also help in binding various biological ligands to the NP surface.

1.1.3. Organic Nanoparticles

NPs forming of complex organic molecule, which, in addition to carbon and hydrogen, include atoms of oxygen, sulfur, halogens play a major role in biochemistry and

nanomedicine.

The methods for the preparation and physicochemical properties of NPs containing complex organic molecules are studied to an insufficient extent, as compared to the inorganic NPs such as semiconductor nanocrystals (NCs), metal NPs, etc. The fact that the development of studies of organic NPs, contrary to that of metal and semiconductor NPs, has started only relatively recently can be explained by the following two main reasons. First, low melting temperatures and lesser thermal stability of organic nanostructures as compared with those of inorganic compounds limit the methods for their synthesis and applications. Second, it was believed that no size effect is manifested in organic nanomaterials. However, it was found that the organic NPs do exhibit size dependence of physicochemical (especially, spectral) properties. Unlike metal and semiconductor NPs that exhibit size effects typically in the size range < 10 nm, for organic NPs the size effects were found with the sizes from several tens to several hundreds of nanometers [69].

In organic molecules, as the electrons are part of chemical bonds, the mobility of these electrons is limited. Hence, the interactions that result in spontaneous formation of ensembles and favour the charge transfer are relatively weak. A substantial difference in the optical and electronic properties of organic nanomaterials from the properties of nanomaterials of inorganic substances is associated with the presence in the former of weak intermolecular interactions, viz., van der Waals forces and $\pi - \pi$-conjugation. The interactions between the constituent moieties in organic NPs are, therefore, termed as 'soft' interactions [70–74]. The optoelectronic properties of the NPs are governed by the charge transfer excitons and the Frenkel excitons with small radii [70–72, 75], with striking difference from that of Mie scattering in case of metal NPs [18, 76, 77] or Mott–Wannier type excitonic charge separation observed in semiconductor NCs [78, 79].

Owing to their thermal instability, fabrication of organic NCs has received little attention. A few reports could be found on nanocrystallization of thermally stable phthalocyanine and other low molecular weight aromatic compounds, by methods involving evaporation in an inert gas [80] or by crystal growth technique in a porous polymer [81]. However, the simplest and the convenient method for the fabrication of organic NCs is the reprecipitation method [82], which employs the difference in the solubilities of the target organic compound in two solvents. By this method, NCs of polydiacetylene [83], phthalocyanine [84], perylene [85], among others, have been generated. Apart from investigation of fundamental optoelectronic properties of organic NCs, their physiochemical properties and other advantages have been extended to the fields of nanomedicine and biophotonics.

1.1.4. Core–shell Nanoparticles

Based on single or multiple materials, NPs can be categorized into simple and core–shell or composite NPs. In general, simple NPs are made from a single material; whereas, as the name implies, core–shell particles are composed of two or more materials. The core–shell type NPs can be broadly defined as comprising a core (inner material) and a shell (outer layer material). The core or shell materials in a core–shell particle are either made of inorganic or organic materials. These can consist of a wide range of different combinations [86], including inorganic–inorganic [87–91], inorganic–organic [92–98], organic–inorganic [99–111], and organic–organic [112–116] materials. The choice of shell material of the core–shell NP is generally dependent on the end application and use.

Core–shell NPs are highly functional materials with modified properties. Sometimes the properties arising from either core or shell materials are quite different. The properties can be modified by changing either the constituting materials or the core to shell ratio [117]. Because of the shell material coating, the properties of the core particle such as reactivity decrease or thermal stability can be modified, so that the overall particle stability and dispersibility of the core particle increases. The particles eventually show distinctive properties of the different materials used together. This is especially true of the inherent ability to manipulate the surface functions to meet the diverse application requirements [118, 119]. Further, the occurrence of the well-known Fano resonance has been demonstrated using metal NP core–shell structures with a silica spacer layer in between [120].

The purpose of the coating on the core particle are many-fold, such as surface modification, the ability to increase the functionality, stability, and dispersibility, controlled release of the core, making the particles less cytotoxic, reduction in consumption of precious materials, and so on. In addition to the improved material properties, core–shell NPs are also important from an economic point of view. A precious material can be coated over an inexpensive material to reduce the consumption of the precious material, as compared with making the same sized pure material.

Core–shell NPs are widely used in different applications such as biomedical [121–124] and pharmaceutical applications [119], catalysis [99, 118], electronics [125, 126], enhancing photoluminescence [127–129], creating photonic crystals [130], etc. In particular in the biomedical field, the majority of these particles are used for bioimaging [97, 123, 131–136], controlled drug release [136, 137], targeted drug delivery [97, 123, 136–138], cell labeling [123, 139, 140], and tissue engineering applications [94, 137].

1.2. INORGANIC–ORGANIC HYBRIDS

Although most colloids are either inorganic or organic in nature, colloidal systems can also be composed of both inorganic and organic constituents. Inorganic–organic hybrid particles can be defined as colloidal particles that contain both inorganic and organic domains. Such materials are not simply physical mixtures. They can be broadly defined as molecular or nanocomposites with organic and inorganic components, intimately mixed where at least one of the components has a dimension ranging from a few Angstrom to several nanometres [141]. A more detailed definition of hybrid materials distinguishes them into two classes, based on the possible interactions between the inorganic and organic species. Class I hybrid materials are those that show weak interactions between the two phases, such as van der Waals, hydrogen bonding or weak electrostatic interactions. Class II hybrid materials are those that show strong chemical interactions between the components [141].

Interests in inorganic–organic hybrids mainly arise as they can favorably combine the often dissimilar properties of inorganic and organic components in one material. By combining the two materials, it appears possible to achieve a unique combination of properties and obtain totally new synergistic behaviors. Examples are the incorporation of inorganic clusters or NPs with specific optical, electronic or magnetic properties in organic matrices. For example, Mann and co-workers [142, 143] have demonstrated that metallization of lysozyme protein crystals, which were cross-linked with glutaraldehyde, with Au or Ag resulted in an extremely well-ordered array of plasmonic NRs. Using the Au-lysozyme hybrid crystals as catalyst, Lu's group successfully carried out the catalytic reduction of *p*-nitrophenol to *p*-aminophenol [144]. On the other hand, Falkner et al. [145] reported the use of scaffolds of cowpea mosaic virus crystals for the generation of ordered arrays of Pt and Pd. Further, systematic organizations of the inorganic NPs in 3D, being held together by the organic moieties, provide additional properties that are absent in ordinary solid solutions. Sada and co-workers [146] have shown that Au NPs when preferentially deposited on the hexagonal faces of L-cystine crystals provide anisotropic optical property to the crystals. They have also been successful in depositing Pd complex NCs onto the specific crystal faces of organic compounds bearing pyridine moieties [147].

Another driving force in the area of hybrid materials is the possibility to create multifunctional materials. The inorganic–organic hybrid particles with diameters ranging from 10 nm up to several 100 nm are an important class of hybrid materials with potential applications in a variety of domains ranging from the encapsulation and controlled release of active substances to their utilization as fillers for the paint and coating industries. The incorporation of inorganic fillers into polymers contributes to a significant

improvement of the thermal and mechanical properties of the resulting composite material. An interesting example is that of the incorporation of Au NPs in perylene single crystals and encapsulation of the resulting hybrid crystals with polyaniline [148]. Report also exists on the dispersion of Au NPs in polystyrene polymer matrix [149]. Growth of NPs of CdS within a conducting metallopolymer to generate hybrid electronic material is also documented [150].

Inorganic–organic hybrid materials not only represent a creative alternative for the design of new materials and compounds for research, but their improved and unusual features open promising applications in diverse areas, viz., optics, electronics, ionics, mechanics, energy, environment, biology and medicine.

1.3. SUPERSTRUCTURES OF NANOPARTICLES

Synthesis of metallic [151–153], semiconductor [154, 155] and magnetic [156, 157] NPs with different functionalities has been demonstrated by various research groups. For researchers, once the NPs are fabricated the most important and challenging part left is the organization of NPs at the nanoscale level in an ordered manner for the desired applications. The ligand present as a stabilizer on the NPs provides the opportunity for the nanocomponents to interact with each other or target other moieties for the assembly processes. NP assemblies are classified into three main categories: 1D, 2D and 3D structures (Scheme 1.2). The 1D assemblies include chains of NPs [158–161], 2D assemblies of NPs lead to the formation of sheets [162, 163], vesicles [161, 164, 165], and 3D assemblies into crystals [166–169] or more complex 3D architectures [170].

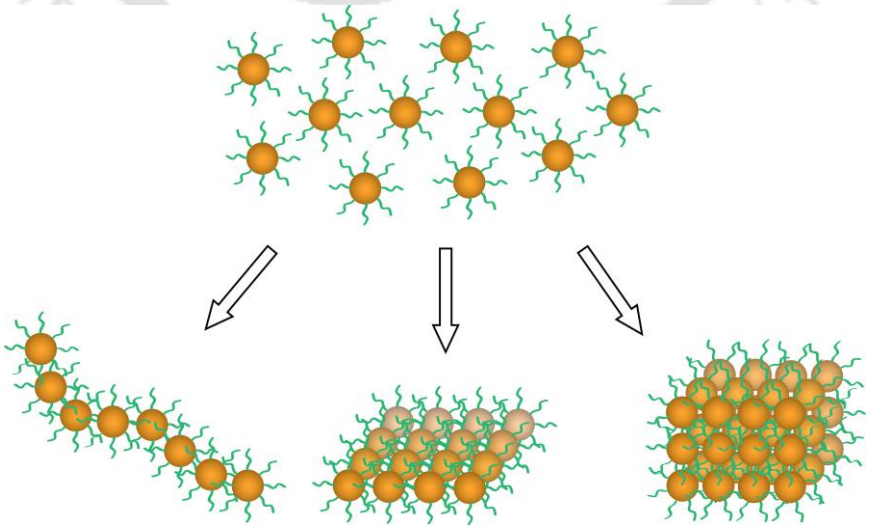

Scheme 1.2. Cartoon showing the organization of NPs in 1D, 2D and 3D superstructures.

Interest in ensembles of NPs arises primarily due to their collective properties and the possibility of using these properties in functional devices. In addition to improving the mechanical properties of composite materials, ensembles of NPs can also display new electronic, magnetic and optical properties as a result of interactions between the excitons, magnetic moments or surface plasmons of individual NPs. It should be possible to exploit these properties in devices, and also the directionality and long-range order found in ensembles, if the spacing and alignment of individual NPs can be controlled.

Self-assembly is a simple route for producing ensembles of NPs in a controllable manner. Self-assembly is the process in which the components of a system, such as molecules, polymers, colloids, or macroscopic particles, organize into ordered functional structures. The self-assembly of particles having a diameter of a few nanometres (< 10 nm) was initially reported by Bawendi's and Pileni's groups [171, 172]. Later, several groups demonstrated that a rather large number of NCs were locally ordered [173–180].

1.3.1. Strategies for Self-Assembly

Assembly of NPs can be achieved following strategies such as simple solution phase self-assembly, self-assembly using templates, self-assembly at interfaces, and field-assisted self-assembly.

1.3.1.a. Self-assembly in solution

In solutions the assembly of NPs is governed by the balance of attractive as well as repulsive forces. Attractive forces include covalent or hydrogen bonding, electrostatic attraction between oppositely charged ligands, depletion forces or dipole–dipole interactions, whereas repulsive forces are steric forces and electrostatic repulsion between ligands of like charge [181].

The 1D assembly of metal NPs can be achieved by manipulating the ligand interaction by introducing simple molecules as linkers [182–188], using block copolymer [161] or by triggering sphere-to-string miceller transition [159]. 2D arrays [189], aggregates [190, 191], assemblies using block copolymers [161], and other superlattices [163, 165, 192] leading to micelles and vesicles have been well studied. A body of works on 3D superlattices involves NP crystals that have been generated by means of tactically functionalizing NPs during synthesis [169, 193–197], by manipulating the crystallization conditions [198] and so on.

One of the simple approaches to solution-based self-assembly exploits site-specific interactions of chemically heterogeneous NPs [161, 199]. For instance, end-by-end or side-by-side assembly of Au NRs have been materialized by enabling attraction between

the distinct ligands attached to the long and short facets of the NR [161, 200–202]. Self-assembly of NRs have also been driven by surfactants [203, 204], DNA molecules [205], and their preferential end-to-end assembly using biotin-streptavidin connectors [158] have been demonstrated.

Chemical heterogeneity of NPs was also brought about by means of phase separation between 'immiscible' organic ligands [160, 206] or by consecutive attachment of different ligands [199, 207]. A classic example in this context is the phase separation in a mixture of nonanoic acid and 4-phenylbutyric acid, which produces two distinct singularities on the surface of γ-Fe_2O_3 NPs. This allows for the subsequent reaction with the molecular linker and the formation of NP chains [206].

Kotov and co-workers [162] demonstrated the spontaneous formation of close-packed 2D sheets of CdTe NPs. They reasoned that combined interplay between the directional hydrophobic attraction and anisotropic electrostatic interactions was the driving force leading to such structures. Previously, they have also reported on dipole-dipole attraction forces as being responsible for the organization of CdTe NPs into nanowires (NWs) [208]. The interaction was mediated by initial depletion of ligand shell surrounding the NPs, followed by attraction between the NPs – a method which forms the basis for the generation of NP superstructures of several types of NPs [204, 209].

On the other hand, 3D superlattices of NPs, made of several layers to form what is called as *supracrystals*, have been obtained for Au [193], Ag [210–212], CdSe [171, 213], Co [214, 215], In_2O_3 [216], PbSe, Fe_2O_3 [217] and Fe_3O_4 [218, 219] NPs. An elegant approach toward growing colloidal crytsals deserves mentioning of the work of Grzybowski and co-workers [166]. They reported the use of oppositely charged Au and Ag NPs for the formation of well-defined crystals with diamond-like structure. Crystallization of NPs was achieved by screening electrostatic interactions, such that the NPs interacted by short-range potentials. Engineering the interaction between DNA molecules, such as hybridizing complementary DNA molecules attached to the NP surface, lead not only to the formation of linear NP assemblies or simply aggregates [185, 189, 220, 221] but also enable the formation of 3D NP crystals with either face-centred cubic (*fcc*) or body-centred cubic (*bcc*) lattice structures [167, 168]. Colloidal crystals of oppositely charged polymethylmethacrylate (PMMA) and silica particles is also being reported [222]. A recent report demonstrates the growth of 3D Ag NP crystals in the form of lamellar structured Ag nanoleaves derived from Ag NPs with *p*-aminothiophenol as mediator [223].

1.3.1.b. Self-assembly using templating methods

Self-assembly of NPs on templates lead to geometries that are complementary to those of the templates. A range of objects including simple molecules [224, 225], carbon nanotubes (CNTs) [226], block-copolymers [227, 228], viruses [229] or DNA molecules [230, 231] have been used as templates for organization of NPs [185, 189, 232]. It is believed that strong interactions between a template and NPs is the driver for the arrangement of NPs in structures predefined by the shape of the template.

Hard templates, such as functionalized CNTs or inorganic NWs, offer well-defined shapes for NP assembly [226, 233, 234]. Chains of anionic poly(vinylpyrrolidone)-functionalized Au NRs have been constructed by depositing the NRs on the surface of cationic poly(diallyldimethyl ammonium chloride)-coated nanotubes [226].

In contrast to hard templates, soft templates possess distinct chemical structures, and provide multiple binding sites for the attachment of NPs. Synthetic polymers [227], proteins [235, 236], DNA molecules [230, 231] or viruses [229] are classified as soft templates. An interesting peptide-based synthesis and assembly of Au NPs into double-helical structures is worth mentioning here [237]. Again, DNA-guided NP assemblies prove to be very promising, in that DNA molecules have structural diversity, well-defined sequences and varied functionalities [238]. Several groups have reported the use of DNA scaffolds for controllable organization of NPs of Au [231, 239, 240], Ag [241, 242], CdSe and CdSe@ZnS [243], as well as for the syntheses of CdS NWs [244] and metal NPs aligned in chains [241]. Report also exists on the use of tobacco mosaic virus as templates for the synthesis and assembly formation of metal NPs [229].

Again, use of block copolymer molecules for NP assembly formation is very interesting in that they can separate into spherical micelles, vesicles, NWs, nanotubes, lamellae and cylinders [164, 245]. It has been observed that NPs follow the self-organization of the host molecules when sequestered by a particular block of the polymer, and the organization can occur in solutions or films. For example, polystyrene-b-poly(methyl methacrylate) films were used as templates to assemble CdSe NRs on the surface of cylindrical or lamellar poly(methyl methacrylate) domains [228]. Self-assembly of PbS NPs have also been demonstrated on the surface of cylindrical block polyferrocenylsilane-b-poly(2-vinylpyridine) co-micelles [227].

1.3.1.c. Self-assembly at interfaces

The assembly of NPs at the interfaces of liquid–liquid, liquid–air and liquid–solid can be affected by techniques such as Langmuir-Blodgett [246–248], sedimentation or evaporation-induced self-assembly [249–251], and the adsorption of NPs [232, 252, 253].

In the Langmuir-Blodgett technique, NP monolayers are formed at the water–air interface and the same then transferred onto a solid substrate [246]. Using this technique higher-order NP architectures have been generated by laser heating of the monolayer [254], and also by controlled dewetting of the monolayer on a substrate [255].

Evaporation-mediated self-assembly of NPs, driven by solvent evaporation and assisted by electrostatic interactions [249], leads to arrays as well as complex lattices of semiconductor, metal and magnetic NPs. The method provides a simple approach to the formation of highly ordered NP structures over a large area on solid surfaces. Apparently, the first reports of a NC "artificial solid" superlattice were published by Bentzon and co-workers in 1989 [256] and 1990 [257]. They observed the spontaneous formation of ordered 3D arrays of Fe oxide particles when a drop of colloidal solution containing the particles was placed on a transmission electron microscope (TEM) grid and the solvent was allowed to evaporate.

Interestingly, interfaces between liquids offer unique platforms for the assembly of NPs. As exemplified by the works of Russell and co-workers [253, 258], size-dependent assembly of NPs, on one hand, as well as formation of ultrathin membranes of NPs has been mediated at the liquid–liquid interfaces. They have also demonstrated a way to obtain hierarchical assembly of NPs on liquid–liquid interfaces by assembling NPs on water droplets arranged in a hexagonal array on the surface of a polymer solution [259]. Alternatively, 1D chains and 2D assemblies could be generated at the liquid–liquid interfaces by manipulation of the initial synthesis conditions of the NPs [160, 260]. Typical air–water interface-assisted supracrystal formation was illustrated by the Pileni's group [198].

1.3.1.d. Assisted self-assembly

Other than the chemical means of guiding the assembly of NPs, electric or magnetic fields, shear or light have also been employed for directing NP assemblies. This is referred to as assisted self-asembly of NPs and it offers the ability to manipulate NP assemblies. Magnetic fields have been used for assembling of metal [261], metal oxide [262, 263] and composite NPs [264]. For ferromagnetic NPs with sufficiently pinned magnetic moments the application of magnetic field enhances their organization [261, 265]. Whereas, superparamagnetic NPs, having randomly changing magnetic moment [266], undergo assembly formation when torque exerted by a magnetic field exceeds their thermal excitation energy [263, 266]. Chain-like structures [263] as well as 3D superlattices [267] of γ-Fe_2O_3 NPs has been obtained under the action of a magnetic field.

In the presence of electric fields, on the other hand, NPs get polarized and assemble

through dipole–dipole interactions forming chains that align parallel to the field lines. The length of NP chains depends on the strength of electric field, the concentration of NPs and the dielectric permittivity of the media. Both alternating current (a.c.) [268, 269] and direct current (d.c.) [270–272] have been employed to form exquisite arrays of CdS [270, 271] and CdSe [272] NRs.

Light mediated formation of NP assembly relies on optical confinement techniques [273–275] or irradiation-induced changes in photoactive ligands [276]. Faceted 3D crystals have been generated from the assembly of Au NPs, being stabilized with trans-azobenzene dithiol ligands that undergo trans-cis isomerization on exposure to UV radiation [276].

1.3.2. Properties of Nanoparticle Self-Assembled Structures

When NPs are assembled into higher order structures they show properties that are distinctly different from those of discrete NPs and corresponding bulk materials. New collective NP properties originate from the coupling of the surface plasmons, excitons or magnetic moments of individual NPs, or from a coherent state of the collections of NPs. For example, coherent vibration of NCs has been found for self-assembled fcc supracrystals of Ag NPs [250]. The coupling of the optical and magnetic properties of NPs are discussed below.

1.3.2.a. Coupling of plasmons

When metal NPs are present in close vicinity with each other, near-field coupling between the surface plasmons of the neighbouring NPs occurs owing to the transfer and confinement of electromagnetic energy. In case of a linear chain of NPs, the near-field coupling leads to transport of light in the subwavelength range along the chain. This phenomenon of light transport in a chain of NPs is referred to as waveguiding of light, and was proposed by Quinten [277]. For NPs strongly interacting with each other, simple Mie theory fails to predict the absorption properties of NP ensembles. These properties are best described by effective medium theories, modified versions of Mie theories or numerical simulations, for example, the finite-difference time-domain (FDTD) method and the discrete dipole approximation (DDA) [278].

Light extinction by NP assemblies depends on two factors: geometry of the assemblies (such as, 1D chains as against 2D lattices) and the strength of coupling of light. The second factor is controlled by the particle-particle spacing and the dielectric constant of the surroundingmedium. Again, it is the symmetry of NP arrays that determines the spatial distribution of charge polarizations and thus the splitting of plasmon bands in case

of assemblies. As for example, the near-field interactions between NPs present in their chains lead to redshift of the longitudinal band and blueshift of the transverse band, in comparison with those of isolated NPs only. The magnitude of the redshift is found to decay approximately exponentially with increasing interparticle separation [278–280]. The interparticle spacing in metal NP self-assembled structures can be much regulated by coating the particles with organic shells of varying thickness [159], such as by using stimuli-responsive polymer ligands [281], by judicious binding of NPs to DNA or proteins [282], or by varying the type and location of ligands on NPs [160, 161, 280, 283].

It is interseting to note that the assemblies of anisotropic metal NPs offer further control of the optical properties, namely, by controlling the orientation of NPs. A classic example being that the shape anisotropy of NRs gives rise to end-to-end and side-by-side NR organization [158, 205, 226, 284]. The end-to-end assembled NRs lead to redshift of the longitudinal plasmon band, while the side-by-side placement of NRs results in blueshift of the longitudinal plasmon band and redshift of the transverse band [158, 284].

Close-packed metal NPs in 3D crystals also give rise to unique, tunable optical and electronic properties. The coordinating ligands play the role to mediate electronic coupling between NPs and therefore the properties of the solids composed of NPs. When metal NPs are placed in proximity in the solids, the average dielectric constant of the surrounding medium increases and the SPR shifts to lower energy [285, 286].

1.3.2.b. Coupling of excitons

Coupling of properties of semiconductor NPs occurs through two mechanisms: electron exchange transfer (Dexter transfer) [287] and Förster resonance energy transfer (FRET) [288–290]. Dexter transfer requires an overlap of the wavefunctions of the NPs, and is typically observed for NPs separated by short (<2 nm) spacings [287]. FRET, on the other hand, occurs as a result of long-range dipole–dipole interactions between NPs that are separated by distances of 2 to 10 nm (ca.). An exciton generated in a smaller NP migrates rapidly to the larger NP in the direction of the reduced energy gap [289, 291–293].

1.3.2.c. Plasmon–exciton interactions

The coupling of excitonic and plasmonic properties in hybrid self-assembled structures of semiconductor and metallic NPs can lead to many interesting effects, such as energy transfer [294], enhanced emission [294], wavelength shift of photoluminescence emission [295] and the nonlinear Fano resonance [296]. Plasmon–exciton interactions can enhance as well as quench the photoluminescence of semiconductor NPs and, in addition, decrease photoluminescence lifetime [294, 297–299]. Photoluminesence enhancement

originates from the amplification of electromagnetic field by the plasmon resonance of metal NPs in the vicinity of semiconductor NPs, whereas quenching occurs as a result of energy transfer from semiconductor NPs to metal NPs.

Plasmon–exciton interactions depend on the mutual arrangement [300], size [287, 294], shape [289], and ratio of metal to semiconductor NPs [292, 297], in addition also to the distance between them [297]. The coupling is also strongly dependent on the type of material. For example, for CdTe NWs photoluminescence enhancement occurs by different mechanisms when the surrounding metal NP is Au [299] than when it is Ag [301].

1.3.2.d. Magnetic coupling

Assemblies of magnetic (metal and metal oxide) NPs give rise to interesting magnetic properties that originate as a result of interparticle interactions and finite-size effects [302, 303]. Studies into the magnetic properties have been extensively performed on the 1D and 2D assemblies of NPs. Pileni and co-workers have reported the difference in magnetic properties of isolated Co NPs versus their chains [304]. An increase in the remenance and coercivity was observed for the 1D Co NP chains, which is due to the orientation of magnetic moments of individual NPs in the direction of the magnetic field. Similarly, a 1D chain of Co NPs was also investigated by Kang et al. under the influence of a 0.05 T magnetic field. As the temperature decreased from 300 K to 5 K, the coercivity of the magnetic field induced assembly increased from 150.7 Oe to 346.7 Oe [305]. A higher magnetic field was, therefore, required to reverse the magnetization for magnetic field induced assemblies compared to randomly dispersed Co NPs. Similar trends were also observed with the aggregated NPs in 2D assemblies.

Furthermore, the increase of the barrier energy, E_b – which separates two minima states of magnetization – slows down magnetic relaxation of individual NPs. Therefore, the NP assemblies show interesting properties such as an increase in the blocking temperature, T_B, [206] and a change in the shape of the hysteresis loop towards a square shape [303, 306]. For example, Stellacci's group showed that chains of γ-Fe_2O_3 NPs display a 40 K increase in T_B and a faster approach to magnetization on variation of magnetic field, in comparison with isolated NPs and their aggregates [206]. Again, the ordering and packing density of magnetic NPs, and also the shape of the self-assembled structures, influences the collective magnetic properties of NP assemblies [306, 307]. For example, Co NCs arranged in a fcc 3D lattice showed a significant narrowing of the peak in the zero-field-cooled susceptibility, compared with a film of disordered NPs [306]. The ordering also led to a higher value of coercivity and a slower approach to saturation in a

hysteresis loop.

1.3.3. Applications of Self-Assembled Nanoparticles

The potential for application of self-assembled NPs is diverse. Although, a host of NP assemblies have already been developed for use in myriads of areas, yet more studies in this direction are continuing to flourish for advanced applications. Self-assembled structures of NPs opens up opportunities to reduce the size of optoelectronic devices and components such as plasmon waveguides, focusing lenses, light generators and optical switches [308–311]. Thus far, such NP structures have, for example, been used as sensors – by using the changes in the wavelengths of metal NPs, changes in the photoluminescence of semiconductor NPs, or variations in the magnetic relaxation of magnetic NPs in many chemical or biological environments. NP assemblies have also been used as nanoscale thermometers and pH meters [312], as bio- and chemical sensors [295, 313, 314], and as 'plasmon rulers' [315–317]. The techniques based on the properties of self-assembled NPs has been found to show increased selectivity and sensitivity, an unlimited lifetime and a larger measurement range, as compared with the common conventional sensing methods.

The first plasmon-based sensor for the detection of oligonucleotides relied on the colour change that occurred when NP–DNA conjugates underwent assembly mediated by hybridization of DNA with target oligonucleotides [313]. Following this work, the colorimetric sensing of enzymatic activity [318], the detection of DNA sequences or hybridization [319], and the sensing of heavy metal ions (such as Hg^{2+} or Pb^{2+}; [314]) have been reported. For example, the attraction between Au NRs end-terminated with cysteine or glutathione led to the NR self-assembly in the end-to-end mode [320]. The redshift in the LSPR band was used for the detection of micromolar concentrations of cysteine or glutathione.

The dependence of the coupling of plasmon resonances on interparticle separation in pairs of metal NP–DNA conjugates allowed measurements of distances from 1 to 100 nm in biological systems [315]. The 'plasmonic ruler' was used in the study of the kinetics of DNA hybridization [315], the dynamics of DNA bending and cleavage [316], and the activity of enzymes [317].

A variety of reduced-symmetry plasmonic nanostructure complexes such as NP heterodimers [321, 322], and septamers [323] support Fano resonances. The asymmetric Fano line shape has great potential for the design of low-loss metamaterials and subwavelength waveguides with low radiative losses [324, 325]. The Fano resonance profile also promises applications in sensors, lasing, switching, and nonlinear and slow-

light devices [326].

The “hot spots” created by localized electromagnetic fields from assemblies of metal NPs have been used for the detection of molecules via surface-enhanced Raman scattering (SERS) [327–329]. The location of hot spots is largely determined by the spatial arrangements of NPs [330] and their shapes [331]. Compared with individual NPs, ensembles of metal NPs showed up to tenfold enhancement of Raman scattering [328].

Variation in exciton–plasmon interactions was also used for the detection of DNA and proteins, which relied on the shift in photoluminescence wavelength [295] or quenching of photoluminescence of semiconductor NPs adjacent to metal NPs [312, 332].

Data storage devices derived from self-assembled nanostructures have been demonstrated for Pt NPs deposited on a tobacco mosaic virus template [333]. The device shows basic memory operations, such as operating voltages, data retention and cycle ability. Arrays of self-assembled magnetic FePt and CoPt NPs were examined as the potential medium for magnetic data storage [334, 335]. Data recording at linear densities of up to 5,000 flux changes per mm has been demonstrated by using 3D superlattices of FePt NPs [334].

Multifunctional hybrid assemblies of magnetic and metal NPs have also been used for the separation of proteins [336] and the recovery of catalysts [337]. Following adsorption of proteins or catalysts on metal NPs in the assemblies, they could be scavenged from the fluid phase by applying an external magnetic field.

Compartmentalization of self-assembled NPs in polymersomes, liposomes or polymer capsules paves the way for producing multifunctional carriers for the delivery of biologically active species or sensing applications in the biological, medical and pharmacological fields [338–340]. For example, semiconductor and magnetic NPs were embedded in the walls of polymer capsules, while the interior of the capsules was loaded with cargo molecules [339]. Compartmentalization of NPs in the capsules allowed for the remote manipulation of the carriers by applying an external magnetic field, the identification of the carriers by measuring their fluorescence, and the controlled release of the cargo molecules by locally heating the system to deform or disintegrate capsular walls [340].

1.4. MOTIVATION BEHIND THE THESIS

Numerous synthesis protocols for core–shell NPs of various combinations of core and shell materials have been developed. There still remains more types and variations of particles unexplored and the effective ways of generation of such particles could prove to be useful for various applications. For instance, variations of the type such as organic

nanoshell surrounding a plasmonic metal NP or for that matter organic NC coated with an inorganic metallic shell can prove to be quite promising.

Most commonly used pharmaceutical drugs are hydrophobic in nature. Special formulations are required to make their aqueous dispersions for drug delivery. Usually, surfactants or other NP-based delivery vehicles are commonly used. The carriers include liposomes, micelles, polymeric micelles, ceramic, hydrophilic drug–polymer complexes and polymeric NPs [341]. However many surfactants themselves tend to increase the systemic toxicity of the drug formulation. Thus, making stable formulation of drugs for systemic administration is highly challenging. To overcome this difficulty, a stable dispersion of drugs into aqueous systems is desirable using delivery vehicles.

As mentioned above (section 1.3), various assemblies of NPs have been generated starting from spherical and rod-shaped NPs. However, comparative studies relating to changes of optical properties have not been carried out, such as by varying the concentration of assembler molecules on different-sized NPs. This could prove to be useful in understanding the dependence of SPR band as well as length of assemblies on the concentration of assembler molecules and on the NPs' size.

Further, combination of inorganic NPs with organic moieties, giving rise to inorganic–organic hybrid materials are of paramount importance, as described in the section 1.2. The organization of NPs within an organic matrix forming 3D hybrid crystals have not been explored yet. Blend of inorganic NPs with organic moieties could provide greater rigidity to the composite material. In addition, NPs contained in such structures would possibly remain intact without phase segregation and loss of generality. The crystals could possess properties of the organic component, in addition to the properties of NPs–optical, magnetic, electronic, etc.

1.5. OUTLINE OF THE THESIS

The thesis is organized as follows. **Chapter 1** provides an introduction and review of literatures pertaining to the field of nanomaterials, specifically revolving around the topics that the works contained in the thesis are based upon. It gives a glimpse of some of the key developments and novel properties of NPs as such and of their higher order architectures. The remaining chapters of the thesis are outlined as under.

In **Chapter 2**, the generation of 0D Ag@pHA core–shell NPs (pHA: *p*-hydroxyacetanilide), where a crystalline pHA layer formed on the Ag NPs, is described. The NPs formed when an aqueous mixture of Ag NPs and acetone-solution of pHA was allowed to evaporate at room temperature. UV/Vis spectroscopic measurements of the crystallizing solution at different times showed a systematic blueshift of the extinction

maximum of Ag NPs, indicating the changes in the dielectric medium surrounding the NPs. The formation of the crystalline shell of pHA was established using powder X-ray diffraction (XRD) and transmission electron microscopy (TEM) studies. TEM observations also indicated melting of the organic layer in the presence of a high energy beam and at longer exposure times. The results also indicated deposition of smaller organic crystals first on the surface of the NPs followed by growth of the organic layer leading to the formation of the shell.

Chapter 3 also deals with the generation of 0D core–shell NPs, viz., having an organic crystalline core and that is coated with an inorganic metallic shell. First, NCs of pHA were generated in the aqueous medium. TEM and powder XRD evidenced the formation of pHA NCs and of their crystalline nature. The NCs were then coated with Au to form pHA@Au core–shell NPs, where the thickness of the Au shell was on the order of nanometres. The formation of Au nanoshell – surrounding pHA NC – was confirmed from its SPR band in the UV/Vis spectrum and by TEM measurements. Further, on treatment of the core–shell particles with a solution comprising of NaCl and HCl (pH < 3), the Au shell could be dissolved, subsequently releasing pHA molecules. The dissolution of Au shell was marked by the gradual diminishing of its SPR band, while the release of pHA molecules in the solution was confirmed from TEM and FTIR studies. The findings suggest that the core–shell NP could be hypothesized to be a model for encapsulating drug molecules, in their crystalline forms, for slow as well as targeted release.

A discussion of 1D assembly formation of Au NPs of different sizes using *p*-aminoacetanilide (pAA) as an "assembler" is presented in **Chapter 4**. Citrate-stabilized Au NPs were assembled into linear arrays of NPs by treatment with protonated-pAA solution. The appearance of a longitudinal SPR band at a longer wavelength was an indicator of the assembly formation. The results elucidated the independent and synergistic effects of pAA concentration and particle sizes on tuning the position of the SPR. For example, the shifting of the band to the red side was more when concentration of pAA was higher and/or when starting with larger particles than with smaller ones. Thus, organization of NPs into linear arrays could be governed simultaneously by two factors: concentration of the assembler and sizes of the NPs.

Chapter 5 focuses on our investigations on the generation of inorganic NP–organic hybrid composite crystals. The composite crystals consisted of Au NPs as the inorganic component and pHA as the organic one. The dimensions of the 3D crystals were on the order of several millimetres. They could be grown from an aqueous solution of Au NPs and pHA at 35 °C. UV/Vis spectroscopic analyses of the crystals not only reflected the

presence of Au NPs but also their degree of association inside the crystals. TEM images indicated Au NPs being dispersed randomly in the crystal with increase in their density when crystallized in the presence of low concentration of pHA. Further, single crystal XRD studies revealed that the composite crystals assumed monoclinic and orthorhombic polymorphic forms attributable to the crystal motifs of pHA. However, at lower concentrations of pHA the orthorhombic form was favored. Optical microscopic investigation revealed the presence of Au NP crystals, the color of which represented their density. For example, a lower ratio of Au NPs to pHA present in the medium led to crystals with the retention of the color (ruby red) of as-synthesized Au NPs, whereas a higher ratio imparted purple color to the crystals, which is characteristic of agglomerated forms of Au NPs.

Chapter 6 concerns the growth of 2D as well as 3D crystals of magnetic NPs, Fe_3O_4 and Fe_3O_4@Au. Initially, monodisperse Fe_3O_4 NPs were synthesized by high temperature decomposition of Fe-oleate complex. To the dispersion of NPs in chloroform, PEG (MW 6000) was added and the resulting solution was subjected to an external magnetic field, undisturbed. Following evaporation of chloroform, dark brown crystals were obtained. TEM investigation of the crystals showed Fe_3O_4 NPs organized in the form of 2D and 3D superstructures. Further, the work was extended with Au coated Fe_3O_4 (Fe_3O_4@Au) NPs; the results were similar to that for bare Fe_3O_4 NPs. In the case of Fe_3O_4@Au NPs, in addition to being magnetic, the 3D crystals possessed optical properties due to presence of nano-sized Au. The magnetic behaviour of the crystals was ascertained from vibrating sample magnetometer (VSM) measurements.

Lastly in **Chapter 7**, the key results of the research works carried out are summarized along with giving an outlook of prospective works that can be pursued in the above fields.

Chapter 2

Inorganic–Organic Core–Shell Crystalline Nanoparticles

In this chapter (the work contained herein is published in an international peer-reviewed journal¶), I have described the formation of crystalline organic shell structures on Ag nanoparticles (NPs). The organic molecule that has been used is *p*-hydroxyacetanilide (pHA), known also as paracetamol or acetaminophen. Addition of pHA to citrate-stabilized Ag NPs in aqueous medium, followed by evaporation, led to the formation of zero-dimensional (0D) core–shell structures with pHA as the shell (Ag@pHA; Scheme 2.1), which was revealed by transmission electron microscopy (TEM). Selected area electron diffraction (SAED) and powder X-ray diffraction (XRD) studies supported the presence of crystalline Ag NP as well as pHA. Interestingly, with the exposure to high energy electron beams of the TEM for longer period, the outer organic layers could be found to have been melted. Further, TEM experiments suggested the deposition of smaller organic crystals on the surface of the NPs followed by their further growth as a mechanism of formation of the core–shell structure.

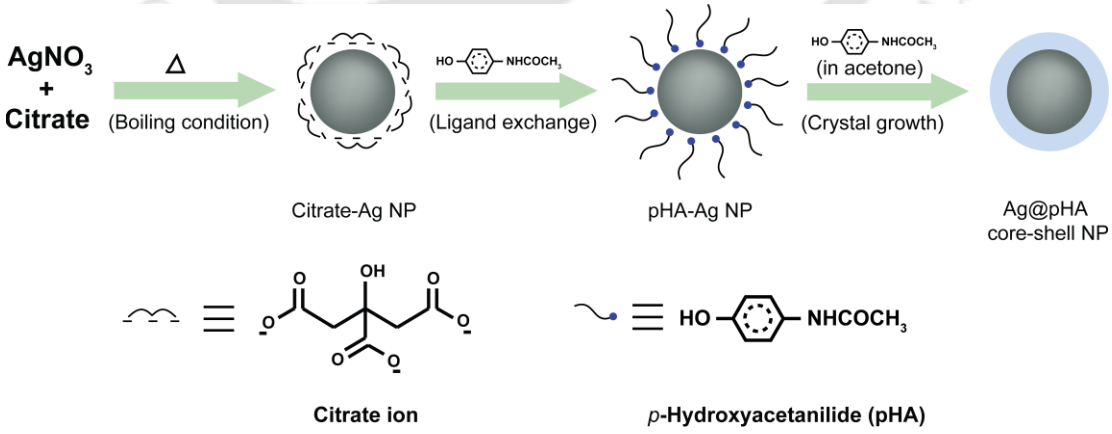

Scheme 2.1. Illustration of the generation of Ag@pHA core–shell NPs.

¶[Das *et al. RSC Adv.* **2012**, *2*, 10245–10250] - Reproduced by permission of The Royal Society of Chemistry http://pubs.rsc.org/en/content/articlelanding/2012/ra/c2ra21264a#!divAbstract

2.1. EXPERIMENTAL

Materials. Silver nitrate ($AgNO_3$, Aldrich), trisodium citrate (Merck) and *p*-hydroxyacetanilide (Merck) were all used as received without further purification. Milli-Q grade water with a resistivity of 18.2 $M\Omega.cm^{-1}$ was used in all the experiments. All glassware and magnetic stir bars used were cleaned with aqua regia and rinsed with Milli-Q water prior to start of experiments.

Synthesis of Ag NP colloid. Colloidal Ag NP solution was prepared by the reduction of $AgNO_3$ by trisodium citrate, which also acted as the stabilizing agent for the NPs. [45] Typically, 17 mg $AgNO_3$ was dissolved in 100 mL water and the solution was allowed to boil under magnetic stirring. After 2 min of boiling, aqueous solution of citrate (35 mM, 10 mL) was rapidly added to the flask. The solution turned yellowish within a few minutes, indicating the formation of Ag NPs. The solution was allowed to boil for additional 6 min and after this the heating mantle was removed and the solution was allowed to cool. The so-prepared NP dispersion was washed by centrifugal precipitation at 5000 RPM (twice); the precipitate was redispersed in water for further use.

Growth of Ag NP–pHA core–shell NPs. To 50 mL of the above solution, 100 mg pHA was dissolved and the resulting solution was allowed to stand undisturbed for 10–12 h. After this time, the solution was centrifuged at 5000 RPM and the precipitate (another sample of which was also used for FTIR studies) was redispersed in 40 mL water. 20 mL acetone solution of pHA (300 mg) was added to the above solution under vigorous stirring. Stirring was allowed to continue for some time. The dispersion was allowed to stand as such at room temperature and on day 5, the same was centrifuged and precipitate used for XRD and TEM (wherever mentioned) studies. On the other hand, the dispersion samples (without centrifugation) on day 0, day 3, and day 5 were used for TEM analyses.

Analytical Measurements. UV/Vis absorption spectra were recorded using a Hitachi U–2900 spectrophotometer. FTIR spectra, of discs of the sample prepared after mixing with KBr, were recorded using a Perkin Elmer Spectrum One spectrometer. A TEM sample was prepared by drop-coating dispersion onto a Cu grid coated with carbon. Images were acquired using a JEOL JEM 2100 transmission electron microscope operating at a maximum accelerating voltage of 200 kV. Samples for powder XRD were prepared by drying the dispersions onto glass cover slips. XRD data were acquired using a Bruker AXS D8 Advance X-ray diffractometer with $CuK\alpha_1$ radiation (λ = 1.54060 Å), operated at 40 kV and 40 mA.

2.2. RESULTS AND DISCUSSION

As mentioned above, centrifuged sample of citrate-stabilized Ag NPs was incubated with pHA to obtain pHA-stabilized Ag NPs. The UV/Vis spectrum of pHA-stabilized Ag NPs exhibited a rather broad extinction spectrum with maximum occurring at 435 nm (Figure 2.1a). This is indicative of the presence of Ag NPs of multiple shapes and sizes. TEM measurements indicated the presence of a few rod-shaped particles, in addition to the spherical particles formed in the medium (Figure 2.1b–d). The average (spherical) particle size as measured using TEM was 58 ± 7 nm. The presence of non-spherical particles,

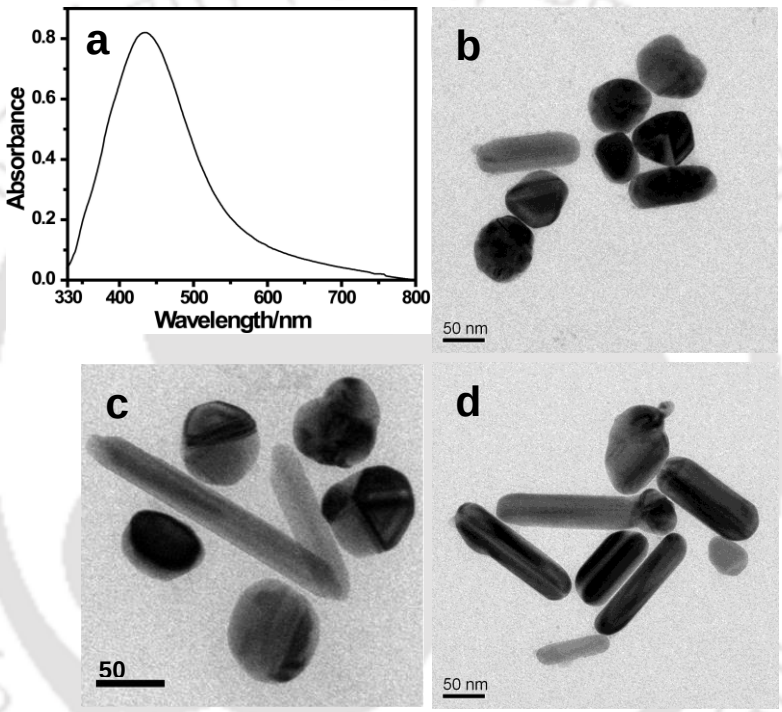

Figure 2.1. (a) UV/Vis spectrum and (b–d) TEM images of pHA-stabilized Ag NPs.

coincidently, helped in studying the crystallization behavior of pHA on differently shaped particles under identical experimental conditions. Fourier transform infrared (FTIR) spectroscopic measurement of the pHA-incubated and centrifuged samples indicated the presence of N–H stretching band at 3206 cm^{-1} (Figure 2.2), which was considerably blue-shifted from the N–H stretching band of pure pHA (3168 cm^{-1}). Also, the intensity of the peak in the former was considerably diminished in comparison to that in the latter. This indicated that the weakly bound citrate ligands were replaced by pHA moieties having –NH functional group that can otherwise bind more strongly to the NP surfaces. [342; refer also to Chapter 5] It was observed that removal of citrate from the medium and

functionalization of the citrate-stabilized Ag NPs with pHA rendered them amenable for further crystal growth. Acetone-dissolved pHA was then added to the dispersion, so that the concentration of pHA in the medium was 0.331 M. The final dispersion consisted of Ag NPs with a value of extinction at the maximum being 0.54 (indicated as day 0 in Figure 2.3). The dispersion was then kept in a vial covered with perforated aluminum foil and was allowed to evaporate at room temperature.

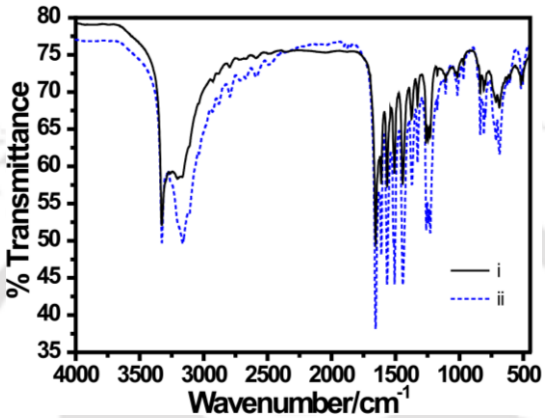

Figure 2.2. FTIR spectra of (i) pHA-stabilized Ag NPs, and (ii) pristine pHA.

The UV/Vis spectrum of the dispersion of Ag NP and pHA (mentioned above) was recorded at time intervals of 24 h, the results of which are shown in Figure 2.3a. Interestingly, the surface plasmon resonance (SPR) band due to Ag NPs exhibited gradual narrowing with time in comparison to that of the dispersion on day 0. In addition to narrowing, blueshift of the band could be observed. After slow evaporation of the solution till day 5, the volume of the mixture was found to be less than that of the Ag NP dispersion (i.e., before addition of acetone-dissolved pHA) on day 0. The reduction in the volume was due to evaporation of acetone and some amount of water from the medium. Typically, when starting with a mixture of 40 mL Ag NP dispersion and 20 mL acetone-dissolved pHA the volume was a little less than 40 mL on day 5. UV/Vis spectrum of the dispersion indicated the extinction at the peak (which was blue-shifted by as much as 5 nm from the day 0 spectrum) to be 0.79. Remarkably, upon dilution of the dispersion of day 5 to that of the original volume (to have the concentration as on day 0), by addition of a mixture of water and acetone, the extinction spectrum broadened as well as red-shifted in position to its original value (indicated as day 5 dil. in Figure 2.3a, b) i.e., due to the dispersion on day 0. Thus starting with the dispersion on day 0 the UV/Vis spectrum consisted of a broad peak with maximum at 439 nm, which narrowed and blue-shifted to 434 nm upon

evaporation till day 5. This dispersion upon dilution led to a broader peak with the maximum at 438 nm. The observations suggested that the dielectric layer surrounding the Ag NPs changed upon evaporation of the solvent (causing line narrowing and blueshift) which upon dilution reverted back to the original spectrum. That the SPR frequency of metal NPs can be tuned by coating with a dielectric material has already been reported. [343, 344] The small difference in the extinction spectrum of the original dispersion (day 0) and that of the diluted one (day 5) could be due to agglomeration of a few NPs during dilution. On the other hand, control experiments, involving recording of UV/Vis spectra

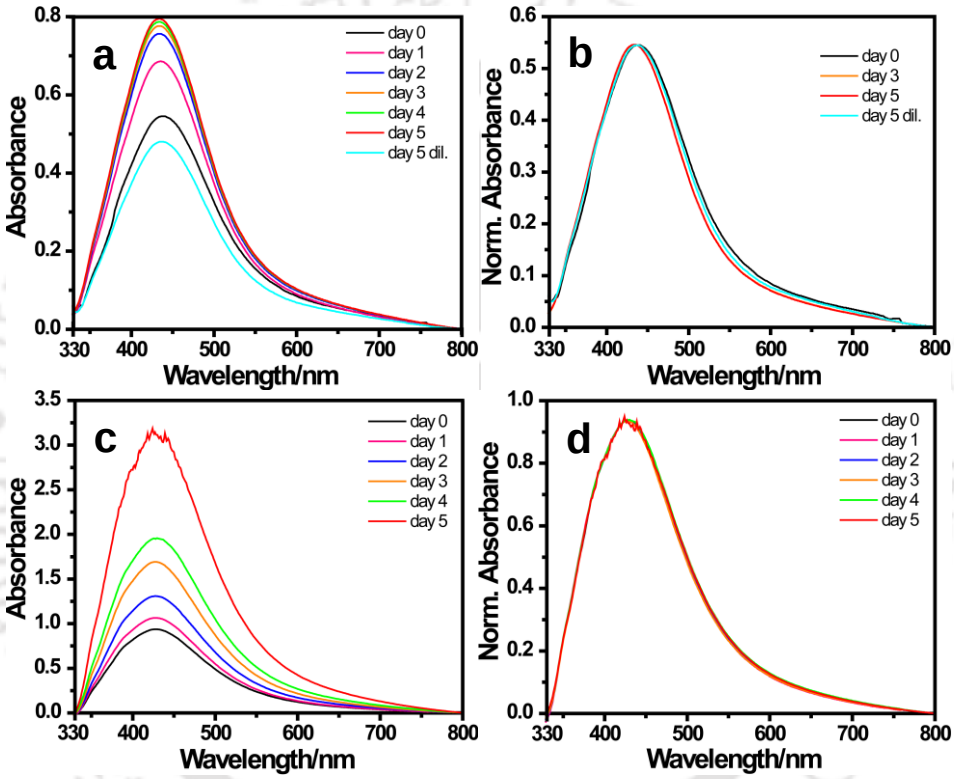

Figure 2.3. (a, b) UV/Vis spectra of Ag NP–pHA crystallizing medium, recorded for samples from day 0 to day 5. (λ_{max}:: day 0: 439 nm; day 1: 435 nm; day 2: 435 nm; day 3: 434 nm; day 4: 434 nm; day 5: 434 nm; day 5 dil.: 438 nm). Spectra in panel (a) represent as-recorded data, while spectra in panel (b) represent data normalized to the value of maximum at the peak. (c, d) UV/Vis spectra of pHA-stabilized Ag NP dispersion in water on different days. The spectra in (c) represent the as-recorded spectra, while (d) represent spectra normalized to absorbance of sample on day 0.

of pHA-stabilized Ag NP dispersion in water only (being evaporated at 40 °C), showed no change in the line shape and position with time (Figure 2.3c, d).

TEM analyses of the dispersion on day 0 (Figure 2.4) showed Ag NPs with no discernible change either in size or agglomeration in comparison to as-prepared NPs. Any

minor difference could be due to evaporation of the dispersion during the sample preparation. On the other hand, TEM images of the dispersion on day 3 indicated formation of shell around the NPs (Figure 2.5). It may be mentioned here that images recorded for samples earlier than day 3 consisted of depositions of smaller particles on the NPs. The shell formation was complete by day 3, although the thickness of the shell was not necessarily uniform. The typical shell thickness that could be observed was 2–8 nm, albeit thickness higher than these could also be observed. It is interesting to note that the shell formation could also be observed around particles of rod shape and the thicknesses around both axes of the rod were nearly uniform (with a maximum of 5 nm

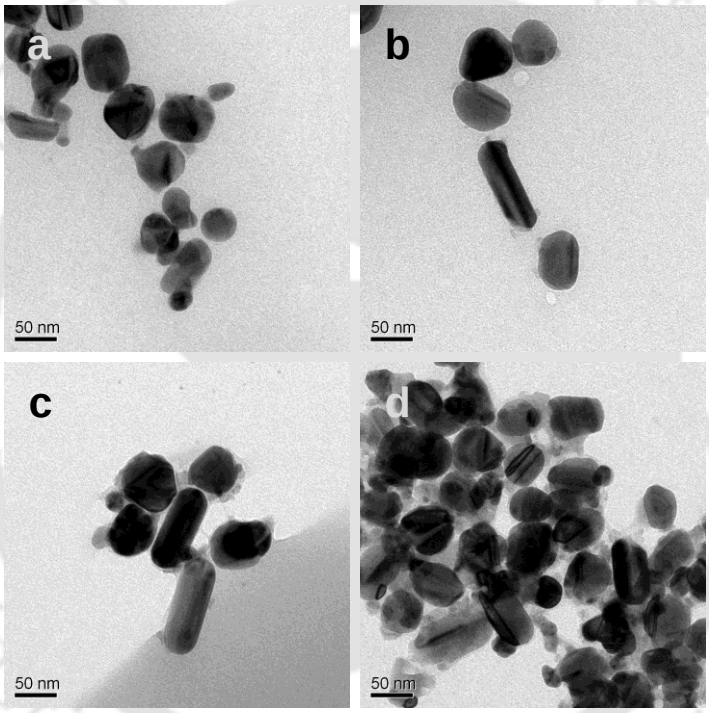

Figure 2.4. (a–d) TEM images of Ag NPs for sample obtained from the crystallizing medium on day 0.

along the minor axis). There was the presence of individual particles with shells surrounding the NPs. In addition, there were also particles which were fused at the shells. They were present in the forms of dimers, trimers and higher agglomerated structures. On day 5, the shells appeared relatively thicker than that on day 3 (Figure 2.6). It was also observed that the coated Ag NPs existed more as clusters than as isolated ones. It is possible that the shell that was forming on the NPs led to their fusions. Further, in order to check if the pHA shells which appeared over Ag NPs were artifacts developed during

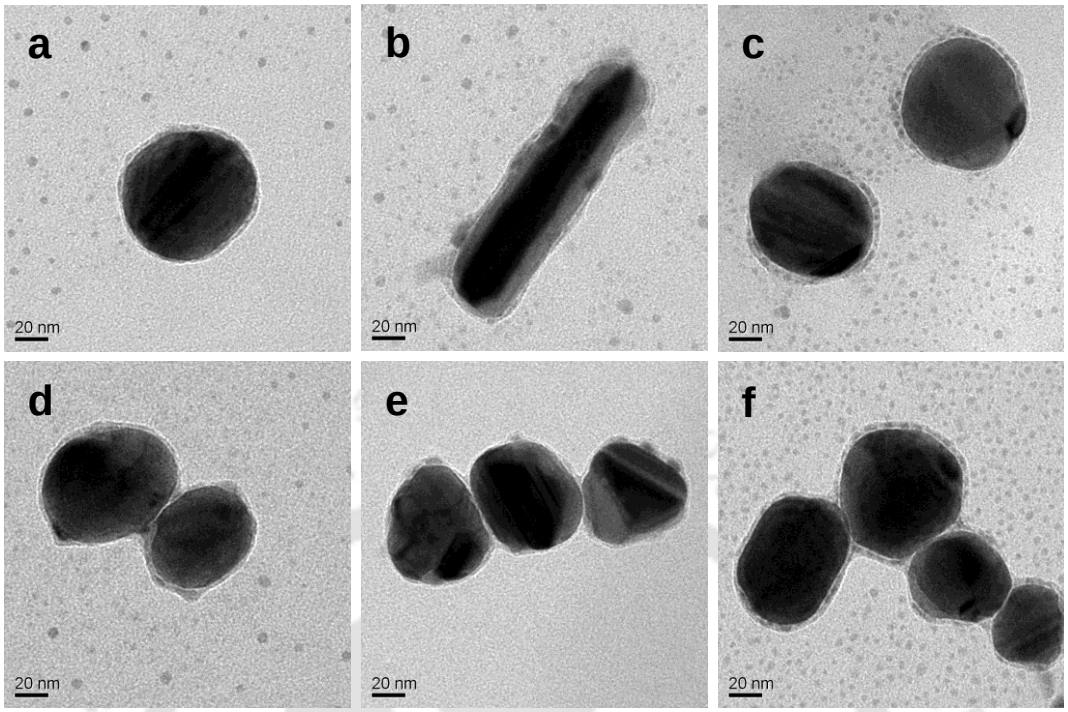

Figure 2.5. (a–f) TEM images of Ag@pHA NPs for sample obtained from the crystallizing medium on day 3.

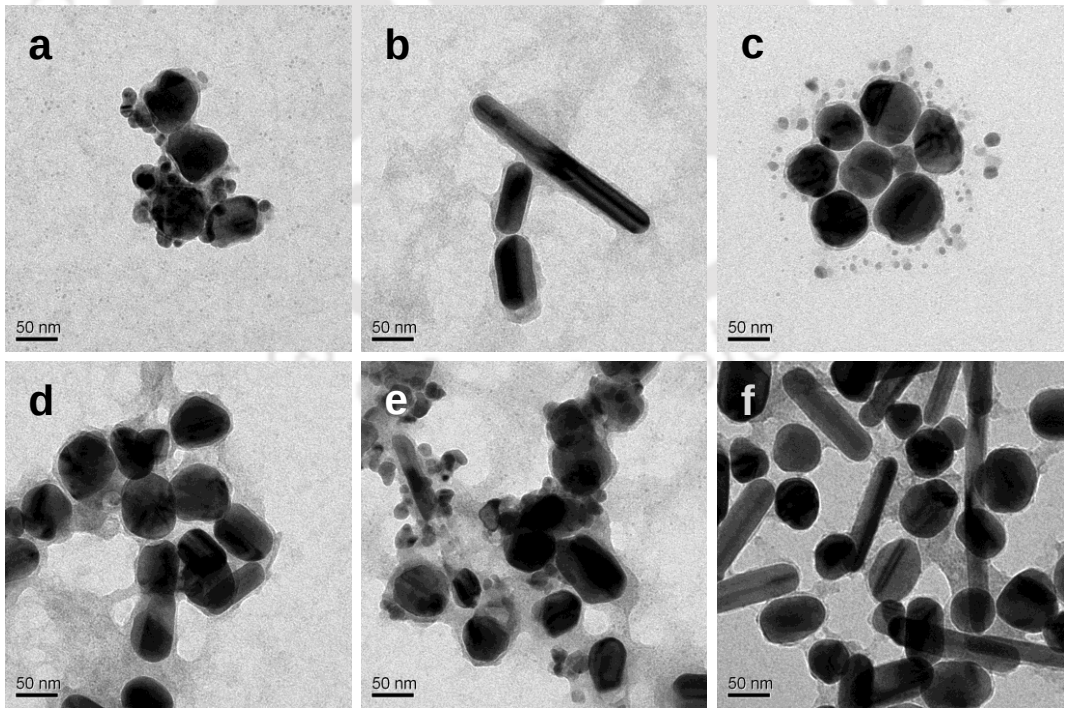

Figure 2.6. (a–d) TEM images of Ag@pHA NPs for sample obtained from the crystallizing medium on day 5.

the process of drying of the dispersion for TEM sample preparation, the concentrated dispersion on day 5 was centrifuged and the precipitate was then suspended in hexane. TEM investigation of the suspension clearly showed pHA shells surrounding Ag NPs (Figure 2.7), with no significant change with respect to the observations on the samples of day 3 or day 5. Thus pHA in water upon slow evaporation, in the presence of Ag NPs, resulted in the formation of core–shell structures consisting of NPs of Ag@pHA. Further, dilution of the solution to original volume led to loss of shells from most of the particles, as is clear from Figure 2.8. It is important to remember that the original dispersion (day 0) consisted of Ag NPs, pHA and acetone. The above results indicated that upon evaporation pHA might have been deposited on the surface of the NPs to have formed shells. Since pHA is highly soluble in water (and acetone) thus upon dilution the shell structures were dissolved leading to primarily bare NPs (probably with a thin stabilizing layer of pHA). In addition, there was the presence of a few fused NPs which could have resulted during dilution. In other words, when the pHA shell was dissolved after addition of excess solvent, the NPs (at least some of them) might have lost their stabilizing pHA layer completely and thus were fused together due to resultant lowered surface energy.

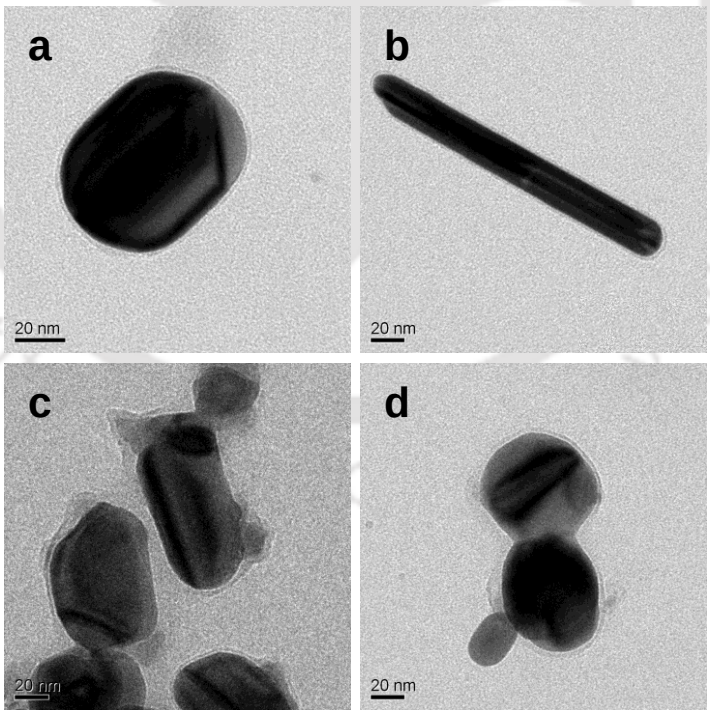

Figure 2.7. TEM images (a, b) of Ag@pHA NPs collected as powder from the precipitate obtained upon centrifugation of the crystallizing solution. The sample was collected from the medium on day 5 of evaporation.

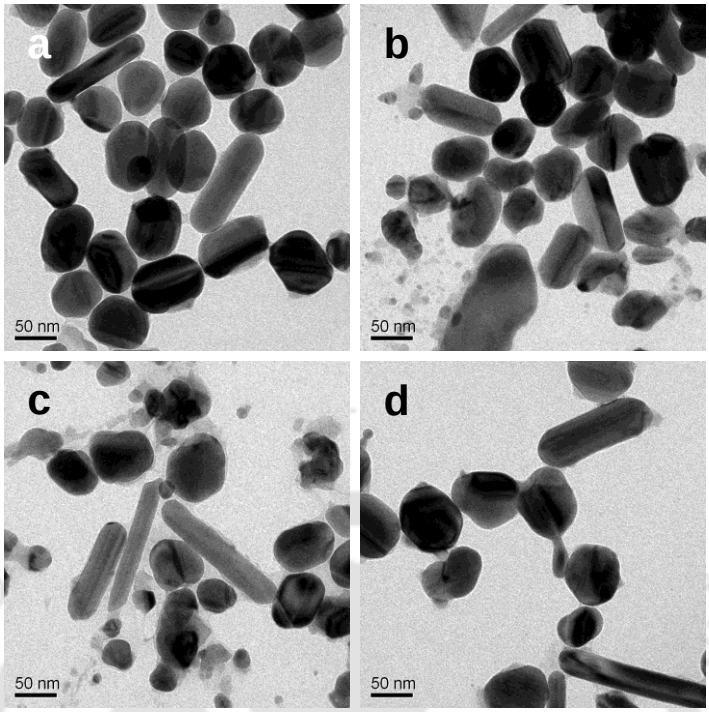

Figure 2.8. (a–d) TEM images of bare Ag NPs obtained following dilution (to achieve concentration as on day 0) of the crystallizing medium on day 5.

SAED analyses of a particle imaged under TEM indicated the presence of crystalline pHA in addition to metallic Ag. The SAED pattern is shown in Figure 2.9a. The presence of diffractions due to (022), (211), (310), (135) planes of pHA could be identified. In addition, diffractions from (111), (220) planes of face-centred cubic (*fcc*) Ag could also be observed in the same image. Thus the electron diffraction results indicated the presence of crystalline pHA in the core–shell structures (in addition to, of course, Ag NPs). Further, powder XRD pattern of the sample, obtained after 5 days of evaporation followed by centrifugation, is shown in Figure 2.9b. The pattern consisted of diffractions from $(10\bar{1})$, (101), (111), (022), $(21\bar{1})$, (211), (131), (310), $(30\bar{3})$ planes of the pHA crystals, corresponding to its monoclinic polymorphic form. In addition, there were peaks due to the presence of Ag, occurring at 38, 44 and 64° corresponding to diffractions from the (111), (200) and (220) planes respectively of metallic Ag. It may be mentioned here that at around these positions of diffraction peaks there ought to be the presence of peaks due to pHA also (see Chapter 5). However, the broadness of the peaks at those angles indicated the presence of Ag NPs. Additionally, the diffraction patterns were in agreement with literature values for both pHA and Ag NPs (Figure 2.10). Overall, the above results indicated that a mixture of Ag NPs and pHA upon evaporation led to the formation of crystalline shells of pHA on the surface of the NPs.

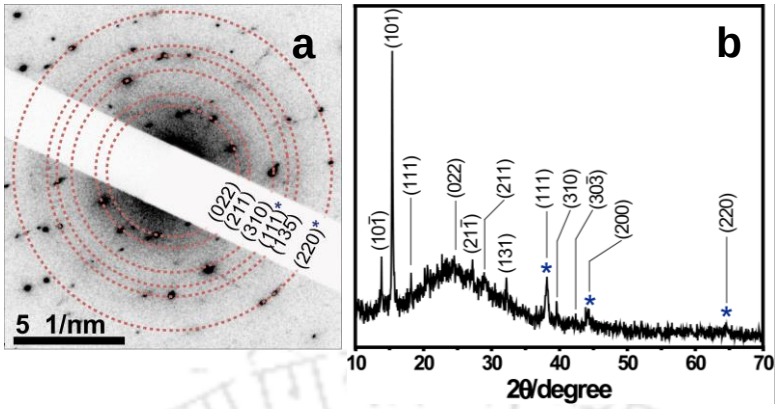

Figure 2.9. (a) SAED and (b) powder XRD patterns of Ag@pHA NPs (planes due to *fcc* Ag NP are marked with asterisk). The hump at around 2θ=25° in (b) is due to the diffractions of the glass cover slip used for the preparation of sample.

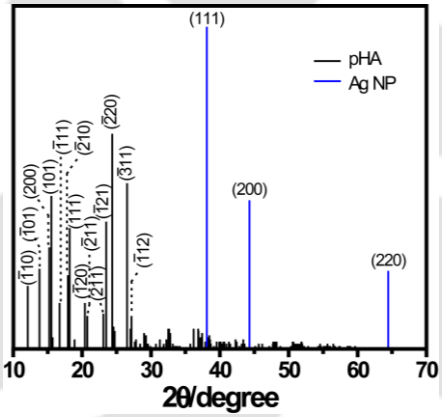

Figure 2.10. Standard XRD patterns of crystals of pHA and Ag NPs. Data were collected from JCPDS Card no. 00-039-1503 (pHA), 03-065-2871 (Ag NP).

The formation of a crystalline layer of pHA surrounding the Ag NP was further confirmed by inverse fast Fourier transform (IFFT) image analysis of the TEM image of one such crystal. Figure 2.11a shows a high resolution TEM (HRTEM) image of a particle consisting of shell. As is clear from the figure, the dark inner image is indicative of the presence of metallic Ag while the lighter outer shell is indicative of the organic moiety. Further, IFFT analysis of the image (Figure 2.11b) clearly indicated the presence of lattice fringes of spacing equal to 0.56 nm. The lattice spacing (*d*) was assigned to the (101) plane of pHA. The fringes were present beyond the darker region and till the lighter region of the composite particle. The contiguous fringes clearly evidenced the complete

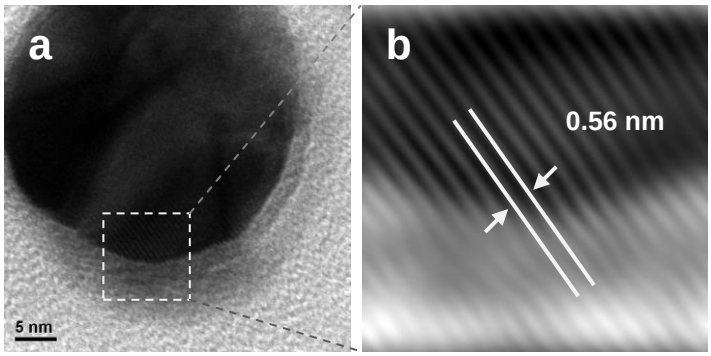

Figure 2.11. (a) HRTEM image of an Ag@pHA NP, and (b) corresponding IFFT image of the select region in (a).

encapsulation of Ag NPs by pHA crystals. It may be pointed out here that XRD results also indicated the growth of (101) plane as the major plane of growth. It is interesting to observe that while uniform spacing could be observed across the image, the bottom lighter part of the image indicated different contrast possibly due to height difference and inner core was due to metallic Ag.

Further, crystals were subjected to exposure of high energy electron beams in TEM, while the crystals were being imaged by the same beam. It was observed that exposure of the crystals to 200 kV beams being kept at higher resolution (400 kX) parameters for 5 min or longer led to melting of the same. It is already known that organic and other biological and non-conducting materials tend to melt or get damaged upon exposure to high energy electron beam. [345] Figure 2.12i shows one such crystal (rod-shaped) at 80 kX amplification. As is clear from the figure the crystal consisted of core–shell rod. The core– shell nature could be observed further at 200 kX amplification (Figure 2.12ii). On the other hand, at 400 kX magnification the outer shell of the crystal melted and the outer shell disappeared (Figure 2.12iii). A better view of the melted crystal at 80 kX magnification (Figure 2.13iv) again indicated that the entire outer shell of the crystal melted in the presence of the electron beam. The above observations clearly indicated the organic nature of the shell of the core–shell particle, substantiating the growth of organic shell (pHA crystal here) around the Ag NP/rod in the present experiments.

Additionally, electron diffraction studies of Ag@pHA NPs using electron beam at a particular magnification and the same sample being observed after melting of the pHA shell (following exposure to electron beam at higher magnifications) resulted in the observations of change in the SAED pattern (Figure 2.13). For instance, SAED pattern obtained for the particle observed at 300 kX magnification (Figure 2.13A1) consisted predominantly of diffractions from pHA crystal (Figure 2.13A2), planes due to which are

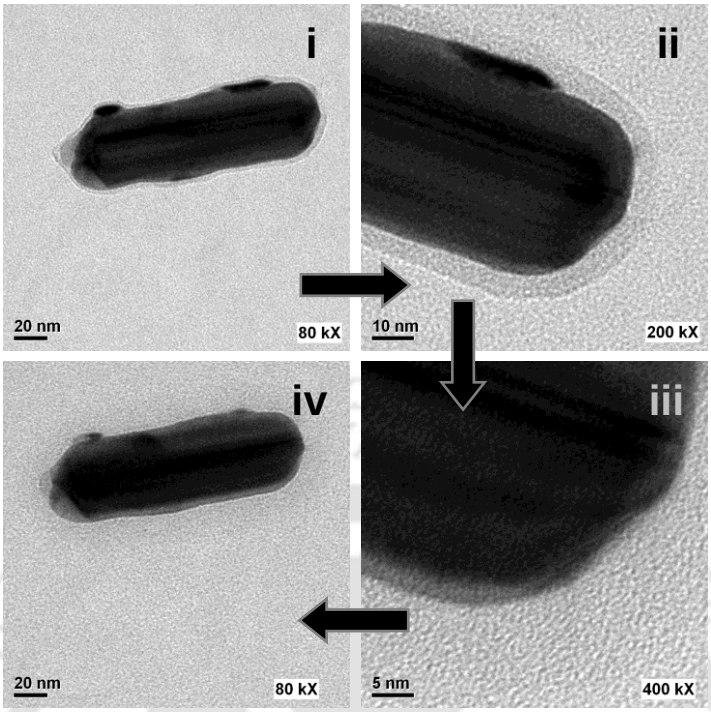

Figure 2.12. TEM images of an Ag@pHA NP at magnifications (i) 80 kX, (ii) 200 kX, (iii) 400 kX, and back to (iv) 80 kX.

indexed as (022), $(30\bar{3})$, $(15\bar{1})$. On increasing the magnification further (~500 kX), partial melting of pHA layer had occurred. Interestingly, recording the SAED pattern again at 300 kX magnification (Figure 2.13B1) revealed the appearance of diffraction patterns due to *fcc* Ag NP (marked with arrows), in addition to that due to pHA (Figure 2.13B2).

It is interesting to understand the mechanism of growth of the pHA crystal on the NPs. It was observed that presence of thinner shells could not be followed easily by TEM and hence growth of thicker shells was preferred. Thus the growth of organic moieties surrounding the NP/rod at shorter time of incubation indicated the presence of smaller crystals (of about 2 nm) attached to the NP/rod. The images are shown in Figure 2.14. It appears that smaller (organic) particles were deposited on the surfaces of the Ag crystals in the beginning (lighter particles attached to the larger darker particles). It could be that these particles were first formed in the medium and were subsequently attached to the NP due to the inherent instability of the NPs. The presence of organic particles could also be observed in the TEM, meaning that there were independent organic particles (smaller) in the medium (also refer to Figure 2.5). It has been reported that when an organic crystal is immersed in a medium in the presence of Au NPs the NPs get deposited over the crystal. [146] This has been attributed to the high surface free energy of the NPs. The same may

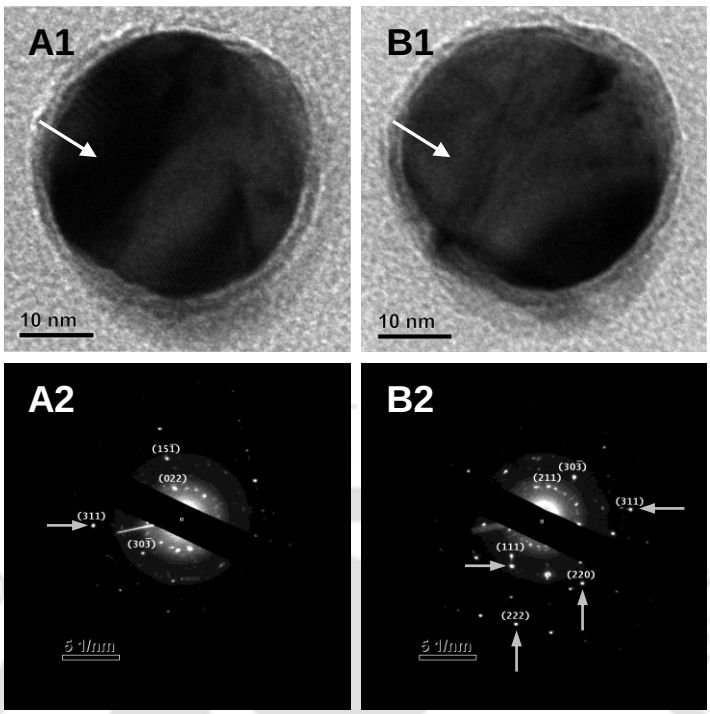

Figure 2.13. TEM images (A1, B1) and SAED patterns (A2, B2) of an Ag@pHA NP before (A1 and A2) and after (B1 and B2) melting experiments. (Arrows in A1 and B1 show the change in the contrast due to melting of pHA crystal on Ag NP, while those in A2 and B2 show the planes due to diffractions from an *fcc* Ag NP.) The sample was collected from the medium on day 5.

be the case here except for the fact the smaller organic crystals were deposited on the larger inorganic NP/rod. Once an initial layer of organic moieties was deposited on the NP/rod, further growth of organic crystal could take place using the initially deposited crystals as the seed crystals. Thus a uniform layer of organic crystal grew around the NP/rod with longer time of incubation. It may be mentioned here that the TEM images presented here consisted of large pHA crystals and thicker layers of the same on the NPs. On the other hand, the same could not be observed for thinner shells of crystals deposited on the NPs. It is plausible that still smaller crystals were first deposited on the NPs (which could not be observed under high energy beam) followed by growth of the crystalline layer. However, the uniform shell thickness of the thin layers also indicated growth of crystalline layers of pHA, akin to epitaxial growth, on the pHA layer stabilizing the NPs.

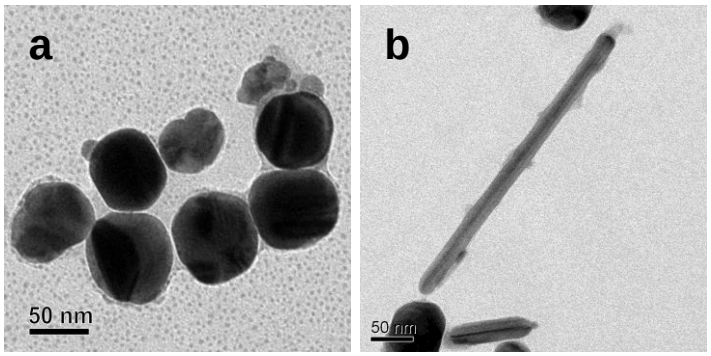

Figure 2.14. TEM images (a, b) showing the depositions/growth of pHA crystals over Ag NPs. The sample was collected from the medium prior to day 3 of evaporation.

2.3. CONCLUSIONS

In conclusion, Ag@pHA core–shell NPs were generated, where the crystalline pHA layer was formed on the NPs. The formation of the crystalline shell of the organic moiety was established using XRD and TEM studies. The crystalline shell could be melted using electron beam of TEM. Results also indicated that smaller particles were first deposited on the NP, followed by growth of the complete crystalline shell. The change in the optical property of the Ag NPs upon the formation of crystalline pHA shell makes an interesting appeal for modification of optical properties of NPs by organic crystals. It is anticipated that this work, first of its kind, on the growth of an organic molecule as a crystalline shell over a metallic NP would usher newer avenues of inorganic–organic hybrid materials with tunable properties.

Chapter 3

Organic–Inorganic Core–Shell Crystalline Nanoparticles

This chapter, different from Chapter 2 in having core and shell materials structurally in reverse order, concerns on the generation of 0D core–shell nanoparticles (NPs) consisting of an organic nanocrystal (NC) core encapsulated by a crystalline metallic shell. This was achieved by first preparing NCs of *p*-hydroxyacetanilide (pHA) in the aqueous medium. The NCs on treatment with hydrogen tetrachloroaurate ($HAuCl_4$) formed star-shaped Au-coated pHA crystals. On treating with cetyltrimethylammonium bromide (CTAB), however, uniform core–shell pHA@Au NPs were formed. Following this, CTAB moieties could be replaced with polyethylene glycol (PEG 400) – a water-soluble biocompatible polymer. UV/Vis and FTIR spectroscopy, transmission electron microscopy (TEM) and X-ray diffraction (XRD) were used to establish the formation of core–shell structures. Importantly, the Au shell of the core–shell particles, upon reaction with a mixed solution of NaCl and HCl (having pH < 3), was etched and thus pHA moieties were released into the medium (Scheme 3.1.). The results presented in this chapter are from a published article¶.

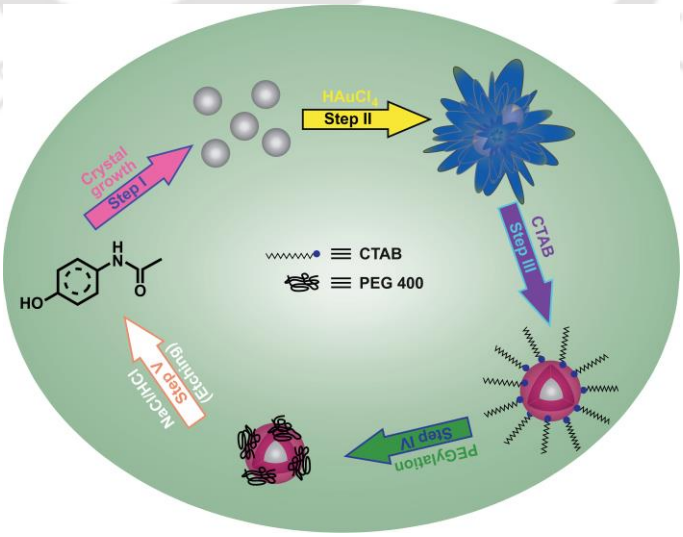

Scheme 3.1. Delineation of the various steps involved in the formation of pHA@Au core–shell NPs and release of pHA molecules following Au shell etching.

¶[Das *et al. Nanoscale* **2013**, *5*, 9247–9254] - Reproduced by permission of The Royal Society of Chemistry http://pubs.rsc.org/en/content/articlelanding/2013/nr/c3nr03566b#!divAbstract

3.1. EXPERIMENTAL

Materials. Hydrogen tetrachloroaurate ($HAuCl_4.3H_2O$, 17% Au in HCl, Sigma-Aldrich), *p*-hydroxyacetanilide (Merck), cetyltrimethylammonium bromide (Aldrich), polyethylene glycol (MW 400, Merck), sodium chloride (Merck) and hydrochloric acid (Merck) were all used as received without further purification. Milli-Q grade water with a resistivity of 18.2 $M\Omega.cm^{-1}$ was used throughout the experiments.

Generation of pHA NCs. A 10 mL aqueous supersaturated solution of pHA (1.32×10^{-1} M) was prepared in lukewarm water. As the solution cooled to room temperature, it was subjected to mechanical stirring. In about a minute of stirring the solution appeared to become cloudy. TEM sample was prepared right at the onset of cloudiness formation by placing a drop of the solution onto a carbon-coated Cu grid and wicking away the drop with a lint-free tissue paper after about 2 min of sampling.

Synthesis of pHA@Au NPs. Just prior to solution becoming cloudy, following stirring of supersaturated solution of pHA, 50 μL $HAuCl_4$ solution (10 mM) was added drop-wise under stirring, such that the concentration of $HAuCl_4$ in the reaction medium was 4.97×10^{-2} mM. It was observed that grains of colorless crystals precipitated during this time. In addition, a faint purplish colored solution formed which then changed to bluish following complete addition of $HAuCl_4$. The appearance of color was indicative of the formation of Au NPs in the reaction medium. The solution was stirred for 20 min and then a freshly prepared CTAB solution (300 μL, 0.1 M) was added and stirring was allowed to continue for additional 15 min. The color of the solution became pinkish during this time. In order to remove excess reagents (primarily, pHA and CTAB) and other ions, the solution was centrifuged twice, each time at 15,000 RPM for 15 min, and the precipitate – obtained likewise was also used for FTIR studies – was redispersed in 10 mL water. The above set of experiments were also performed separately, by having $HAuCl_4$ concentrations of 7.44×10^{-2} and 9.90×10^{-2} mM respectively in the reaction media, while keeping the concentration of pHA same. The amount of CTAB solution (0.1 M) added were 400 and 600 μL respectively, and the rest of the experiments were same as described above for the lowest concentration of $HAuCl_4$.

It may be stated here that all the experimental details described in the article were carried out with the $HAuCl_4$ treated pHA NC solution that was prepared with the highest concentration of the salt i.e., 9.90×10^{-2} mM, unless mentioned otherwise.

PEG stabilization. CTAB/pHA-stabilized NP solution was treated with PEG so as to have PEG-stabilized NPs. A 10 mL PEG-stabilized NP solution was prepared as follows. Four sets of CTAB/pHA-stabilized NP solutions were centrifuged and precipitates were combined and redispersed in 10 mL water. 100 μL PEG was added to same and the

resulting solution was allowed to stir for 3–4 h. The solution was centrifuged (at 15,000 RPM) and the precipitate redispersed in 10 mL water. The precipitate following centrifugation was used for FTIR studies.

Au etching experiment. PEG-stabilized NP solution, as prepared above, was treated with an aqueous solution containing a mixture of NaCl and HCl, which is known to etch metallic Au. NaCl/HCl aqueous solution was prepared by having total Cl^- ion concentration equal to 0.375 M, while keeping the ratio of concentrations of NaCl to HCl i.e., [NaCl]/[HCl] as 1, and such that the pH of the solution was less than 3. To 5 mL PEG-stabilized NP solution, 0.2 mL NaCl/HCl solution was added and the mixed solution was allowed to stir for 30 min, following which the UV/Vis spectrum was recorded. The addition of NaCl/HCl solution in the same aliquots, as mentioned above, was continued until the SPR band due to Au completely disappeared. The completion of the experiment was marked by adding a total of 3.2 mL NaCl/HCl solution for 5 mL NP solution. Two more batches of similar reactions were also carried out, separately – one by bubbling O_2 gas through the reaction mixture, while the other one was without O_2 bubbling.

Analytical Measurements. UV/Vis absorption spectra were recorded using a Hitachi U-2900 spectrophotometer. FTIR spectra, of discs of the sample prepared after mixing with KBr, were recorded using a Perkin Elmer Spectrum One Spectrometer. TEM sample was prepared by drop-coating dispersion onto Cu grid coated with carbon. Images were acquired using a JEOL JEM 2100 transmission electron microscope, operating at a maximum accelerating voltage of 200 kV. The samples for powder XRD were prepared by drying the dispersions onto glass cover slips. XRD data were acquired using a Bruker AXS D8 Advance X-ray diffractometer with $CuK\alpha_1$ radiation (λ ~1.54060 Å), operated at 40 kV and 40 mA.

3.2. RESULTS AND DISCUSSION

When lukewarm solution of pHA in water was allowed to cool down to room temperature, colorless precipitates of large particles were observed. TEM analyses revealed that these particles were of micrometer size and hence could not be used for core–shell particle generation. On the other hand, TEM analysis of the sample, prepared from the solution which appeared to become cloudy following cooling and stirring, exhibited the formation of uniform nanoscale particles. It may be added here that typical TEM sampling time was set at the onset of solution turning cloudy. A drop of the solution was placed on the grid which was then wicked away in 2 min. A typical image of the sample observed under TEM is shown in Figure 3.1a. As is clear from the micrograph, formation of well-defined isometric spherical particles having narrow size distribution took place. The average size

of the particles calculated from the image having an ensemble of over three hundred particles was found to be 8.8 ± 1.3 nm, which is more clearly manifested in the higher resolution image in Figure 3.1b. Further, a HRTEM image (inset in Figure 3.1b) showed the crystalline nature of the particles; the interfringe distance (*d* ~0.22 nm) corresponding to (103) planes of pHA crystals could be identified. Additionally, a SAED study, made by focusing the electron beam onto an area consisting of a few NCs clustered together, supported the formation of crystalline nanoscale particles (Figure 3.2a). The appearance of concentric rings was attributed to the merging of diffraction spots from more than one particle lying in close vicinity with each other. The *d*-spacings corresponding to the planes $(\bar{2}20)$, $(\bar{1}12)$, (103) and $(\bar{1}33)$ were found to be 0.36, 0.33, 0.22 and 0.19 nm in the crystal lattice of pHA. Further, a powder XRD pattern of the sample

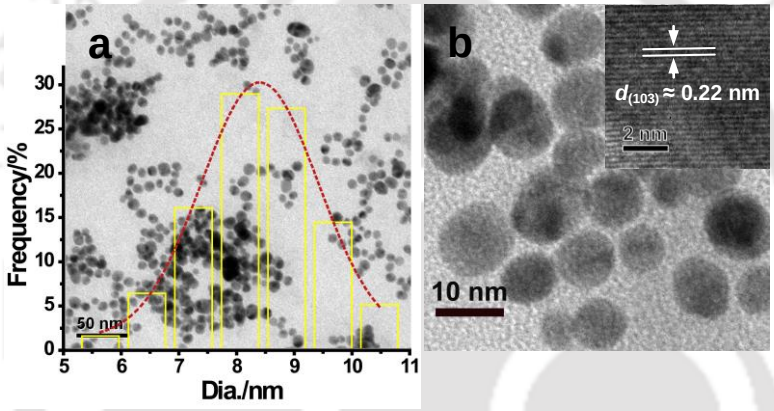

Figure 3.1. Low (a) and high (b) magnification TEM images of pHA NCs. Bar diagram in (a) is the size frequency distribution of the particles, while inset in (b) is the HRTEM image of a pHA NC showing interfringe patterns.

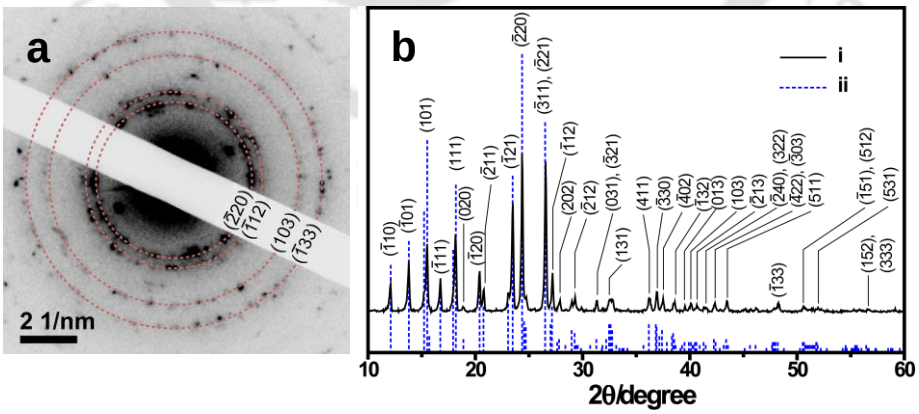

Figure 3.2. (a) SAED patterns of pHA NCs (obtained by focussing electron beam on a region of collection of NCs). (b) (i) Powder XRD patterns of pHA crystals which were obtained as precipitate from the supersaturated solution, and (ii) standard diffraction lines for monoclinic polymorph of pHA (data from JCPDS Card No. 39-1503).

(Figure 3.2b), obtained as a precipitate following a prolonged stirring of supersaturated pHA solution, showed the presence of planes due to a monoclinic polymorphic form of pHA. This was in agreement with the standard diffraction pattern of monoclinic pHA crystals (Figure 3.2b; data from JCPDS Card no. 39-1503). The XRD and SAED results were in concordance with each other. TEM investigation, therefore, along with SAED and XRD measurements clearly indicated the formation of rather uniform and small-sized NCs of pHA. It is important to mention here that the above results suggested that although in general larger crystals are known to form from the nucleation and growth of smaller crystals, careful timing of the samples could indeed help in trapping the formation of smaller and uniform NPs. Further, the concentration of pHA and the time of sampling for TEM were optimized herein for production of small and uniform NPs.

Since uniform and smaller pHA NCs could be formed and their presence in the medium could be probed indirectly, the generation of a core–shell structure with an inorganic metallic (Au) shell was pursued. This step required the immediate arresting of the NCs upon their formation by generation of an Au shell, as otherwise formation of larger pHA crystals would ensue. Therefore, addition of $HAuCl_4$ to the medium was started just prior to the solution becoming cloudy. Typically, the salt solution was added 30 s following cooling (and stirring) of the pHA solution. The colour of the solution at the early stage of $HAuCl_4$ addition was purplish that changed eventually to bluish with the complete addition of the salt solution. The results indicated the formation of Au NPs in the medium. Further, in order to study the dependence of coating thickness on the concentration of $HAuCl_4$ – if core–shell NPs were at all formed in the medium – three different experiments were performed by having different concentrations of $HAuCl_4$ in the media, while keeping the concentration of pHA the same. For instance, the concentrations of $HAuCl_4$ present in the media were 4.97×10^{-2}, 7.44×10^{-2} and 9.90×10^{-2} mM. The salt solutions were all added at about the same time following cooling and stirring of supersaturated pHA solution. The UV/Vis spectra of the solutions measured right after addition of $HAuCl_4$ to different media were rather broad (Figure 3.3a, i-iii). There was no clear difference in the extinction spectra for the three samples. The peaks appeared at 565 nm for all the three samples. Further, TEM investigations of the samples revealed formation of highly anisotropic star-shaped structures (Figure 3.3b) and the structures were similar for samples prepared from media containing particles obtained from all the three concentrations of $HAuCl_4$. Further, the intensity of the UV/Vis peak was higher for particles generated from a higher salt concentration. For instance, the value of extinction was 0.51 for a sample generated from $HAuCl_4$ concentration of 9.90×10^{-2} mM, while that was 0.21 for $HAuCl_4$ concentration being 4.97×10^{-2} mM. The positions for the extinction

maxima for all the three peaks indicated larger particle sizes. TEM results were commensurate with the UV/Vis spectral observations. It has been reported that larger particle sizes and particles with a non-spherical shape in the medium give rise to an SPR peak of Au NPs at wavelengths higher than typically observed for smaller average sizes – which is at around 520 nm. [346] That the particles were large and star-shaped led to the appearance of peaks at longer wavelengths. [347] Further, a TEM image even at higher resolution (Figure 3.3c) did not clearly reveal the presence of both pHA and Au in the NPs, although the lattice planes could vaguely be observed. However, inverse fast Fourier transform (IFFT) analysis of the HRTEM image of one such particle showed the presence of pHA crystal in addition to that of Au (Figure 3.3d). The *d*-spacing corresponding to planes of pHA could be identified apart from more closely spaced (111) planes due to *fcc* lattice of Au (*d* ~0.23 nm). This means that both pHA and Au were present in the same particle.

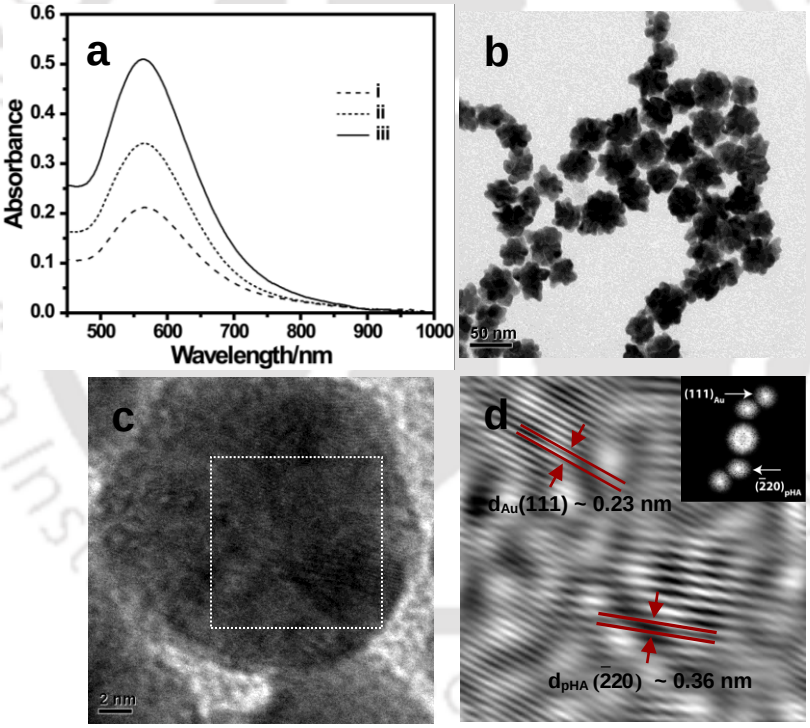

Figure 3.3. (a) UV/Vis spectra of as-made star-shaped Au NPs prepared with (i) 4.97×10^{-2}, (ii) 7.44×10^{-2} and (iii) 9.90×10^{-2} mM of $HAuCl_4$. (b) TEM image of the sample (iii) in (a), (c) HRTEM image of one single NP, and (d) IFFT image of the select region in (c) with the corresponding FFT image in the inset.

Additionally, when the solution containing the star-shaped particles was treated with CTAB, which was followed by centrifugation and redispersion, the plasmon band changed dramatically (Figure 3.4a, i-iii). The band became narrow and exhibited a sharp peak. In

addition, the band occurred at a shorter wavelength as compared to the spectrum for the sample before addition of CTAB. The behaviour of the plasmon band i.e., change in the presence of CTAB was similar for the Au NPs prepared from different concentrations of $HAuCl_4$. For example, the peaks appeared at 536, 530 and 544 nm for samples with a starting concentration of $HAuCl_4$ 4.97×10^{-2}, 7.44×10^{-2} and 9.90×10^{-2} mM respectively.

The role of CTAB as a shape-directing agent and in reshaping of the nanostructures is well-established. [347, 348] In the current experiments, addition of CTAB to the solution containing star-shaped Au NPs might have resulted in the dissolution of Au atoms at the tips (convex curvature) and re-deposition at the base with concave surface curvature. This eventually resulted into spherical and smaller particles. TEM results of the sample obtained following centrifugation and redispersion of CTAB treated solution of star-shaped Au NPs indicated the presence of spherical particles with variable contrast, indicative of the presence of core–shell particles (Figure 3.4b). The results were similar for different concentrations of $HAuCl_4$. It is to be added here that the presence of pHA NCs inside Au particles could not be discerned clearly at lower magnification in TEM. However, at a higher magnification the presence of smaller particles with a different contrast inside the larger particle could be observed (inset of Figure 3.4b). Further, the analysis of one such particle, obtained *via* IFFT of HRTEM image, revealed the presence of both Au and pHA crystals in the same structure (Figure 3.4c and 3.4d). The presence of pHA NCs could be visualized from the appearance of lattice fringes with a *d*-spacing of 0.48 nm, corresponding to its (111) planes, in addition to the presence of *fcc* Au lattice with a *d*-spacing of 0.23 nm for its (111) planes. Interestingly, the presence of fringes with wider separation due to pHA appeared to be lying underneath that of narrower Au fringes, in samples obtained both before and after CTAB treatment (Figure 3.3d and 3.4d). This suggested that the pHA crystals observed were present inside Au shells and not those which might have been deposited on the surfaces of the Au NPs. A comparison of pHA NCs present inside Au nanoshells with that of bare NCs (uncoated) also showed the similarity in size and spherical shape (Figure 3.4b *versus* Figure 3.1), thereby confirming the incorporation of pHA NCs inside Au NPs. For example, the typical size of the core particle in the core–shell was observed to be ca. 11 nm, whereas that for free pHA NCs was 9 nm. The formation of free Au NPs, devoid of pHA NC core, in the medium also could not be ruled out. Hence all of the particles observed in TEM did not show core–shell architectures. It may be added here that instances of incorporation of more than one pHA NC inside Au nanoshells could also be observed, as is clear from Figure 3.4b.

The particles were probably formed as follows. NCs of pHA were present in the medium in the form of small uniform spherical particles. The reduction of $AuCl_4^-$ ions by

pHA molecules yielded small Au NPs. It has been showed earlier [349, 350] that pHA reduces Ag^+ ions to produce Ag NPs as well as $AuCl_4^-$ ions to Au NPs, accompanied by the formation of a fluorescent dimer. A similar mechanism of reduction of $AuCl_4^-$ by pHA molecules may be occurring here. These Au NPs, because of their inherent instability, adhered onto the pHA NCs to have a lower surface potential, as reported earlier [146; refer also to Chapters 2 and 5]. It is possible that the particles were primarily formed on the surface of the pHA NCs. This was followed by further growth of Au resulting in the formation of a shell surrounding the pHA NCs (pHA@Au NPs). Further growth of the shell structures as well as deposition of smaller Au NPs generated in the medium resulted in larger star-shaped structures. It is plausible that the overwhelming concentration of pHA, which would be present in the medium in the form of crystals, was responsible for the formation of core–shell structures, in addition to the formation of individual Au NPs stabilized by either pHA or its dimer.

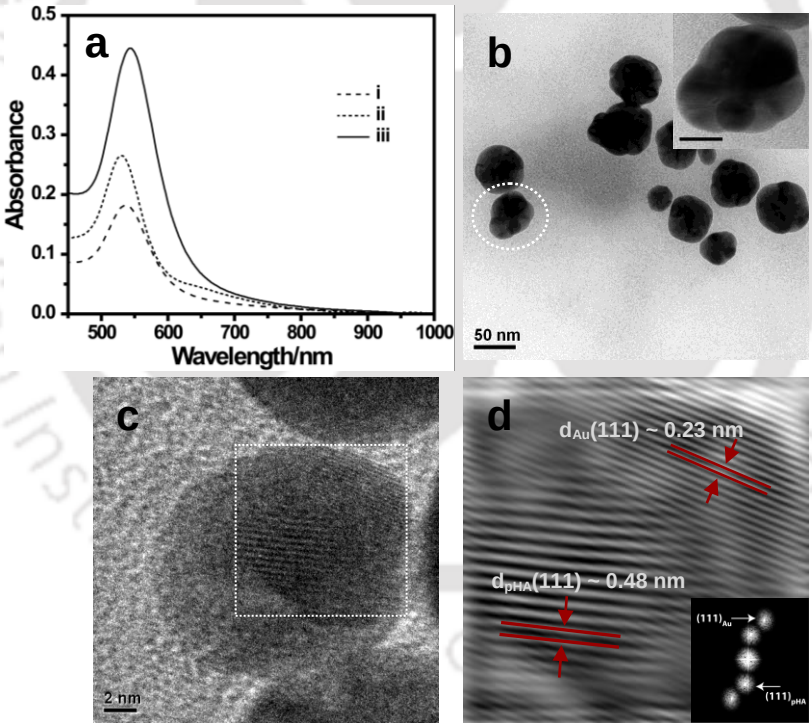

Figure 3.4. (a) UV/Vis spectra of solutions obtained following centrifugation and redispersion of CTAB treated star-shaped Au NP dispersion prepared with (i) 4.97×10^{-2}, (ii) 7.44×10^{-2} and (iii) 9.90×10^{-2} mM of $HAuCl_4$. (b) TEM image of the sample (iii) in (a) with an inset that is close up of the encircled particle (scale bar: 20 nm), (c) HRTEM image of a core–shell particle, and (d) IFFT image of the select region in (c) with the corresponding FFT image in the inset.

Further, SAED analysis on a core–shell particle was done. A typical SAED pattern recorded from a core–shell particle is shown in Figure 3.5a. It consisted of diffractions due to pHA crystals in addition to that from fcc Au NPs. The planes viz., $(\bar{2}20)$, $(\bar{1}12)$, (103) and $(\bar{1}33)$ could be indexed to pHA crystals, in addition to (220) and (311) *fcc* planes of Au. Powder XRD analysis of a pHA@Au NP sample, collected as precipitates following centrifugation of as-made pHA@Au NPs, was also carried out. It may be recalled here that the cycle of centrifugation and washing with water was carried out twice in order to minimize the presence of pHA crystals either free or deposited on Au shells. Figure 3.5b shows the diffraction profile of such a sample. Apart from diffractions due to *fcc* Au occurring at the angles 38.2, 44.4, 64.6, 77.6° (with reference to JCPDS standard data, Card no. 04-0784), diffractions due to pHA crystals could also be observed. The planes could be indexed to the monoclinic crystalline polymorph of pHA, as in Figure 3.2b. The

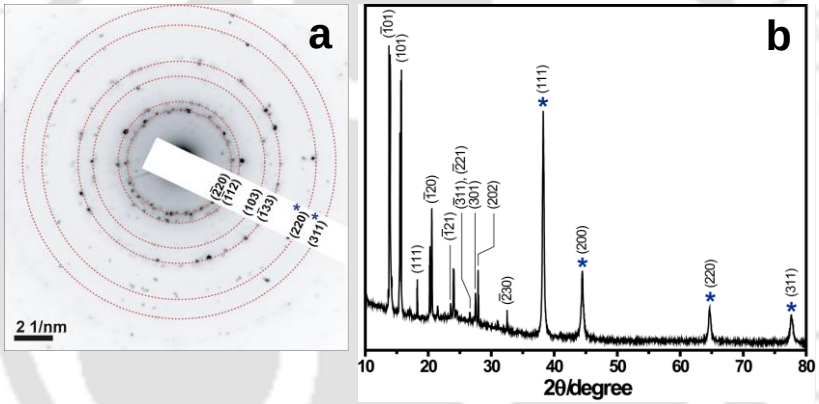

Figure 3.5. (a) SAED and (b) powder XRD patterns of pHA@Au NPs. Planes due to fcc Au are indicated by asterisks.

reflections from planes $(\bar{1}01)$, (101) for pHA and (111) for Au being dominant, other planes due to monoclinic pHA were significantly overwhelmed and could possibly not be observed. Overall, XRD measurements corroborated the presence of pHA and Au in the core–shell structures formed in the medium.

As mentioned above, following treatment with CTAB, pHA@Au NPs were subjected to centrifugation twice to ensure removal of excess pHA and CTAB from the medium. The pellet thus obtained was used for FTIR analysis. The results are shown in Figure 3.6a. The peak centered around 2920 cm^{-1} is due to C–H stretching of both methyl and methylene groups of CTAB and those at 3165 cm^{-1} and 3325 cm^{-1} are for N–H and O–H functional groups of pHA (Figure 3.6a, i). The occurrence of bands for the O–H and N–H stretch of pHA and C–H stretch of CTAB when compared to pristine pHA (Figure 3.6a, ii) and

pristine CTAB (Figure 3.6a, iii) evidenced that pHA and CTAB moieties were present in the core–shell NPs. This could mean that CTAB and pHA were possibly present outside the particle, acting as the stabilizers. It is difficult to imagine that pHA NCs present inside the crystal would give rise to FTIR spectral peaks.

The above results demonstrated the stabilizing of organic crystals of pHA within Au nanoshells. As Au is known to be generally non-toxic to mammalian cells, the particles could thus be potentially useful in the loading of drug molecules and their release in the body, if a suitable mechanism of systematic dissolution of Au or creation of pores could be achieved. However, CTAB-stabilized pHA@Au NPs would suffer from one drawback when attempted to be used in the biological system, as CTAB is known for its cytotoxicity [351, 352]. Hence, the core–shell particles needed to be made biocompatible prior to proposition for using in a biological environment. This was pursued by replacing CTAB

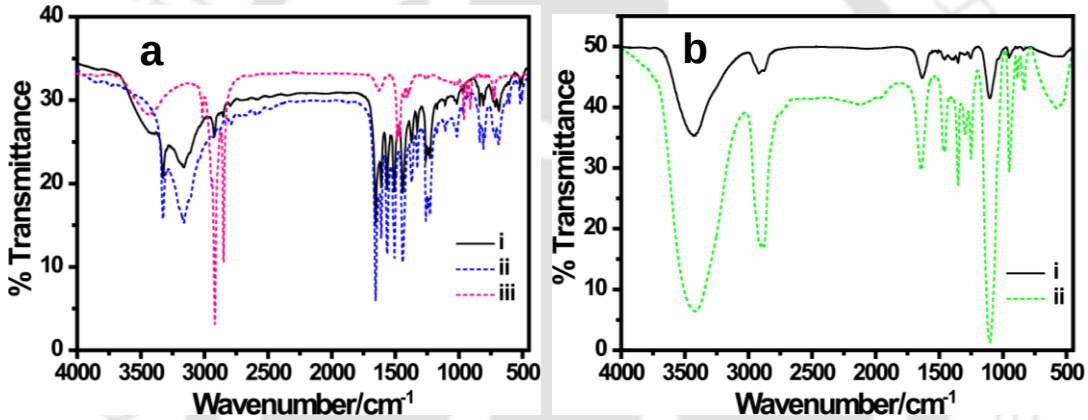

Figure 3.6. (a) FTIR spectra of (i) pHA/CTAB-stabilized pHA@Au NPs, (ii) pure pHA, and (iii) pure CTAB. (b) FTIR spectra of (i) PEG-stabilized pHA@Au NPs, and (ii) pure PEG.

moieties following treatment of the particles with PEG 400, which is a water-soluble biocompatible polymer used extensively in the realm of biomedical applications. In addition, PEG affords stability to the NPs by means of steric stabilization. [353, 354] FTIR spectrum of centrifuged and dried core–shell NPs after being treated with PEG showed the presence of peaks at 3430 cm^{-1} and 2920 cm^{-1}, corresponding to O–H and C–H stretching frequencies, identical to the spectrum of free PEG molecules (Figure 3.6b). Further, peaks neither due to pHA nor due to CTAB could be observed. The above observations indicated, thus, that CTAB and pHA moieties present on the outer surface of core–shell NPs were replaced by PEG molecules.

Further, in order to demonstrate the possibility of the core–shell NPs releasing pHA in a biological environment, a solution containing PEG-stabilized pHA@Au NPs was

treated with a solution consisting of an appropriate mixture of NaCl and HCl and having pH less than 3 (as described in section 3.1). It may be mentioned here that a solution of NaCl and HCl – having excess Cl^- ion – is known to etch metallic Au. [355] The UV/Vis spectra of pHA@Au NP solutions were recorded on treatment with different concentrations of NaCl/HCl solution. Initially, for pHA@Au NP solution as such, the maximum extinction at λ_{523} was recorded to be 0.41. On increasing the concentration of NaCl/HCl solution in the medium by adding each time 0.2 mL aliquots and allowing the solution to stir for 30 min following addition, the intensity of Au plasmon band was found to gradually reduce. It was also observed that the solution color changed from faint pinkish to colorless, which marked the etching of Au metal from the surface of pHA NCs. The etching of Au was complete in the presence of 3.2 mL NaCl/HCl solution when starting initially with 5 mL pHA@Au NP solution (with an extinction value of 0.41). The absence of metallic Au, in the form of a shell covering pHA NCs, was confirmed from the disappearance of the SPR band due to Au nanoshells. The dampening of the Au plasmon band as a function of NaCl/HCl concentration is given in Figure 3.7. Recording the

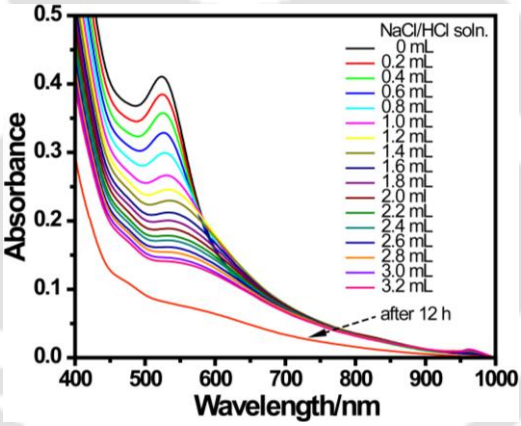

Figure 3.7. UV/Vis spectra of PEG-stabilized pHA@Au NPs at different concentrations of NaCl/HCl etching solution, as mentioned in the legends.

spectrum of the final solution after 12 h showed the Au plasmon band to be annulled completely (Figure 3.7, curve indicated with arrow). It may be mentioned here that the extent of the Au dissolution reaction was more pronounced when O_2 gas was bubbled through the reaction mixture than when carried out without additional gas. For this, to 5 mL pHA@Au NP dispersion, NaCl/HCl solution of chosen volume was added sequentially, along with bubbling O_2 gas through the reaction medium. Another batch of a similar reaction was also carried out in the absence of gas. The results are shown in Figure 3.8. As is clear from the figures (Figure 3.8a–c), the dissolution of Au NP was more

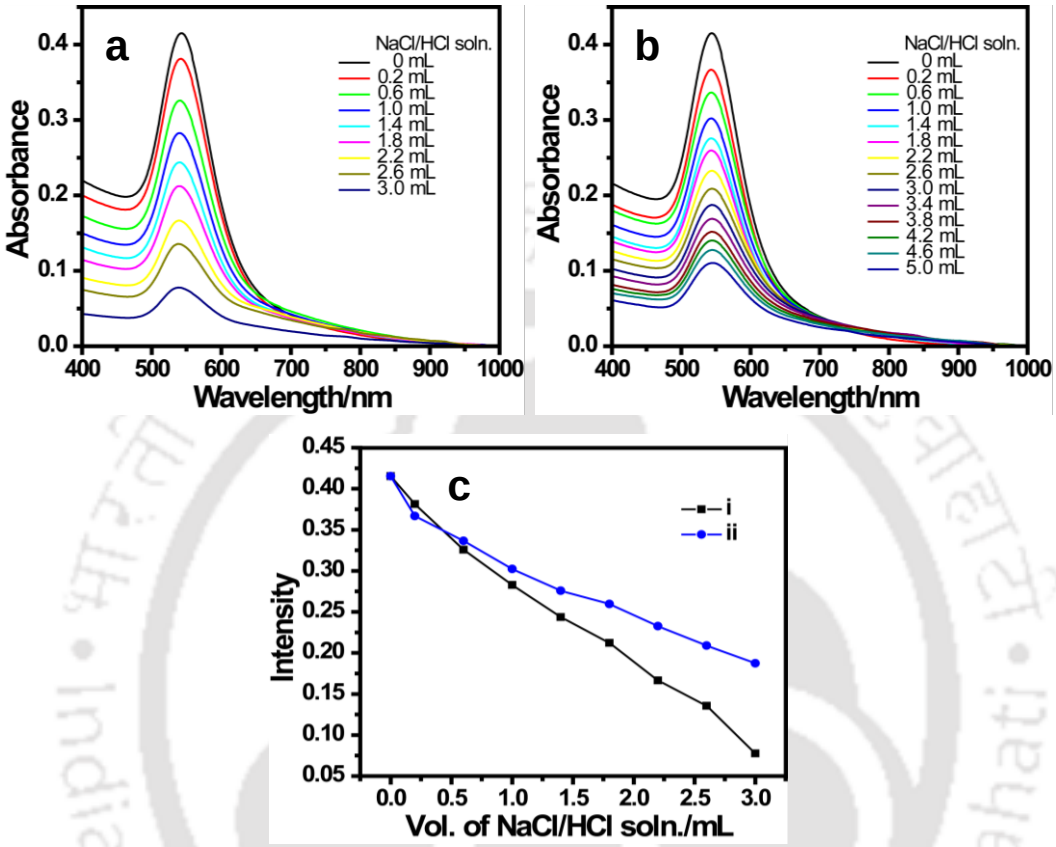

Figure 3.8. UV/Vis spectra of pHA@Au NPs at different concentrations of NaCl/HCl etching solution, (a) with and (b) without bubbling of O_2 gas through the reaction medium. (c) Plot of the peak intensities of absorbance bands, in (a) and (b), against the volume of NaCl/HCl solution added, shown here for 0–3 mL of NaCl/HCl solution; while (i) corresponds to data taken from (a), (ii) is that from (b).

facile in the presence of excess O_2. This suggests that in a strongly acidic medium and in the presence of excess Cl^-, the dissolved oxygen plays an important role in etching the Au shell. Based on the above observations and electrochemical potential, the following mechanisms could be proposed to be involved in removing the metallic (Au) shell from the core–shell particles.

Half-reactions for the oxidation of Au in the presence of oxygen (E° values being taken from standard reference):

$$O_2 + 4H^+ + 4e^- = 2H_2O \quad \text{... ... ... (1)} \quad E^0 = +1.23\ V$$

$$AuCl_2^- + e^- = Au^0 + 2Cl^- \quad \text{... ... ... (2)} \quad E^0 = +1.15\ V$$

$$AuCl_4^- + 3e^- = Au^0 + 4Cl^- \quad \text{... ... ... (3)} \quad E^0 = +0.93\ V$$

Combining reactions (1) and (2):

$$4Au^0 + O_2 + 4H^+ + 8Cl^- = 4AuCl_2^- + 2H_2O \quad \text{... ... ... (4)} \quad E^0_{rxn} = +0.08\,V$$

And combining reactions (1) and (3):

$$4Au^0 + 3O_2 + 12H^+ + 16Cl^- = 4AuCl_4^- + 6H_2O \quad \text{... ... ... (5)} \quad E^0_{rxn} = +0.30\ V$$

The large positive E° value of reaction (5) than reaction (4) shows that reaction (5) is more favorable, even though both the reactions are possible. Therefore, the oxidation reaction of Au in the presence of oxygen and higher concentrations of Cl^- and H^+ ions is spontaneous. Further, the reaction speeds up when carried out in the presence of excess oxygen (by bubbling O_2 gas through the reaction mixture) than in the aerial condition, as evident from Figure 3.8 above.

Furthermore, the species $AuCl_2^-$ is unstable and on formation undergoes disproportionation reaction to give $AuCl_4^-$ and Au° [355], as below:

Combining reactions (2) and (3):

$$3AuCl_2^- = AuCl_4^- + 2Au^0 + 2Cl^- \quad \text{... ... ... (6)}$$

with redox potential: $E^0 = E_1^0 - E_2^0 = +0.22\ V$

The positive value of E° suggests that reaction (6) is feasible, resulting in a decrease in the concentration of $AuCl_2^-$.

TEM observation of the PEG-stabilized pHA@Au NPs showed no change in size and shape (Figure 3.9a) with respect to that observed for the sample before treatment with PEG (Figure 3.4b). The shade observed surrounding the NPs could be due to PEG which could have been formed while drying of the liquid for TEM sample preparation. However, TEM investigation of a sample collected from the medium after addition of 1.2 mL NaCl/HCl solution (Figure 3.9b) showed reduction of the overall sizes of the NPs. This indicated the etching of Au from the surface of the core–shell NPs. In addition, flake-like structures could also be observed in the image. SAED analyses on a typical such flaky structure (Figure 3.9c) revealed the diffractions due to pHA crystals (Figure 3.9d). It can be surmised that the gradual dissolution of the Au shell could have led to controlled release of pHA moieties. It could also be possible that pores were first formed at the places of the thinnest shells followed by release of pHA.

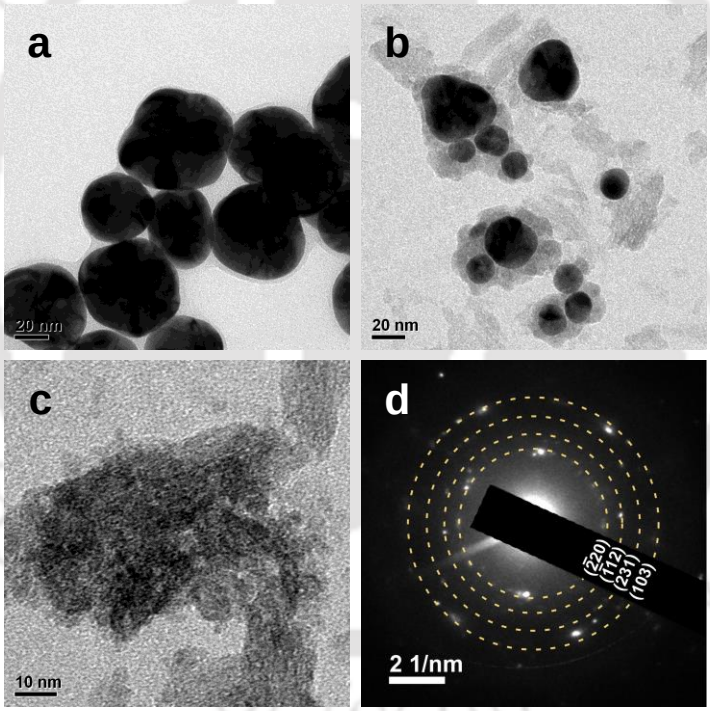

Figure 3.9. TEM images of PEG-functionalized pHA@Au NPs: (a) as-made, and (b) after partial etching of Au shell with NaCl/HCl solution. (c) TEM image and (d) SAED patterns of a flake-like structure in (b); the faint diffraction spots correspond to that of pHA crystals.

In order to further confirm the release of pHA moieties in the medium, FTIR study of the final solution (in its dried form) was carried out and the result is shown in Figure 3.10, i. It clearly demonstrated that the spectrum had the signature of stretching frequencies

for the N–H and O–H bonds in the regions 3187 and 3330 cm^{-1} respectively, due to pHA moieties, in addition to the presence of PEG molecules having bands at 2926 and 3424 cm^{-1} due to C–H and O–H bonds, respectively. Further, the finger-print region of the spectrum matched significantly that of free pHA molecules. For the sake of comparison, spectra of pure pHA and pure PEG are also shown in Figure 3.10, ii and Figure 3.10, iii respectively. The experiments thus indicated the release of pHA molecules from the core–shell NPs on the etching of Au shell.

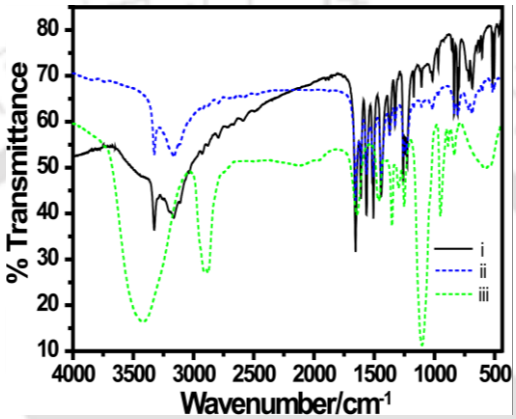

Figure 3.10. FTIR spectra of (i) NaCl/HCl etched pHA@Au NP solution (in its dried from), (ii) pure pHA, and (iii) pure PEG.

It may be mentioned here that the release of pHA moieties following etching of Au shell, by the process described above, could probably be mediated in the stomach (*in vivo*). Gastric acid, formed in the stomach, is a digestive fluid that has a pH of 1.5 to 3.5. [356, 357] It is composed of hydrochloric acid and ions like Na^+ and K^+, providing an ideal environment for the etching of the Au shell and thereby the release of pHA molecules. The slow rate of dissolution of the Au shell in the present method has the kernel of a model drug delivery vehicle, with releasing drug slowly at the site for increased potency.

3.3. CONCLUSIONS

In summary, spherical and uniform NCs of an organic molecule (pHA) was generated in the aqueous medium. The pHA NCs so generated were as such not stable in the aqueous dispersion, being prone to precipitation following growth into larger crystals. However, addition of $HAuCl_4$ to the medium containing pHA NCs generated a new kind of crystalline core–shell material with Au surrounding the pHA NCs. HRTEM investigations

clearly demonstrated the encapsulation of pHA NC inside Au shell. Interestingly, the shell could be etched away by treatment with a solution containing a mixture of NaCl and HCl. This opens up a new concept for delivery of drug molecules by encapsulating them inside inorganic nanoshells and with further appropriate functionalization, having the possibility of slow and targeted release, engendered with high local concentration at the delivery site. The method could possibly be extended to form core–shell NPs of drugs or biomolecules (such as proteins). However, this would depend on the ability for reduction of $AuCl_4^-$ by the moiety and also on the ease of crystallization of the molecule in the medium. The key advantage of such a structure would be that the drug molecules contained inside the metallic shell, in the form of a crystal, will have their chemical and biological properties intact and be stable against degradation at the normal ambience. With the advent of nanotechnology several methods have been developed on the delivery of drugs but encapsulating nanocrystalline drugs within metal NPs has remained a challenge. While it is understood that the current way may not yet be perfect for practical implementation, the findings may pave the way for more research in this direction and bring in brand new ideas of drug encapsulation, delivery and release, using organic–inorganic hybrid crystalline nanostructures.

Chapter 4

Linear Assembly of Nanoparticles

While Chapters 2 and 3 described the generation of 0D NPs, this chapter is on the formation of 1D linear assembly of nanoparticles (NPs). The contents of this chapter are from a published paper¶. Citrate-stabilized Au NPs were assembled into chain-like arrays of superstructures by using *p*-aminoacetanilide (pAA) as a mediator (Scheme 4.1). Au NPs of different sizes were used in the assembly formation. The extent of the assembly formation depended on the concentration of pAA in the medium. Higher concentration led not only to the formation of longer assemblies but also branched ones. UV/Vis spectra showed the appearance of a second peak at a longer wavelength – the position of which shifted to the red with increasing pAA concentration. Furthermore, the second peak could not only be influenced by the concentration of pAA but also by choosing different sizes of the NPs at the initial stages. For example, when the particles were larger the shift could be observed at longer wavelengths than those starting with smaller particles.

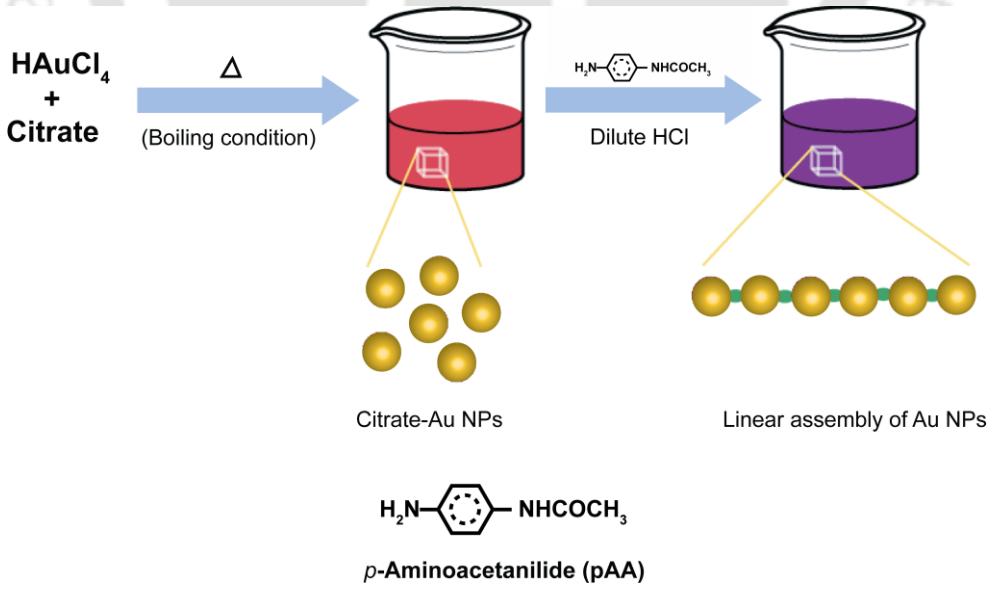

Scheme 4.1. Representation of the assembly formation of Au NPs on treatment with pAA.

¶[Das *et al. J. Chem. Sci.* **2008**, *120*, 547–555] - Reproduced by permission of Springer http://link.springer.com/article/10.1007%2Fs12039-008-0084-2

4.1. EXPERIMENTAL

Materials. Hydrogen tetrachloroaurate ($HAuCl_4.3H_2O$, 17% Au in HCl, Sigma-Aldrich), trisodium citrate (Merck), *p*-aminoacetanilide (Merck) and hydrochloric acid (Merck) were all used as received without further purification. Milli-Q grade water with a resistivity of 18.2 $M\Omega.cm^{-1}$ was used in all the experiments. All glassware and magnetic stir bars used were cleaned with aqua regia and rinsed with Milli-Q water prior to start of experiments.

Synthesis of Au NP colloid. Aqueous Au NPs of diameters 10 to 40 nm were prepared according to the method of Frens, [26] using the reduction of $HAuCl_4$ by trisodium citrate. A mixture of 494 μL of 25.3 mM $HAuCl_4$ aqueous solution and a definite amount of water was taken in a two-necked round-bottom flask fitted with a condenser and the mixed solution was heated on a hot plate with continuous stirring. When the solution started boiling a measured amount of 1% (w/v) trisodium citrate solution was added under continuous stirring. Within 20 s of boiling the solution turned faint blue which then changed readily to red after around 50 s, indicating the formation of Au NPs. Boiling was allowed to continue for another 30 min in order to have complete reduction of Au^{3+} ions. The resulting red colored solution was taken out from the hot plate and cooled to room temperature. By this procedure Au NPs of different sizes were prepared by varying the amount of citrate solution. The solutions were used for further studies. The concentration of $HAuCl_4$, amount of citrate solution, and the pH of the final solutions are given in Table 4.1. The particle sizes were calculated from TEM images.

Table 4.1. Details of data related to size-selective synthesis of Au NPs.

Sample No.	Volume of $HAuCl_4$ solution (25.3 mM) (mL)	Volume of citrate solution (1% w/v) (μL)	Total volume of solution (μL)	Citrate conc. (mM)	pH of resulting solution	Avg. size of Au NPs (nm)
1	494	1600	50	1.10	5.2	11.2 ± 2.7
2	494	1000	50	0.69	4.2	25.3 ± 4.3
3	494	875	50	0.60	3.2	33.1 ± 3.0
4	494	750	50	0.51	3.7	38.5 ± 5.0
5	494	625	50	0.43	3.4	39.6 ± 7.2

Preparation of pAA solution. A given amount of pAA was added to 10 mL water, such that the concentration was 33.3 mM, and the mixture was warmed so as to dissolve all the solid pAA. The solution was allowed to cool down to room temperature and its pH was adjusted to 2.0 by addition of conc. HCl.

Mixing aqueous pAA with citrate-capped Au NPs. 2.5 mL of the as-prepared

Au NP solutions were taken each in five different vials. To each of these solutions, a given amount of pAA was added. The color of the solutions changed from red to purple for a meager concentration of pAA and then to blue on increasing the concentration of pAA. The final pH of the solutions was found to be 3.5. It may be mentioned that the amount of the different Au NP solutions were kept constant. The final concentrations of pAA are given in Table 4.2.

Table 4.2. Variation of λ_{max} of LSPR band with concentration of pAA.

Conc. of pAA (mM)	λ_{max} (nm) of LSPR band for pAA treated Au NP solutions synthesized with different citrate concentrations (mentioned in rows)				
	1.10 mM	0.69 mM	0.60 mM	0.51 mM	0.43 mM
0.40	637	742	670	-	733
0.60	648	754	672	679	864
0.78	677	786	793	799	896
0.97	679	809	815	830	911
1.15	683	820	830	852	937
1.34	687	822	838	858	937
1.52	687	843	846	859	937
1.70	693	843	850	859	937

Analytical Measurements. UV/Vis spectra of the samples were recorded using Perkin Elmer Lambda 45 spectrophotometer. FTIR spectra were measured using Perkin Elmer Spectrum One spectrometer in the range of 450–4000 cm^{-1} with a resolution of 4 cm^{-1}. The sample for pAA-treated citrate-stabilized Au NPs was prepared by the addition of 5.4 mL pAA solution (33.3 mM) to 100 mL of citrate ion capped Au NPs (size 11 nm); the solution was subjected to centrifugation at 15,000 RPM at 10 °C. The pAA-capped Au NPs was collected as a precipitate and the precipitate was washed with excess water to remove any uncapped pAA molecules. The precipitate was subsequently dried and then mixed with KBr to record FTIR spectrum. Similarly, pure solid pAA was mixed with KBr to make the pellet for FTIR measurement. Transmission electron microscopy (TEM) measurements were performed using JEOL JEM 2100 transmission electron microscope operating at a maximum acceleration voltage of 200 kV. The TEM samples were prepared by placing a drop of a solution on a carbon-coated copper grid (400 mesh) followed by evaporation of the solvent at room temperature.

4.2. RESULTS AND DISCUSSION

Citrate-stabilized Au NPs of different sizes were prepared by the well-known Frens'

method. [26] In this method, citrate ion is used as a reducing agent as well as capping agent for Au NPs. The variation of concentration of citrate ions produces spherical Au NPs of different sizes. In the present set of experiments, the concentrations of $HAuCl_4$ and citrate used and pH of the media are mentioned in Table 4.1. Also mentioned in Table 4.1 are the average particle size produced in the medium. The particle sizes were measured by TEM and a few sample images are shown here for brevity. TEM measurements indicated the presence of uniform spherical Au NPs in the solution. As is clear from the table, larger sized particles were produced when the concentration of the citrate ion was lower. The average sizes of the Au NPs produced were measured to be 11·2 ± 2·7 nm, 25·3 ± 4·3 nm, 33·1 ± 3·0 nm, 38.5 ± 5.0 nm and 39·6 ± 7·2 nm in the presence of 1·10, 0·69, 0·60, 0.51 and 0·43 mM citrate concentrations respectively. The results are similar to the observations of the previously published article. [26] The UV/Vis spectra of different sizes of Au NPs are shown in Figure 4.1. As is clear from the figure, the spectra consisted of a single peak in the visible region with the maximum absorption appeared at longer wavelengths with decrease in citrate concentration. For example, when the citrate ion concentrations used were kept at 1·10, 0·69, 0·60, 0·51 and 0·43 mM, the maxima occurred at 519, 529, 530, 536 and 545 nm respectively. This also means that with increasing particle size the peak shifted to the longer wavelengths. The increase in particle size is known to be responsible for the shift in the absorption maximum due to Au NPs. Thus the method allowed production of uniform and spherical NPs with well-defined sizes, which is responsible for further study in the present context with respect to the formation of assemblies. The as-made Au NP dispersions, prepared by varying citrate concentration, are shown in the inset of Figure 4.1. The color of the solutions changed from ruby red (for 1.10 mM citrate) to purple (for 0.43 mM citrate) on reducing the concentration of citrate in the reaction media.

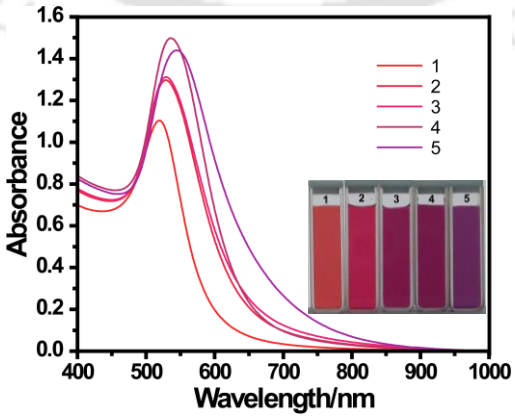

Figure 4.1. UV/Vis spectra of citrate-stabilized Au NP dispersions prepared with different concentrations of citrate (**1**: 1.10, **2**: 0.69, **3**: 0.60, **4**: 0.51, **5**: 0.43 mM).

Addition of pAA into citrate-stabilized Au NPs of different sizes led to a gradual change of color of the Au NPs. The UV/Vis spectra of the solutions were recorded immediately after addition of pAA to the Au NP solutions. The resulting spectra are shown in Figures 4.2a–e. The amount of pAA added to each solution and consequent appearance of a second peak and subsequent changes in its position are indicated in Table 4.2. Both the spectra and the data present in the table clearly indicate that the appearance of a second peak is the consequence of the addition of pAA. Further, when the concentration of pAA was gradually increased the second peak started appearing at increasingly longer wavelengths in all samples. The appearance of this peak at longer wavelength can be ascribed to the longitudinal SPR (LSPR) band due to possible assembly formations of Au NPs. Interestingly, increasing the concentration of pAA did not lead to continuous increase. On the other hand, at above certain concentrations of pAA, the shifting of the second peak stopped to occur. The exact concentration of pAA for which the shift of the longer wavelength stopped changing depended on the size of the NPs. Such concentrations are mentioned in Table 4.2.

Interestingly, it was observed that with the increase in the concentration of pAA in the Au NP solutions, the shifting of the second peak was more pronounced for larger particles than for smaller particles, as can be realized from Figures 4.2a–e. For example, when 0·780 mM concentration of pAA was added into 11 nm citrate stabilized Au NPs, the LSPR band shifted to 677 nm in comparison to the peak at 637 nm at the pAA concentration of 0·395 mM. For the same concentration, the shifting of the second peak could be observed at 786, 793 and 896 nm for Au NPs of sizes 24 nm, 33 nm and 40 nm respectively (refer to Tables 4.2 and 4.1). The above observation suggests that appearance of the second peak is not only dependent on the concentration of pAA but also dependent on the size of the Au NPs. Further, the plot of the concentration of pAA *versus* shift of the λ_{max} of the LSPR band of the Au NPs is shown in Figure 4.2f and the details of data are available in Table 4.2. In all cases, the increase in the shift was significant when the concentration of pAA was lower. At higher concentrations the change seemed to level off. Interestingly, the change was more significant when the starting particles were larger. This result indicates that while increasing the concentration of pAA with different sizes of Au NPs the λ_{max} of the second peak shifted to much longer wavelengths when starting with larger particles. Also, the intensity of the first SPR band gradually decreased while that of the second SPR band increased with the increase in concentration of pAA in the Au NP solutions as shown in Figure 4.2. This was valid up to a certain limiting concentration of pAA beyond which there was either no change or both the intensities decreased possibly due to precipitation. However, the change in intensities is indicative of formation of assemblies with possible

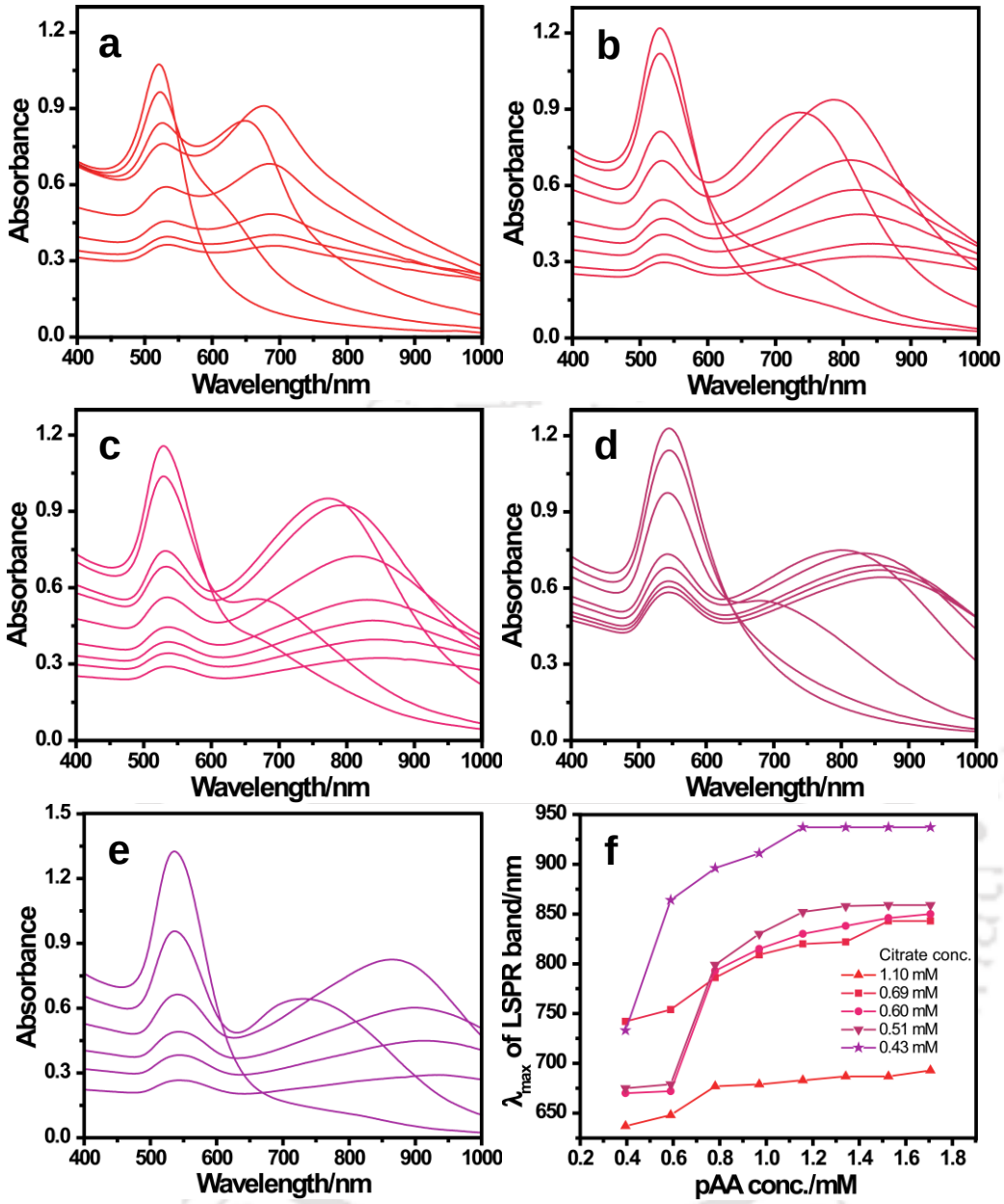

Figure 4.2. (a–e) UV/Vis spectra for different pAA-treated citrate-stabilized Au NP solutions: concentrations of citrate in the corresponding solutions were in (a) 1·10 mM, (b) 0·69 mM, (c) 0·60 mM, (d) 0·51 mM and (e) 0·43 mM. (f) is the plot of λ_{max} of LSPR band of different Au NPs for different concentrations of pAA (refer to Table 4.2).

increase in the length of the assembly upon increasing the amount of pAA. This means that the number of Au NPs involved in assembly formation increases and hence the length of the assembly increases and number of available free NPs decreases. However, after a particular concentration of pAA there is no shifting of the second SPR band as further Au NPs are not available for assembly formation. This result also reflects the formation of unidirectional self-assembly, which is responsible for the localized surface plasmon

resonance (LSPR) band at longer wavelengths. What is interesting in these assemblies is the opportunity to have tunable optical absorption not only according to the length of the assembly but also the diameters of the constituents of the assemblies i.e., Au NPs. Changing the diameters changes the effective length of the assembly for differently sized NPs even at the same pAA concentration. Also, that the extent of redshift of the longitudinal SPR can be extended with higher diameter Au NPs adds to the advantage of the method. In an earlier study it was observed that addition of acetanilide to a solution of citrate stabilized Au NPs led to organization of the NPs into linear chain-like arrays. The appearance of a second peak corresponding to the formation of arrays was similar to the present observations. In the present set of experiments, however, the results suggest that a judicious choice of particle size and concentration of pAA could be used to achieve more tunable optical properties of the organized NPs. Also, the intensities of the LSPR occurring at higher wavelength are prominent and the peaks are nearly isolated. On the other hand, the LSPR peaks in the case of acetanilide added Au NPs were less prominent and were part of a broad spectrum with two peaks. In addition, it is interesting to observe that the concentration of pAA required for the formation of assembly was much lower than that of acetanilide. For example, the appearance of the (second) LSPR peak could be observed at a pAA concentration of 0·59 mM. On the other hand, the second peak could be observed at a minimum concentration of acetanilide being 6·4 mM. These indicate that properties of individual molecules could be used in organizing NPs and tune their optical properties. Water soluble pAA consists of an additional $-NH_2$ group (from that of acetanilide), which can be protonated under acidic pH and which contributes to organization of NPs at a lower concentration in comparison to that of acetanilide. In other words, both molecules contain $-NHCOCH_3$ group that leads to organization of citrate capped Au NPs, while the additional $-NH_2$ group present in pAA facilitates the formation of assembly at even lower concentration. It may be that at acidic pH both $-NH_2$ and $-NHCOCH_3$ groups of pAA get protonated, which makes it easier to partially replace the citrate capping and also facilitates the formation of dipoles necessary for the unidirectional organization of the NPs.

The assembly formation was further established from the observations made upon TEM measurements of various samples. The results are shown in Figure 4.3. Typically, it shows well-dispersed Au NPs without any orderly arrangement before the addition of pAA (Figures 4.3a–e). The apparent agglomeration that can be seen in the figures possibly occurred during the evaporation of the samples. On the other hand, the TEM micrographs of the samples prepared after addition of pAA revealed that the Au NPs were assembled primarily into chains (Figures 4.3f–l). It also demonstrates that by increasing the concen-

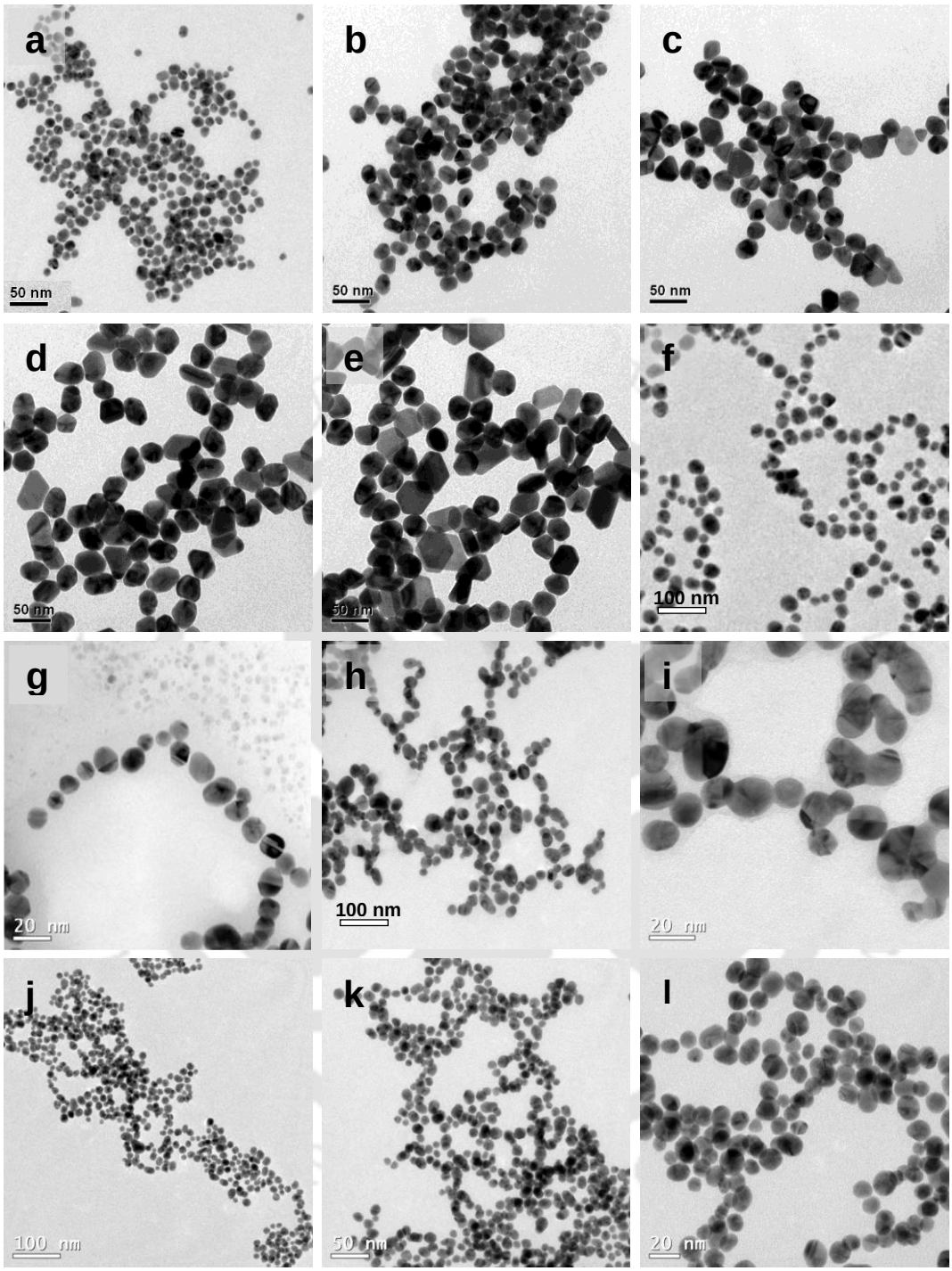

Figure 4.3. (a–e) TEM images of citrate-stabilized Au NPs prepared by the Frens' method [26]: Concentrations of citrate were in (a) 1·10 mM, (b) 0·69 mM, (c) 0·60 mM, (d) 0·51 mM and (e) 0·43 mM. (f)–(l) are the TEM images on addition of different concentrations of pAA to citrate-stabilized Au NPs: (f), (h) and (j) are the images when 0·395, 0·780 and 1·706 mM pAA were respectively present in Au NP solution prepared with 1·10 mM citrate. (g) and (k) are different views of the images taken at 0·395 and 1·706 mM of pAA-treated Au NPs, respectively. (i) and (l) are the magnified views of regions in (h) and (k) respectively.

tration of pAA in the medium, the chain length of the assemblies gradually increased. However, at higher concentrations significant branching of the assemblies occurred. It is also interesting to note that at higher concentrations of pAA substantial fusion of particles had occurred (Figures 4.3h–l). It is important to mention here that in the case of acetanilide induced organization although branching was observed there was substantial presence of linear chains in the branched structures. [186] On the other hand, when pAA was used the presence of linear chains in the branched structures was minimal. Instead, clustering of particles could be observed to appear more prominently at higher concentrations of pAA. Also, significantly higher level of fusion of adjoining particles seemed to have taken place in comparison to those organized using acetanilide. The branching of the assembly and subsequent fusion of the assembled particles possibly is the reason for the observation of no change in the UV/Vis peak positions beyond certain concentrations of pAA, as the length of the assembly did not increase further; on the contrary, branching had occurred.

Formation of the assembly of stabilized NPs is known to occur based on dipole-dipole interaction. [187, 209] In the present case that would involve the citrate-stabilized Au NPs and the protonated-pAA. The linear assembly formation can take place when the strength of the dipole-dipole interaction exceeds the Coulombic interaction between the Au NPs and the citrate ions. In citrate-stabilized Au NPs the citrate ions are bound to the surface of each NP and so the NPs are covered uniformly with negative charges. After the addition of protonated-pAA, citrate ions from most of the NPs could be partially replaced by the added pAA. This changes the uniform charge distribution and generates polarity on each NP (as shown in Scheme 4.2). Each Au NP now becomes a dipole and because of dipole-dipole interaction two NPs could form a dimer. Once dimers are formed the integrative dipole moment of the dimer exerts an attractive force stronger than that between two individual Au NPs, causing chain growth. As a result, the preformed chains act as a template and facilitate the addition of additional free Au NPs to the end of the chains via dipole-dipole interactions. This dipole-dipole interaction might be the driving force for the formation of a linear chain of Au NPs. Beyond a certain critical chain length, the interaction energy decreases because of the interaction at a junction which creates extra entropy. Also, when the chain length is sufficiently long there could be additional formation of branched dipoles from one of the Au NPs acting as the head of the larger branch. The dipolar nature of the chains of the citrate-stabilized Au NPs makes them stable in the medium. [188]

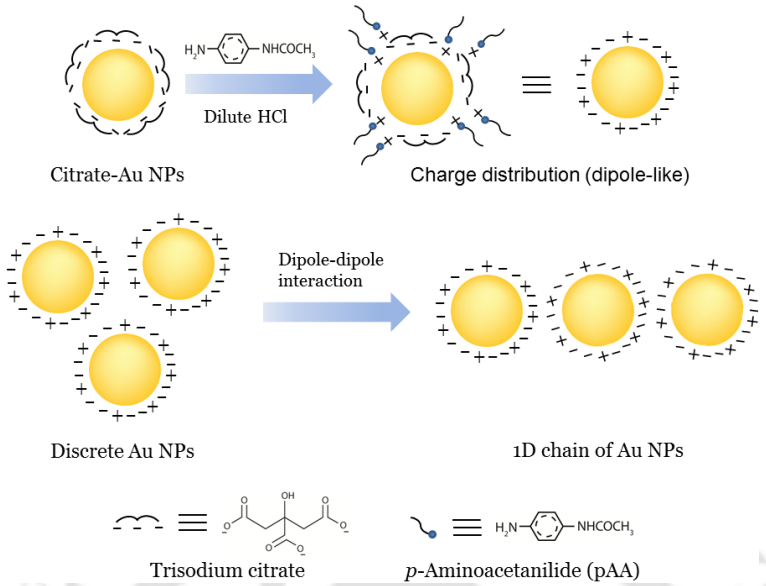

Scheme 4.2. Illustration of the mechanism of assembly formation of citrate-stabilized Au NPs on treatment with pAA.

In order to understand better the nature of pAA in the assembly formation, FTIR measurements of the samples were carried out. The results are shown in Figure 4.4. Figure 4.4, i is the FTIR spectrum of pAA dried from the medium containing pAA-treated Au NPs; whereas the spectrum of as-purchased pAA is shown in Figure 4.4, ii. Figure 4.4, i shows a broad peak in the region of 1640 cm^{-1} due to the characteristic peak of amide-I stretching vibration. The low intensity peak around 1541 cm^{-1} is due to the amide-II N–H band. But the sharp peak at 1514 cm^{-1} for the amino group at the para position in the

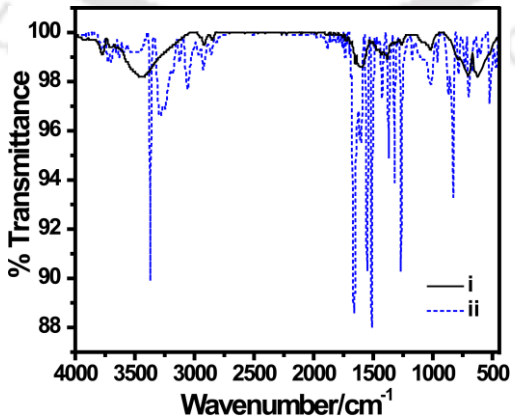

Figure 4.4. FTIR spectra of (i) pAA in the presence of Au NPs, and (ii) pure pAA.

benzene ring remains same for both the samples. The additional peaks in the region of 3300–3400 cm^{-1} are due to the N–H stretching vibration. This result suggests that pAA molecules were attached to the surface of the Au NPs.

4.3. CONCLUSIONS

In conclusion, it has been shown that citrate-stabilized Au NPs could be assembled into a chain-like array by treatment with pAA solution at an acidic pH. The assembly formation is attributed to the appearance of a second LSPR band, in addition to the original band of Au NPs, in the UV/Vis spectra. The appearance of the second band has been ascribed to the formation of assembly and its shift is due to formation of longer assemblies. The assembly formation has further been corroborated by TEM studies. Quite interestingly the level of organization and also the second SPR band of Au NPs could be tuned not only by varying the concentration of pAA but also by changing the particle sizes of the Au NPs. This provides a much better control over assembly formation as there are now two parameters available instead of one that has been in use recently. Also, it is important to note that the NPs could be assembled using a concentration of pAA that was lower than that of acetanilide used in earlier experiment. Further, while branching occurred in the assembly using both the molecules, clustering of particles seems to be more prominent in the case of using pAA. In addition, fusion of the assembled NPs at higher pAA concentrations was more prominent, indicating properties associated with the molecules i.e., the presence of an additional $–NH_2$ group. The present method of organizing NPs using molecule such as pAA may lead to much more control over organization of NPs into hierarchical superstructures based on molecular interactions.

Chapter 5

Inorganic–Organic Hybrid Composite Crystals

Keeping in view of using interaction between nanoparticles (NPs) and organic molecules, as in Chapter 4, generation of 3D architectures of NPs is mentioned in this chapter. The work presented here has been published in an international journal¶. The formation of hybrid composite crystals (3D) comprising of inorganic Au NPs and organic *p*-hydroxyacetanilide (pHA) is discussed. The crystals could be grown out of an aqueous mixture of Au NPs and pHA at 35 °C. The dimensions of the crystals were on the order of a few millimeters and the optical properties of Au NPs were retained in the crystals. Further, when the solution containing NPs and pHA was centrifuged (to remove excess pHA) followed by redispersion into water smaller crystals (of a couple of millimeters in length) were formed with the highest content of NPs. In addition, optical microscopic investigations indicated existence of plasmonic origin colored centers due to Au NP crystals akin to color centers that are known to appear due to defects in otherwise colorless crystals. The color that appeared was dependent on the ratio of Au NPs to pHA. Thus by varying the ratio of Au NPs to pHA in the original medium two types of crystals (referred to as Process I and Process II) were obtained, as shown in Scheme 5.1.

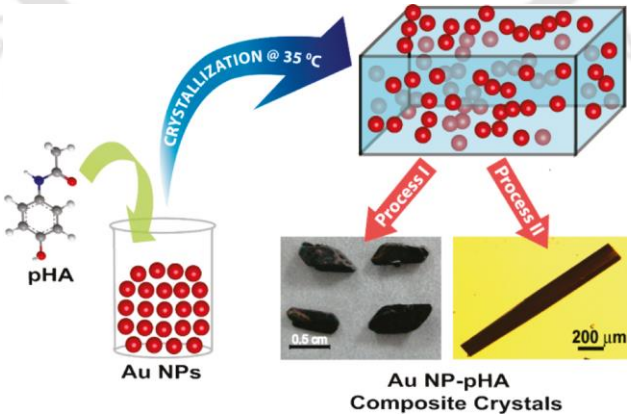

Scheme 5.1. Representation of the process involving growth of composite crystals of Au NPs and pHA. (The images at the bottom right are the photographs/micrographs of the as-grown crystals. Process I involved crystallization from the solution as such with excess pHA, whereas Process II involved crystallization from solution containing a mixture of Au NPs and pHA which was subjected to centrifugation before and thus the concentration of pHA was low.)

¶Reproduced with permission from [Das *et al. Langmuir* **2010**, *26*, 15714–15717] Copyright [2010] American Chemical Society http://pubs.acs.org/doi/abs/10.1021/la1034867?prevSearch=%255BContrib%253A%2Bsubhojit%2Bdas%255D&searchHistoryKey=

5.1. EXPERIMENTAL

Materials. Hydrogen tetrachloroaurate ($HAuCl_4.3H_2O$, 17% Au in HCl, Sigma-Aldrich), trisodium citrate (Merck) and *p*-hydroxyacetanilide (Merck) were all used as received without further purification. Milli-Q grade water with a resistivity of 18.2 $M\Omega.cm^{-1}$ was used in all the experiments. All glassware and magnetic stir bars used were cleaned with aqua regia and rinsed with Milli-Q water prior to start of experiments.

Synthesis of Au NP colloid. To a definite volume of water (~ 46.7 mL), 1.25 mL of $HAuCl_4$ solution (10^{-2} M) was added and the mixed solution was refluxed under stirring condition. As the solution started to boil, 2 mL of freshly prepared trisodium citrate solution (1% w/v) was added, so that the final volume of the solution was 50 mL. The solution turned blue in about 20 s and then to ruby red color in another 40 s, indicating thereby the formation of Au NPs. The resulting solution was allowed to boil under refluxing condition for another 30 min to allow for the complete reduction of Au^{3+} ions.

Growth of Au NP–pHA composite crystals. To 50 mL of Au NP dispersion 3.31 x 10^{-2} M pHA dissolved by warming the solution. The mixed solution was kept in an incubator at 35 °C, undisturbed. About 5 days later, large crystals typically on the order of tens-of-millimeters were formed (Process I). In another batch, prior to crystallization, the mixed solution of pHA and Au NPs was centrifuged at 20,000 rpm for 20 min in order to have excess pHA, citrate and any other ions removed from the solution. The pellet so obtained was redispersed in ca. 5 mL water under mild sonication. The solution was subjected to crystallization at a slower rate of evaporation (in incubator maintained at 35 °C) in a container having a perforated cover. After around 5 days, millimeter-sized needle-shaped crystals were formed (Process II). The crystals obtained by both the processes were washed with water and used for analyses.

For comparative studies, pristine pHA crystals had also been grown by dissolution of pHA in water followed by crystallization at 35 °C in incubator; this was used as the control sample.

TEM sample preparation. The composite crystals were etched i.e., washed off partially with water, air-dried and then ground to powder. The powder was dispersed in cyclohexane and the suspension so obtained was drop-cast on carbon-coated copper TEM grid and dried in ambience. The sample was then deemed ready for measurement.

Analytical Measurements. UV/Vis spectra were recorded using Perkin Elmer Lambda 25 and Hitachi U–2900 spectrophotometers. FTIR spectra of the samples were recorded, by forming discs with KBr, using a Perkin Elmer Spectrum One spectrometer. Thermogravimetric analyses (TGA) was performed by using SDT Q600 TA instrument at a heating rate of 10 °C/min in a nitrogen atmosphere. Optical microscopy images were

acquired with a Carl Zeiss Axioskop 2 Mat Microscope fitted with a digital camera. TEM images were acquired using a JEOL JEM 2100 transmission electron microscope operating at a maximum accelerating voltage of 200 kV. Atomic force microspcopy (AFM) images were acquired using a VEECO Multimode atomic force microscope, connected with a Nanoscope IVa controller. Powder XRD experiments were performed using a Bruker AXS D8 Advance X-ray diffractometer with Cu $K\alpha_1$ radiation (λ= 1.54060 Å), operated at 40 kV and 40 mA. X-ray crystallography data were collected using a Bruker SMART APEX-II CCD diffractometer, equipped with a fine focus 1.75 kW sealed tube Mo Kα radiation (λ= 0.71073 Å) at 298(3) K with increasing ω (width of 0.30 per frame) at a scan speed of 3 s/frame. The SMART software was used for data acquisition.

5.2. RESULTS AND DISCUSSION

When citrate-stabilized Au NPs dispersed in water – synthesized by a procedure based on the classical Turkevich method [24, 25] – was mixed with pHA and the mixture was left in an incubator at 35 °C, large deep red-colored crystals could be seen to have formed at the bottom of the container in about 4 to 5 days. Single crystal XRD studies of the Au NP–pHA crystals evidenced the formation of crystals corresponding to monoclinic (form I) [358] and orthorhombic (form II) [359] polymorphs of pHA. The details of crystallographic data are available in Table 5.1. Thus, the crystals consisted of periodic units due to those of pHA crystal and no additional periodicity due to the presence of Au NPs was observed. Further, the observation of cell parameters corresponding to those of pHA crystals indicated that the presence of Au NPs did not alter the parameters of the crystal. Finally, it was interesting to observe that the crystals obtained following Process II

Table 5.1. Crystallographic data for polymorphs I (monoclinic) and II (orthorhombic) in the Au NP–pHA composite crystals.

Parameters	I	II
Formula	$C_8H_9NO_2$	$C_8H_9NO_2$
Formula weight	151.16	151.16
Crystal system	Monoclinic	Orthorhombic
Space group	P21/n	Pbca
a (Å)	7.1070(2)	11.8321(4)
b (Å)	9.3917(3)	7.4032(3)
c (Å)	11.7225(3)	17.1585(6)
α (deg)	90.00	90.00
β (deg)	97.4030(10)	90.00
γ (deg)	90.00	90.00
V (Å)	775.92(4)	1503.01(10)
Z	4	8

were predominantly orthorhombic, whereas those obtained using Process I were of mixed types consisting of monoclinic and orthorhombic polymorphs, indicating that at the higher ratio of Au NPs to pHA crystallization into the orthorhombic form might have been favored.

The UV/Vis spectrum of as-made citrate-stabilized Au NPs showed an extinction maximum at 520 nm region (Figure 5.1a). The NPs were spherical in shape and had a narrow size distribution, as evident from TEM micrograph in Figure 5.1b. The UV/Vis spectrum of the Au NP–pHA solution, containing lower ratio of concentration of Au NP and pHA, that was used to grow crystals by Process I (Figure 5.2a) appeared to be identical, in terms of line position and shape, to the spectrum of as-made Au NP solution (Figure 5.1a). However, the spectrum of the Au NP–pHA solution, having lesser concentration of pHA (or higher ratio of concentration of Au NPs to pHA), used to grow

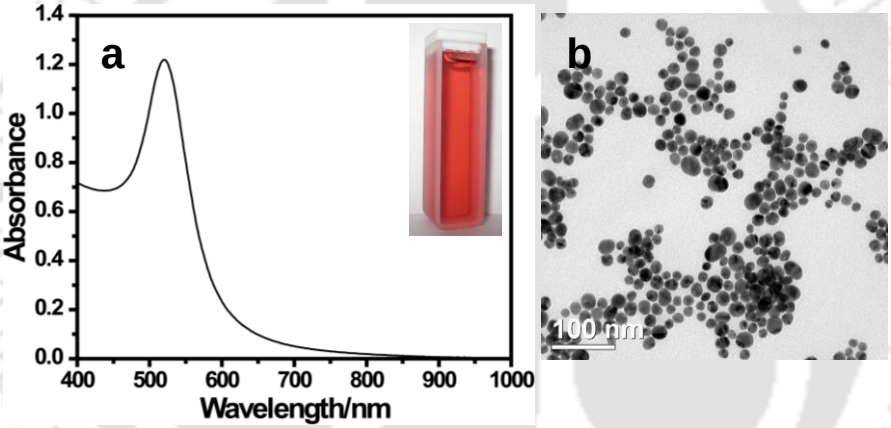

Figure 5.1. (a) UV/Vis spectrum and (b) TEM micrograph of as-made citrate-stabilized Au NPs (avg. particle size: 16.8±3.5 nm). Inset in (a) is the photograph of the Au NP solution.

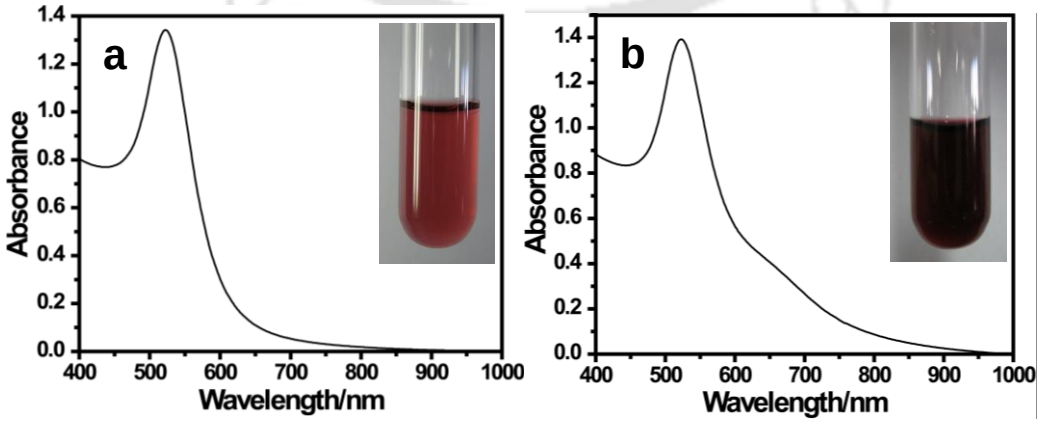

Figure 5.2. UV/Vis spectra of Au NP–pHA solutions used to grow crystals by (a) Process I and (b) Process II. Insets in (a) and (b) are the photographs of the Au NP–pHA solutions.

crystals by Process II exhibited a small shoulder at around 670 nm (Figure 5.2b) – in addition to the usual Au NP SPR band at the region of 520 nm – indicating presence of a low level of agglomeration of NPs prior to crystallization.

UV/Vis spectrum of the powdered composite crystals (obtained by Process I) exhibited an SPR band corresponding to Au NPs at 538 nm (Figure 5.3a), which showed around 18 nm bathochromic shift when compared with the SPR band of as-synthesized citrate-stabilized Au NPs (Figure 5.1a). There was also a shift in the peak position with respect to the composite crystals when they were redispersed in water, in which case SPR band occurred at 532 nm (Figure 5.3b). In addition, there was a small shoulder present at 622 nm indicating discernible agglomeration of some of the NPs present in the crystal (also evident from Figure 5.3b, for the band at 682 nm). The dielectric environment of Au NPs in the pHA crystal is fundamentally different from its water dispersion, even in the presence of pHA. The difference could give rise to the observed shift in the wavelength of extinction maximum. On the other hand, when pHA in the presence of Au NPs was subjected to crystallization, it is plausible that some of the NPs were agglomerated during the process and the agglomerated particles would give rise to a net redshift in the extinction maximum. Further, since pHA stabilized the NPs electrostatically it might be that at its lower concentration agglomeration of NPs was favored. In addition, the same would be responsible for the appearance of the second peak at longer wavelength. Upon redispersion of the crystals into water, the dielectric environment of the individual NPs would revert back; however, the agglomerated particles will remain as such and thus the net effect would be a blueshift in the extinction maximum (Figure 5.3b) in comparison to that in the original spectrum (of crystals, Figure 5.3a) and the occurrence of a second peak

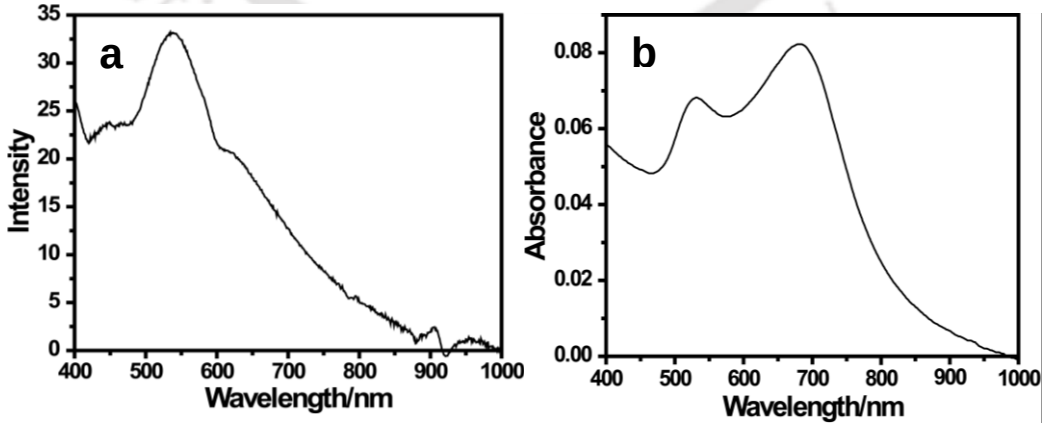

Figure 5.3. UV/Vis spectra of (a) Au NP–pHA composite crystals (in the powder form), recorded in the reflectance mode, and (b) re-dissolved crystals in water. The crystals mentioned in (a) and (b) were generated by Process I.

at longer wavelength due to the agglomerated particles. It may also be possible that upon redispersion into water (only) due to very low concentration of pHA further agglomeration in comparison to those in the crystals could occur leading to a great shift in the longitudinal plasmon resonance (observed to be occurring at 682 nm as shown in Figure 5.3b).

FTIR spectrum of the composite crystal (obtained following Process II) vis-à-vis that of pHA crystal indicated attachment of –NH of pHA to the Au NPs, thus either partially or fully replacing citrate. This was evident from the shift of the peak due to N–H stretching to 3208 cm^{-1} (Figure 5.4, i) in the composite crystals with respect to pure pHA (3168 cm^{-1}, Figure 5.4, ii), a result similar to that observed in Chapter 2 (refer to Section 2.2).

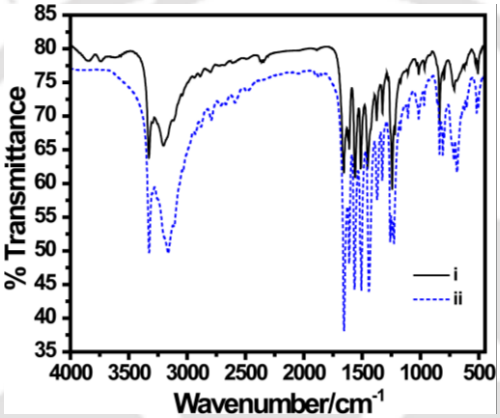

Figure 5.4. FTIR spectra of (i) Au NP–pHA composite crystals (grown by Process II), and (ii) pure pHA.

TEM images of powdered crystals indicated the presence of NPs dispersed well in pHA matrix for the crystals obtained by Process I and Process II (Figure 5.4). Further, the TEM results also suggested that incorporation of Au NPs in the crystal was aperiodic, which could also be random. In addition, the presence of some NPs in close proximity could be observed (both in Figure 5.4a, and Figure 5.4b) , being possibly responsible for the second peak in the UV/Vis spectrum (Figure 5.3a). It is well-established that when NPs either agglomerate or are very close to each other, a second peak at a longer wavelength appears [360] and thus the peak at 622 nm is due to close proximity of the NPs in the crystals. SAED patterns obtained from both the crystals indicated the presence of NPs in close proximity in the crystals. AFM image of a composite crystal indicated the presence of particles, being clustered together on the surface (Figure 5.5a). It may be mentioned here that for AFM measurements the crystals were partially etched by keeping them in water and hence the surface images observed here were those of undissolved surface present

originally deep inside the crystal. Corresponding AFM image of pristine pHA crystal (Figure 5.5b) indicated rather smooth surface and devoid of particulates that were otherwise present in the composite crystal. The above-mentioned results indicated that Au NPs were present in the composite crystals and they were incorporated inside the crystals, some of which might have been close together to form clusters. Under ordinary circumstances, during the process of crystallization of pHA from the solution containing Au NPs, there ought to be phase separation and crystals of pHA should ideally precipitate out of the medium. This may lead to agglomeration of bare NPs, which were originally electrostatically stabilized by pHA. However, because of high surface free energy of the NPs, they might be attached to the growing surfaces of the crystals onto which further growth of pHA crystal might be possible. It is also plausible that the surfaces of Au NPs stabilized by pHA might facilitate crystallization of pHA. Also, smaller crystals might fuse with each other to grow into bigger ones. During the process of crystallization, the depletion of surface pHA on Au NPs might happen, which might lead to agglomeration of

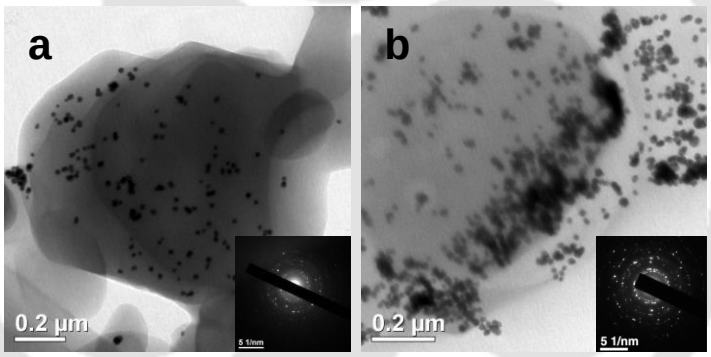

Figure 5.4. TEM micrographs of ground form of Au NP–pHA composite crystals generated by (a) Process I and (b) Process II. Insets in (a) and (b) are the SAED patterns obtained from the respective crystals.

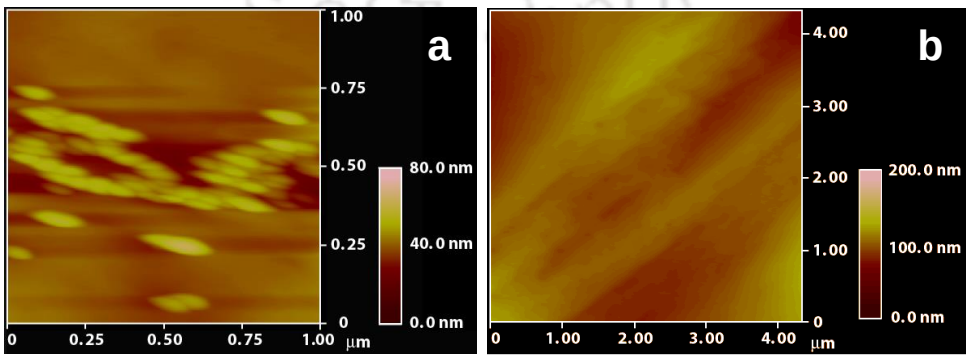

Figure 5.5. AFM images of (a) Au NP–pHA composite crystal (obtained by Process I), and (b) pure crystal of pHA only.

NPs to a certain extent. The agglomerated particles would be part of the growing crystals and thus would exhibit the plasmonic properties of assembled NPs with extinction of light having maximum wavelengths higher than that due to single particle only and the wavelength would depend on the extent of agglomeration. The extent of agglomeration would depend on the ratio of Au NPs to pHA present in the original medium. Higher pHA concentration would provide necessary stabilizers (i.e., pHA molecules) to the NPs even during crystallization resulting in smaller level of aggregation. On the other hand, when the concentration of pHA would be low there may not be sufficient pHA to stabilize all the NPs during crystallization and thus would lead to greater agglomeration of the NPs.

TGA of the ground form of composite crystals (generated from Process I and Process II) did not show any significant change in the decomposition temperature of pHA in the presence of Au NPs. The curves showed only one weight-loss step at around 250 ^{o}C (Figure 5.6) corresponding to combustion of pHA, as indicated by the decomposition curve of pHA only. Also, from the figure, it is clear that ca. 1 and 3% Au (by weight) were present in the Au NP–pHA crystals, which were derived by Process I and Process II, respectively. XRD of the powdered composite crystals (obtained using Process I and Process II) indicated the presence of Au NPs as diffraction due to *fcc* lattice planes (111), (200), (220) at 2θ values of 38.4, 44, 64.5^{o} occurred, respectively (Figure 5.7). Further, diffraction patterns due to the presence of crystalline pHA could be observed at the same positions (in addition to peaks occurring at other angles). It is to be mentioned here that the diffraction lines due to Au NP lattice planes were significantly overwhelmed by that due to pHA diffraction. This was due to the presence of lesser content of Au NPs than pHA in the composite crystals (as evidenced from TGA results presented above). As a result, prominent lines due to Au NPs in the crystals were not observed. Also, if present

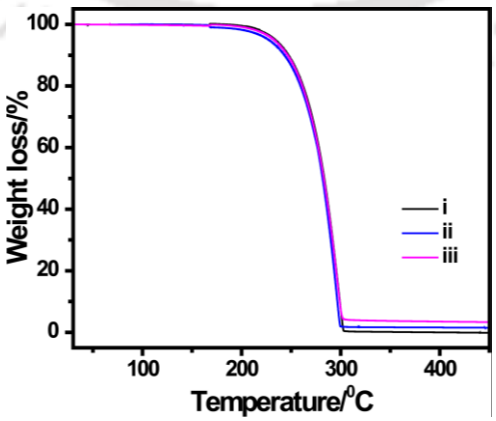

Figure 5.6. TGA thermograms of (i) pHA, and Au NP–pHA crystals obtained by (ii) Process I and (iii) Process II.

they were superimposed by the pHA diffraction lines which occur at the same positions. However, the peaks at 38.4, 44 and 64.5° were broader in the composite crystals in comparison to those in the crystal of pHA, the broadness being due to the presence of nanocrystalline Au.

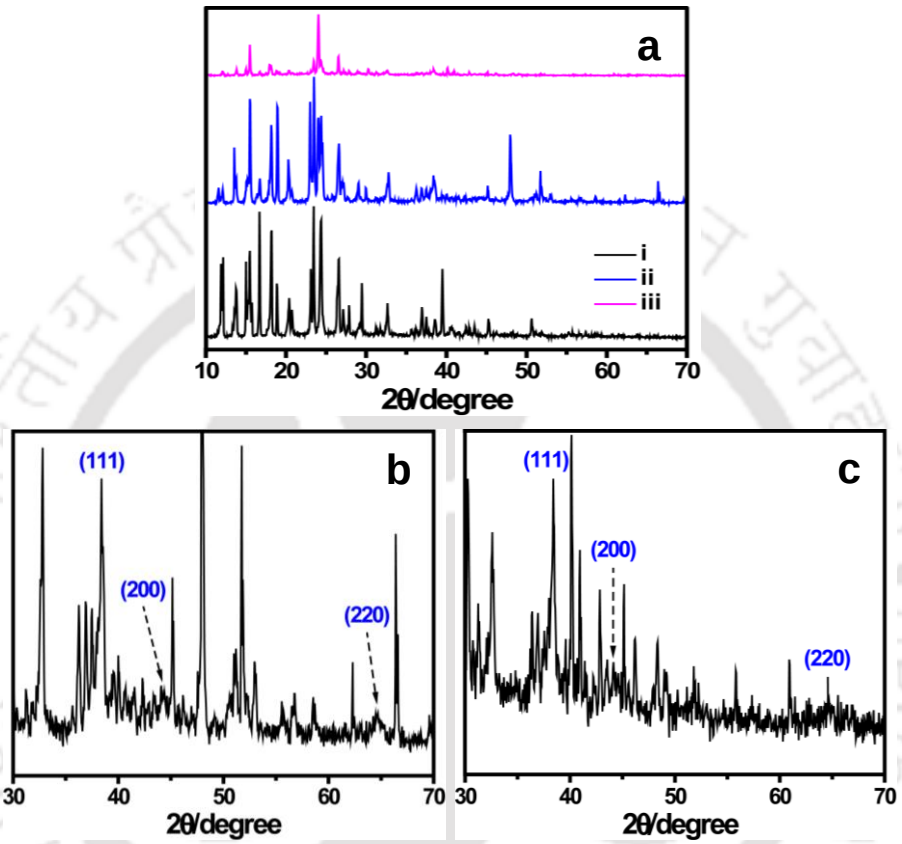

Figure 5.7. Powder XRD patterns of (a, i) pHA, and Au NP–pHA crystals obtained by (a, ii) Process I and (a, iii) Process II. (b) and (c) are the expanded views of (a, ii) and (a, iii) respectively, in the 2θ range from 30–70°.

Finally, when the ground form of Au NP–pHA composite crystals was observed under optical microscope in reflection mode, specific colors due to the presence of Au NP crystals were observed. A collection of such images is shown in Figure 5.8. As is clear from the images, a ruby red color is seen in the crystals (Figure 5.8a, b), which were generated with excess pHA in the original medium (Process I), a photograph of which is shown in the inset of Figure 5.8a. On the other hand, when the as-prepared Au NP and pHA solution was subjected to centrifugation and then redispersion (a photograph of which is shown in the inset of Figure 5.8c) followed by crystallization (Process II), a purple color

was observed in the composite crystals (Figure 5.8c, d). In other words, in the presence of excess pHA, the NPs retained their original color and there was possibly no further significant fusion of NP crystals during the process of crystallization of pHA along with them. In contrast, in the presence of lesser amount of pHA in the medium, considerable fusion of NPs might have occurred during crystallization and thus the appearance of color characteristics of larger NP crystals. TEM images of the ground crystals of the two kinds (Figures 5.4a, b) further corroborated the observations. Further, it has been observed that the solid dry crystals were stable for weeks in the atmosphere without any visible change in color or texture, indicating no further change in the agglomeration behavior following crystallization. Thus by controlling the concentration of pHA in the medium prior to crystallization, one could possibly control the plasmonic properties of the composite crystals owing to varying proximities of the NPs present in the solid. Further, since pHA crystals are optically transparent under ideal conditions, the NPs of Au present throughout the crystals ought to be optically active and exhibit plasmonic behavior. A powerful laser light ought to be able to penetrate the crystal and interact with the NPs on its path. On the other hand, the weak light of the UV/Vis diffuse reflectance probe may only be able to interact with the NPs present on the surface and in addition may be with a

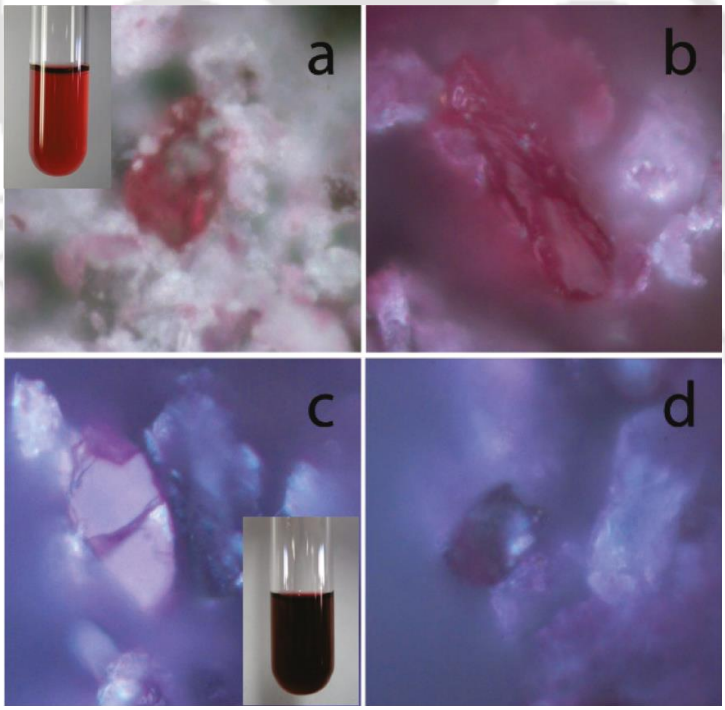

Figure 5.8. Optical microscopy images of Au NP–pHA composite crystals (in their ground form) obtained by (a, b) Process I and (c, d) Process II. Insets in (a) and (c) are the photographs of Au NP–pHA solutions from which the crystals were obtained.

few layers below. Again, optical microscopy might only reveal the interaction of light with the NPs present on the surface of the crystal. The advantage here is that even if the top layer is removed by etching or other means the plasmonic behavior of the NPs present on the next exposed layer would again bring in characteristic color or extinction property.

5.3. CONCLUSIONS

In conclusion, a new hybrid inorganic–organic composite crystalline material has been generated, wherein the NPs were present not only at the surfaces of crystals but were also embedded deep inside. It is fascinating to note that crystals of organic molecules such as those of pHA could be host to foreign crystals such as those of Au NPs, which are tens of nanometers in diameters. It is to be further noted that previous observation [146] indicated that NPs such as those of Au could be deposited on the surfaces of an organic crystal without compromising the crystallinity of the host. In the present case, it could be rationalized that hosting of NPs inside the crystal is akin to simultaneous deposition of NPs on two surfaces of the crystal (with the exception that it is the same crystal here). The novelty here is that a crystal could be grown out of pHA in water in the presence of Au NPs, where the NPs were incorporated inside the crystal without changing the crystal lattice of the host and maintaining the plasmonic signatures of the NPs. And the crystal motif as well as the plasmonic properties of the NPs inside the crystal could be controlled by the ratio of NPs to pHA. That inorganic NPs could be incorporated inside an organic crystal brings newness to an observation that might lead to the generation of newer and well-defined composite crystals, whose properties could be tuned based on the properties of the molecules and the NPs and the combination of the two.

Chapter 6

Supercrystals of Nanoparticles

With the endeavor to generate higher order superstructures of nanoparticles (NPs), as discussed in Chapters 4 and 5, 2D as well as 3D supercrystals of magnetic NPs, viz., Fe_3O_4 and Fe_3O_4@Au, were generated. This chapter discusses the formation of such crystals and of their properties. To start with, oleic acid-stabilized Fe_3O_4 NPs were generated by the high temperature decomposition of Fe-oleate complex (Scheme 6.1). This yielded uniform and spherical NPs. They were then treated with polyethylene glycol (PEG, MW 6000) and the dispersion in chloroform medium was suspended under the influence of an external magnetic field. Following evaporation of chloroform, dark brown flake-like crystals were obtained. TEM studies revealed Fe_3O_4 NPs being organized in the form of 2D and 3D superstructures. The magnetic behavior of the crystals was ascertained using vibrating sample magnetometer (VSM) measurements. Further, the work was extended with Au-coated Fe_3O_4 (Fe_3O_4@Au) NPs. In the case of Fe_3O_4@Au NPs, the supercrystals in addition to being magnetic in nature showed optical properties due to presence of nanometer-sized Au.

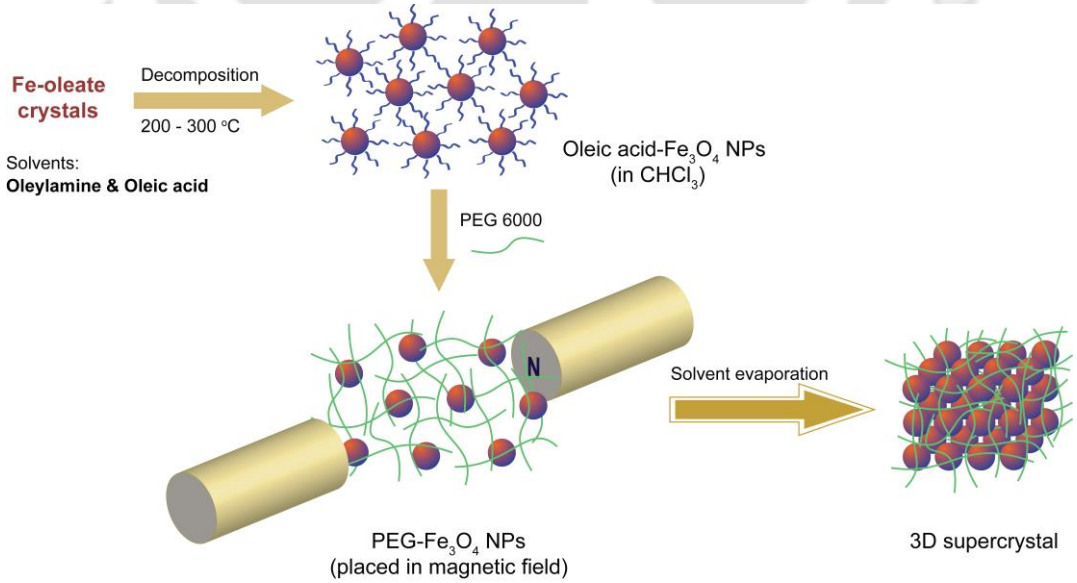

Scheme 6.1. Cartoon showing the synthesis of Fe_3O_4 NPs and growth of their supercrystals by suspending them in an external magnetic field.

6.1. EXPERIMENTAL

Materials. Ferric chloride hexahydrate ($FeCl_3.6H_2O$, Merck), sodium oleate (Na-oleate, Loba Chemie, India), oleylamine (National Chemicals, India), oleic acid (Merck), hydrogen tetrachloroaurate ($HAuCl_4.3H_2O$, Sigma-Aldrich), hexane (Merck), chloroform (Merck), polyethylene glycol (PEG 6000, Merck) and ethanol (TEDIA) were used as received without further purification. All glassware and magnetic stir bars used were cleaned with aqua regia and rinsed with Milli-Q water prior to start of experiments.

Synthesis of Fe-oleate complex. 3.24 g $FeCl_3.6H_2O$ and 18.25 g Na-oleate were dissolved in a solvent mixture consisting of 15 mL ethanol, 18 mL hexane and 8 mL water. The resulting solution was heated at a temperature of 70 °C for 4 h. Upon completion of the reaction, a precipitate separated out into the upper organic layer. The precipitate was washed with water and ethanol 4–5 times and dried in the air to obtain shiny dark brown crystals that were analysed by FTIR and TGA and DSC measurements. Using the Fe-oleate complex as precursor, Fe_3O_4 nanoparticles (NPs) were synthesized as described below.

Synthesis of Fe_3O_4 NPs. The as-synthesized Fe-oleate complex (300 mg) was dissolved in a 3:1 mixture of oleylamine and oleic acid and the mixture was heated under reflux for 1 h at 120 °C when the solution colour became dark. The temperature was raised to 200 °C, during which nitrogen gas was blown through the reaction mixture. The solution was allowed to heat under magnetic stirring for 2 h more at 300 °C. After the completion of reaction, the crude product was precipitated by adding ethanol. It was washed around 4 times with hexane and ethanol and then redispersed in chloroform. The TEM studies of the dispersion showed the formation of Fe_3O_4 NPs.

Synthesis of Fe_3O_4@Au NPs. The synthesis of Fe_3O_4@Au NPs was carried out by following a reported protocol, [68] with slight modification. A 1 mL Fe_3O_4 NP solution, taken from the as-prepared dispersion of Fe_3O_4 NPs, was diluted to 10 mL with chloroform and to which 500 μL oleylamine was added. 5 mL $HAuCl_4$ solution (10^{-2} M) was added drop wise and the mixture was left to stir for 20 h. After this time, the colour of the solution appeared reddish. The resulting solution was washed by centrifugal precipitation twice: at 15 000 rpm (whose precipitate discarded) and at 25 000 rpm – the precipitate to which was redispersed in 20 mL chloroform. The TEM experiments revealed the successful synthesis of core–shell Fe_3O_4@Au NPs.

Growth of supercrystals of Fe_3O_4 NPs and Fe_3O_4@Au NPs. To 1 mL chloroform dispersion of Fe_3O_4 NPs in a test tube, 15 mg PEG dissolved and the mixed solution was covered with a perforated aluminum foil. The test tube containing the solution was placed upright between the poles of an electromagnet (Figure 6.1). A

constant magnetic field of 0.19 T was allowed between the poles, such that the magnetic flux was perpendicular to the NP solution. After about one day, crystals in the form of solid crust formed at the bottom of the test tube. Crystals were also grown from the dispersion of Fe_3O_4 NPs under 0.09 and 0.12 T magnetic fields. In addition, for the sake of comparative studies, crystals were also grown in the absence of external magnetic field. It is to be noted that all the experiments mentioned in the article were each carried out with a 1 mL dispersion of Fe_3O_4 NPs and 15 mg PEG, unless mentioned otherwise.

Likewise, crystals of Fe_3O_4@Au NPs were obtained, when starting with 1 mL Fe_3O_4@Au NP dispersion and 15 mg PEG, in the presence (0.19 T) and absence of magnetic field.

Analytical Measurements. UV/Vis spectra of liquid samples were recorded in Hitachi U–2900 Spectrophotometer, while that of solid samples in Perkin Elmer Lambda 750 using an integrating sphere. FTIR spectra, of discs of the sample prepared after mixing with KBr, were recorded using a Perkin Elmer Spectrum One Spectrometer. TEM sample was prepared by drop-coating dispersion onto Cu grid coated with carbon. Images were acquired using a JEOL JEM 2100 transmission electron microscope, operating at a maximum accelerating voltage of 200 kV. FESEM images were obtained using Carl Zeiss SIGMA VP instrument. XRD data were acquired using a Bruker AXS D8 Advance X-ray diffractometer with $CuK\alpha_1$ radiation (λ~ 1.54060 Å), operated at 40 kV and 40 mA. Vibrating sample magnetometer (VSM) measurements were performed at 300 K in a VSM Lake Shore 736 controller. Thermogravimetric analysis (TGA) and differential scanning calorimetry (DSC) measurements were carried out with SDT Q600 TA instrument. Optical micrographs were acquired in a BX 51 Olympus Microscope equipped with a digital camera XC10.

The growth of NP supercrystals was carried out using a DC electromagnet (Model EMU-50V, Scientific Equipment & Services, Roorkee, India).

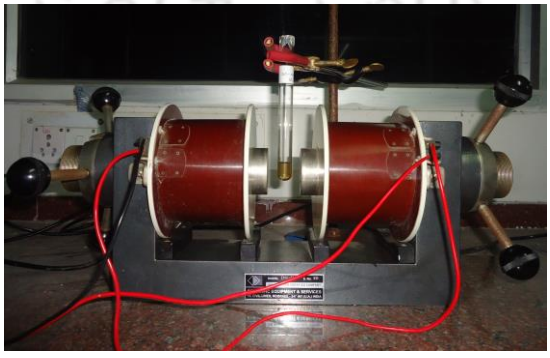

Figure 6.1. Photograph showing Fe_3O_4 NP dispersion (in $CHCl_3$) suspended between the poles of an electromagnet.

6.2. RESULTS AND DISCUSSION

Fe_3O_4 NPs were prepared, based on a reported protocol, [68] by the high temperature decomposition of $Fe(oleate)_3$ complex. The $Fe(oleate)_3$ complex was prepared by the reaction between $FeCl_3.6H_2O$ and Na-oleate. The formation of $Fe(oleate)_3$ complex was confirmed by FTIR spectroscopy and TGA and DSC measurements.

Fe_3O_4 NPs were synthesized *via* high temperature thermal decomposition of $Fe(oleate)_3$ complex in the presence of high boiling solvents – oleic acid and oleylamine. The as-synthesized NPs were isolated, from the oil phase, by precipitation with ethanol and purified further by repeated washing with hexane and ethanol, when excess oil was removed. The NPs were dispersed in chloroform. A dilute solution of same was used for investigation by TEM. TEM experiments revealed that the NPs were all spherical in shape and monodisperse in size, with an average diameter of 8 nm (Figure 6.2). The particles could be observed to have self-organized into a 2D superlattice with a uniform spacing in between, the reason for which could be attributed to the binding on the surface of NPs of long chain oleic acid moieties that prevented agglomeration among particles. It may be noted here that a successful synthesis of monodisperse NPs is the prerequisite of the generation of their supercrystals. The crystallinity of the particles was ascertained from the HRTEM analyses along with SAED studies. Both HRTEM and SAED results evidenced that the Fe_3O_4 crystals were single crystalline. IFFT image analysis of a particle observed at high resolution showed *d*-value of 0.29 nm (Figure 6.2c), which correspond to the spacing between the (220) planes of Fe_3O_4 crystals. The planes (111), (220), (311), (222), (400), (422), (511), (620) with *d*-values 0.46, 0.31, 0.27, 0.24, 0.22, 0.18, 0.16, 0.13 respectively had been identified in the SAED pattern (Figure 6.3a). These results were corroborated by powder XRD experiments (Figure 6.3b). The planes (220), (311), (400), (422), (511), (440) at Bragg's angles 30.1, 35.6, 43.8, 53.4, 56.9, 62.8° could be indexed.

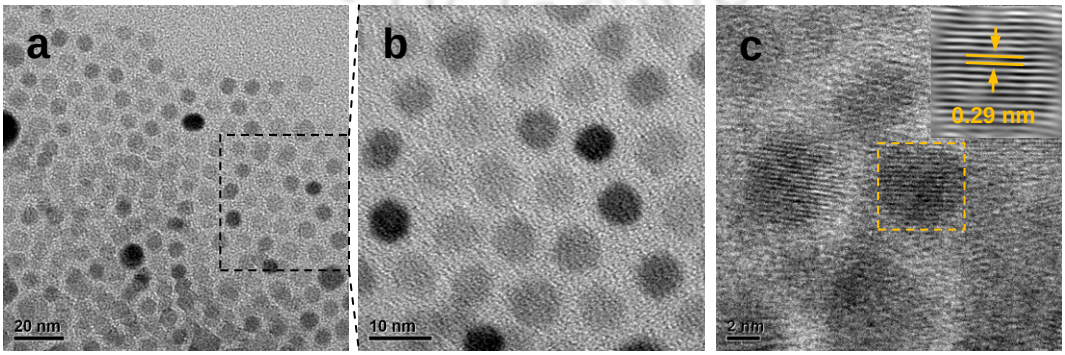

Figure 6.2. (a, b) Low and (c) high resolution TEM images of Fe_3O_4 NPs. Inset in (c) corresponds to IFFT image of the select particle.

The experimental findings suggested that the Fe_3O_4 NPs had body-centred cubic (*bcc*) spinel structure, coincident with the results in a standard reference (JCPDS Card No. 11-0614).

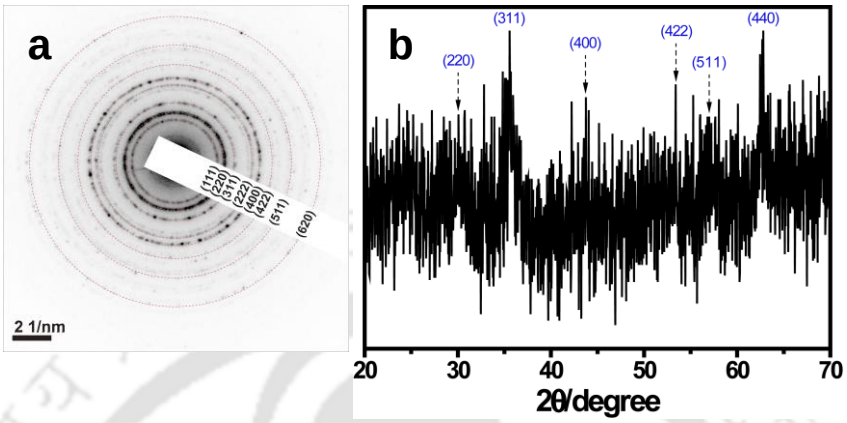

Figure 6.3. (a) SAED and (b) powder XRD patterns of Fe_3O_4 NPs.

The superparamagnetic behaviour of Fe_3O_4 NPs was ascertained from the M–H loop measured at 300 K (Figure 6.4) using a VSM. The saturation magnetization at 10 000 Oe is 48.5 emu.g^{-1}, which is much lower than that of bulk magnetite particles (92 emu.g^{-1}). The decrease in magnetization is due to the superparamagnetism of Fe_3O_4 NPs. [51, 361] The coercivity at room temperature is ~33 Oe, suggesting of the superparamagnetic nature of the particles and of their nano size. The coating of oleic acid onto the NPs was determined from the FTIR spectroscopic analyses. Figure 6.5a shows the spectra of oleic acid-coated Fe_3O_4 NPs and pristine oleic acid. The peak at 1638 cm^{-1} is due to C=O

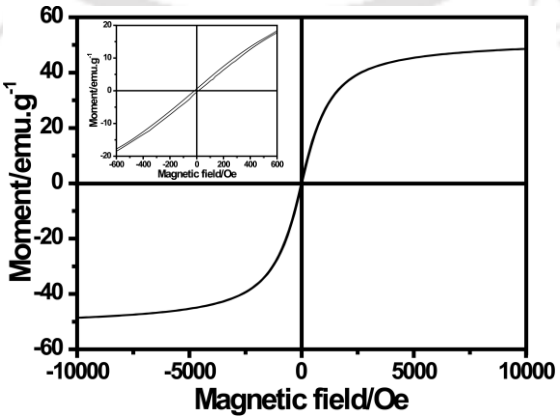

Figure 6.4. Hysteresis loop for Fe_3O_4 NPs with an expanded view (inset) of the region from -600 to +600 Oe and -20 to +20 emu.g^{-1}.

stretching frequency and which shifted to a lower energy with respect to the band for pure oleic acid (1712 cm^{-1}). The sharp bands at 2855 and 2926 cm^{-1} belong to the methylene and methyl symmetric stretching vibrations, respectively. Such bands in case of oleic acid bound to NPs occurred at 2853 and 2923 cm^{-1} respectively, showing no change in the vibrational frequencies of these bonds for oleic acid molecules anchored onto NPs, indicating thus that the above groups were not involved in grafting onto the NPs' surface. In the present set of experiments, for growing NP supercrystals (discussed in the subsequent paragraph), the NPs had to be initially treated with PEG. In order to check if PEG was present as a capping layer to the NPs or not, a weighed amount of PEG was added to oleic acid-stabilized Fe_3O_4 NPs and the solution was aged for 2–3 h. After this time, the solution was centrifuged and the precipitate containing Fe_3O_4 NPs was analysed *via* FTIR studies. The spectra of the NP precipitate and pure PEG resembled each other (Figure 6.5b), suggesting that PEG moieties were present along with NPs. The presence of weak peaks at 3430 and 2920 cm^{-1} for the O–H and C–H stretching vibrations in the PEG-contained NPs' spectrum (Figure 6.5b, i), vis-à-vis the spectrum for pure PEG (Figure 6.5b, ii), suggested the binding of PEG onto the NPs.

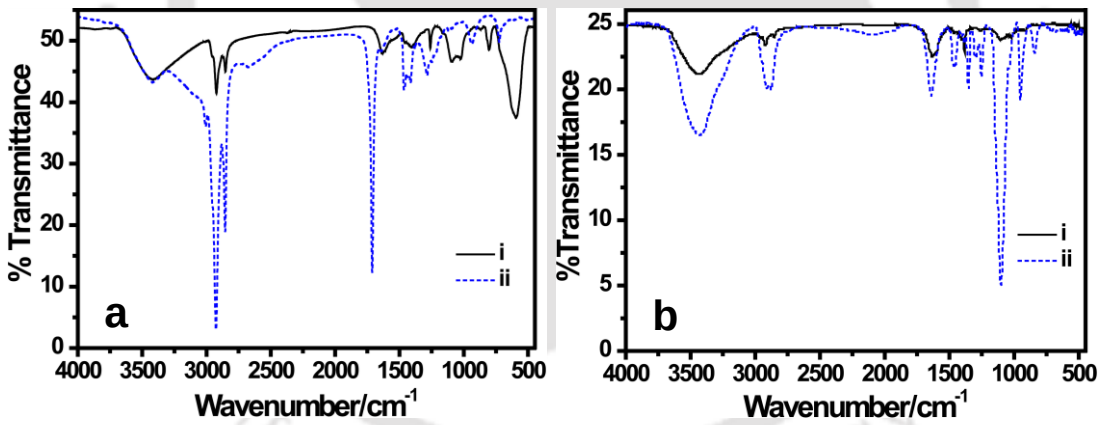

Figure 6.5. FTIR spectra of (a): (i) oleic acid-capped Fe_3O_4 NPs, and (ii) pure oleic acid, and (b): (i) PEG-coated Fe_3O_4 NPs, and (ii) pure PEG.

For generating Fe_3O_4 NP supercrystals, to a definite volume of oleic acid-stabilized Fe_3O_4 NP dispersion in chloroform (1 mL), a weighed amount of PEG (15 mg) was added and the resulting solution was placed under a magnetic field of 0.19 T (regulated using an electromagnet) and left undisturbed. After evaporation of chloroform from the medium, dark flaky crystals were obtained. For investigation in a TEM, the crystals were crushed and suspended in ethanol. A drop of the suspension was allowed to air-dry on a carbon-coated Cu grid. Ethanol was used as a solvent since both oleic acid-stabilized Fe_3O_4 NPs

and PEG are insoluble in it, and therefore, the sub-millimeter- and micrometer-sized crystallites (obtained on crushing the flaky crystals) remained intact for observation in a TEM. A TEM micrograph of a typical 3D supercrystal constituted of Fe_3O_4 NPs is shown in Figure 6.6a. The image also shows an extensive production of supercrystals with sizes of a few micrometers scattered over the entire region in the TEM grid. In addition, 2D superlattices of tens of nanometers in size could also be seen. A magnified view of the crystal in Figure 6.6a can be visualized in Figure 6.6b. Clearly, in Figure 6.6b, some regions appear light while others dark. The lighter regions are attributed to having lower density of NPs and therefore are thin. While the darker regions abound with NPs are relatively thicker. The particles were possibly held together by soft interactions, such as van der Waals or hydrogen bonding, between the coating molecules. [263] The visual difference in contrast, arising out of differential NP densities, is more apparent from Figure 6.6c.

It is, however, cumbersome to estimate deterministically the nature of packing of NPs in such crystals. The roughness is vivid when individual NPs are compared with their neighbouring ones. However, examining a TEM image of a crystal at an optimum resolution enabled figuring out regions having packing in the form of hexagonal closed-pack (*hcp*). A magnified image (Figure 6.6d) of a section of crystal in Figure 6.6c can be considered for determining the nature of packing of NPs. In the figure, the *hcp* is indicated by a circle and a concentric hexagon. The circle implies the central particle, while the vertices of the hexagon denote the surrounding particles. As apparent from the TEM and FESEM images, the surfaces of crystals consist of NPs present randomly providing an uneven topography. Therefore, translation of the *hcp* packing could possibly not be materialized at the surfaces. A model [362] of the packing of NPs *via hcp*-stacked layers forming a 3D supercrystal is proposed (Figure 6.6e). The SAED pattern obtained from a region of densely packed NPs appeared to show concentric ring patterns (Figure 6.6f). This was attributable to diffractions from a collection of NPs. More TEM images of the supercrystals grown in the presence of 0.19 T field can be found in Figure 6.7. The crystals are all elongated in shape and have length of a couple of micrometers.

Understanding of the surface morphology of crystals, however, could not be made from TEM experiments. The surface profile is evident from field-emission scanning electron microscopy (FESEM) experiments (Figure 6.8). The crystals appear flat and smooth at the resolution provided by the FESEM electron beam. However, defects as steps and ridges are also evident from the images.

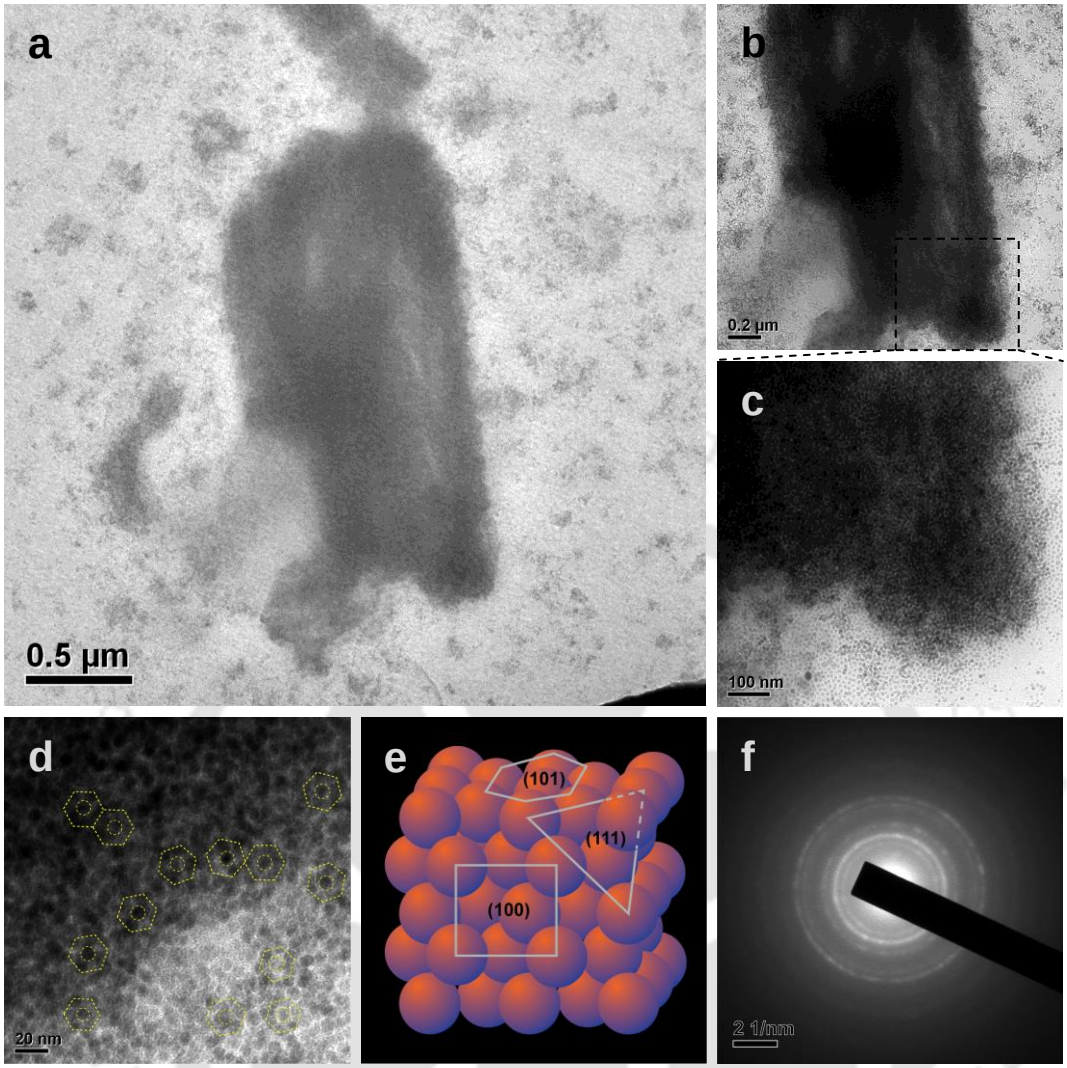

Figure 6.6. (a) Large area TEM image of a supercrystal of Fe_3O_4 NPs grown under a magnetic field of 0.19 T. (b) Higher resolution image of a part of the crystal in (a), and (c) is the higher resolution image of the select region in (b). (d) is the close up of a dense region in (c), and (e) is the model packing of NPs (in a supercrystal) shown in (d). (f) SAED patterns obtained from a dense region in (d).

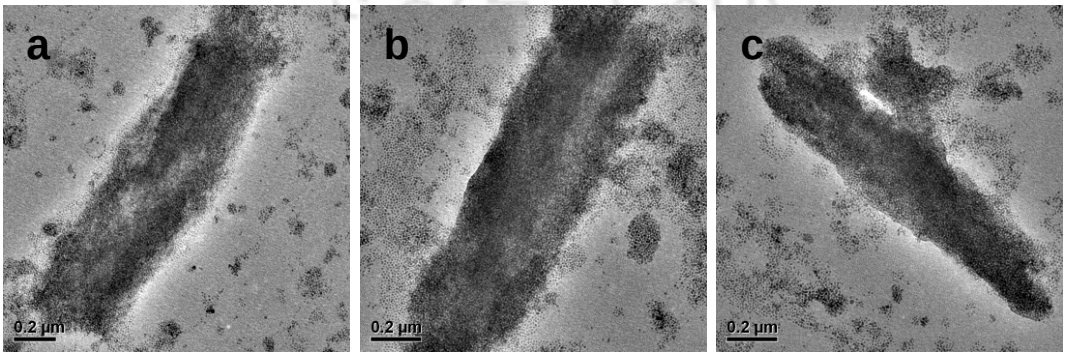

Figure 6.7. (a–c) Low resolution TEM images of Fe_3O_4 NP supercrystals that were grown in the presence of 0.19 T magnetic field.

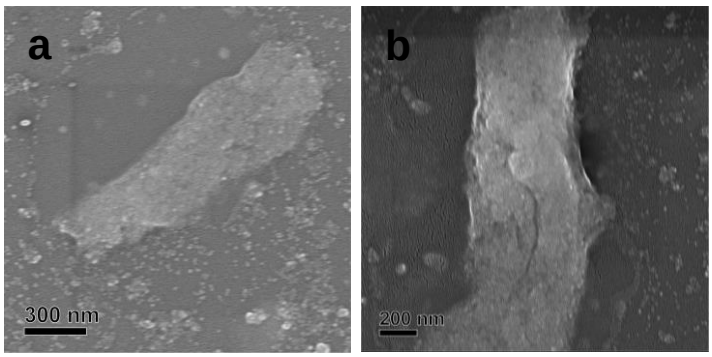

Figure 6.8. (a, b) FESEM images of Fe_3O_4 NP supercrystals grown in the presence of 0.19 T field.

In order to gain insight on the growth habit of supercrystals in the presence of magnetic field, a 1 mL solution was suspended to a magnetic field of 0.19 T, and the solution examined under TEM at different time intervals; the TEM results can be found in Figure 6.9. At time 0 h particles were present as free isolated forms as well as in the form of small assortments (Figure 6.9a). The smaller aggregates could have formed in the process of TEM sample drying. After 12 h, larger aggregates of NPs could be observed and the density of such structures was large (Figure 6.9b). It is interesting to observe the

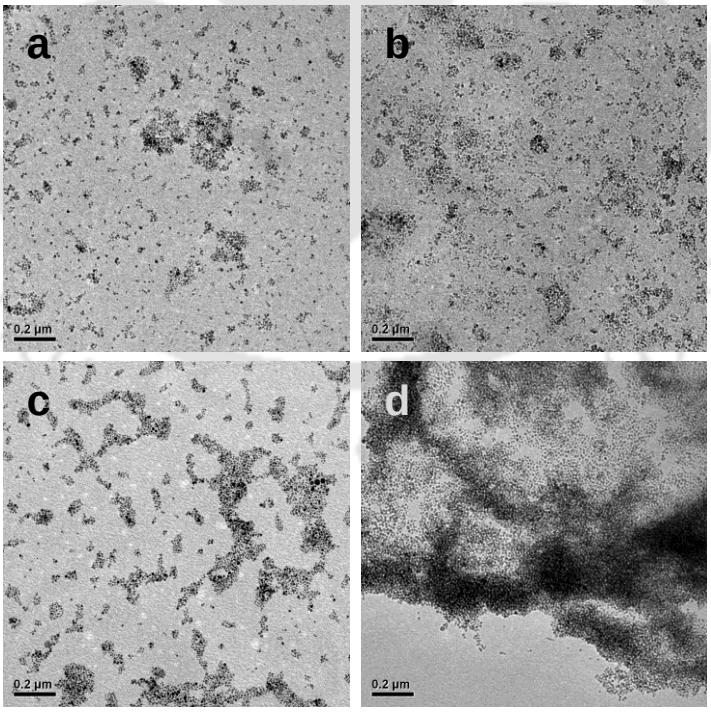

Figure 6.9. Low resolution TEM images, recorded at times (a) 0 h, (b) 12 h, (c) 18 h and (d) 24 h, of the dispersion of Fe_3O_4 NPs with PEG in chloroform, suspended to a magnetic field of 0.19 T.

sample after 18 h when the solution volume had reduced considerably. The TEM showed

formation of smaller crystals of sub-micrometer in size and less. They were elongated structures having NPs organized mostly in 2D (Figure 6.9c). Such structures could have been the result of alignment of particles along the magnetic field. In addition, it could be observed that there were no isolated free NPs compared to samples observed at times 0 and 12 h, signifying the reduction in the density of isolated particles and their participation in the formation of crystals. The results suggested that the formation of crystals had resulted in the bulk solution much before evaporation of solvent. After 24 h when solid visible crystals formed, with the complete evaporation of chloroform, the crystals were larger with particles aggregated in 3D (Figure 6.9d). The formation of NP assembly leading to crystals is considered to be entropy-driven. [363] The evaporation of solvent from the medium is responsible for increasing the entropy. An important condition for the formation of ordered structures of particles in the crystals probably is that the evaporation of the liquid has to be slow enough to allow for diffusion during the process of solidification. It might be that under the influence of magnetic field chains of NPs initially formed in the solution, followed by clustering to form 2D sheets (Figure 6.9b, c) and eventually leading to the formation of 3D crystals (Figure 6.6a, Figure 6.7). It is also interesting to make comparative studies of the crystals, being generated under different field strengths, with each other and also with the crystals formed in the absence of external field. For instance, formation of crystals in the absence of field was accompanied with substantial spacing between particles (Figure 6.10a). However, the spacing reduced for crystals grown in a field to 0.09 T (Figure 6.10b). The spacing was further less in the crystals grown at 0.15 T (Figure 6.10c). In addition, formation of larger aggregates was found to be favored with the increase in the field strength. Finally, in the case of crystals generated at 0.19 T field, larger aggregation of NPs occurred, with spacing between particles not clearly discernible (Figure 6.10d). It is also apparent from Figure 6.10d that the packing of particles formed in the presence of stronger magnetic field was tight and the crystals possessed definite geometries compared to those that formed under weaker or no field. In fact on comparison of the brittleness, it was found that the crystals formed under stronger field were considerably harder than that formed in the absence of or weaker field.

Powder XRD analyses of the supercrystals give the impression of the presence of Fe_3O_4 NPs along with PEG (Figure 6.11). The diffractions due to PEG being overwhelming peaks due to NPs were not quite prominent. The results indicated the higher content of PEG in the crystals. Diffraction lines corresponding to planes (311), (400), (422), (440) of Fe_3O_4 NPs could be assigned at the angles 35.4, 43.4, 53.3, 62.2°. It may be added here that the presence of higher proportion of PEG in the supercrystals was responsible for the

occurrence of blurry circles in the SAED pattern (Figure 6.6f), and otherwise not observing sharp spots due to Fe_3O_4 NPs.

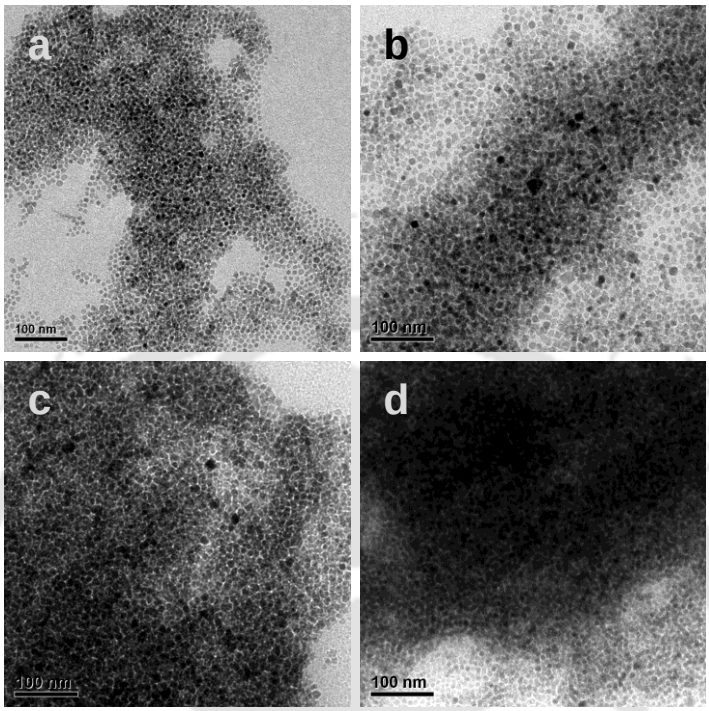

Figure 6.10. TEM images of Fe_3O_4 NP supercrystals grown in the (a) absence (0 T), and presence of (b) 0.09, (c) 0.15 and (d) 0.19 T magnetic fields.

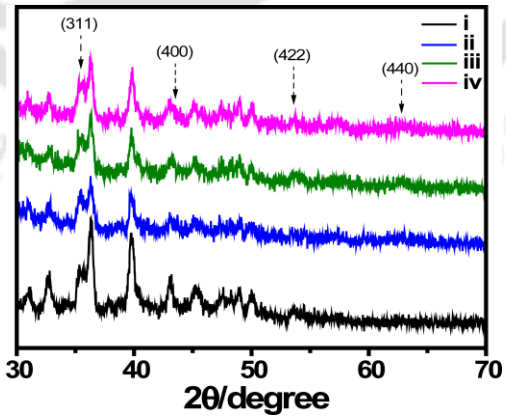

Figure 6.11. Powder XRD patterns of crushed (i) PEG crystals, and Fe_3O_4 NP supercrystals grown under (ii) 0, (iii) 0.09, and (iv) 0.19 T magnetic fields. Planes indicated with arrows are for Fe_3O_4 NPs.

The magnetic properties of the crystals were determined from the VSM measurements. The crystals prepared in the absence of magnetic field and in the presence of 0.09 and 0.19 T fields were compared. The response of the supercrystals (in their ground form) in a magnetic field at 300 K was found to be apparently identical (Figure 6.12). The saturation magnetization for the crystals prepared in the absence of field and in the presence of 0.19 T field was significantly low, values for both being 0.59 emu.g^{-1}. And it was 0.50 emu.g^{-1} for the crystals prepared under 0.09 T field. The coercivity of the samples were 36.5, 63.4, 98.4 Oe, as clear from Figure 6.12b. The reduction in the saturation magnetization could be attributed to the presence of PEG moieties on the surfaces of Fe_3O_4 NPs. Some studies suggest that non-collinear spin structure, which originates from the pinning of the surface spins and coating of surfactant at the interface of Fe_3O_4 NPs, is responsible for the reduction of magnetic moments in such NPs. [364] The same may be the cause for the current observation.

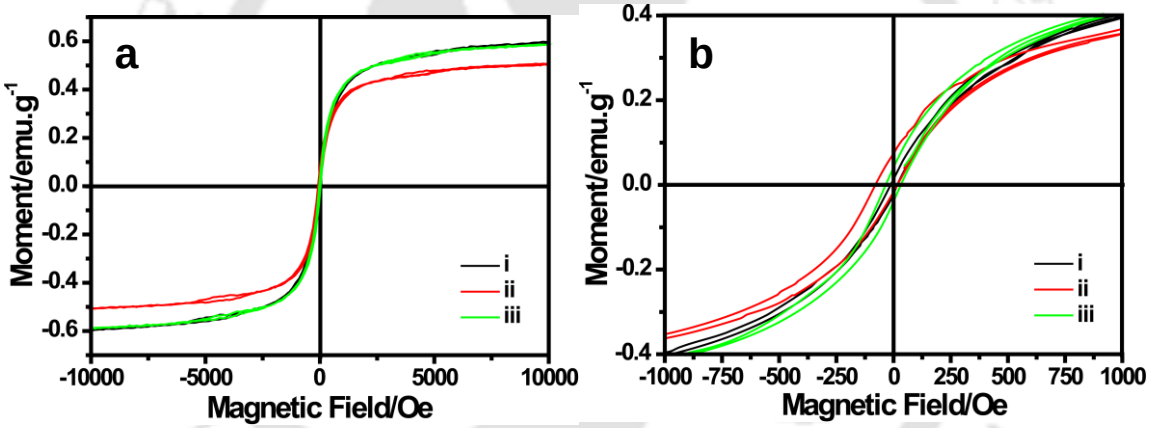

Figure 6.12. (a) Hysteresis loops for Fe_3O_4 NP supercrystals grown in the (i) absence of magnetic field, and presence of (ii) 0.09 and (iii) 0.19 T fields. (b) Expanded view of (a) from -1000 to +1000 Oe and -0.4 to +0.4 emu.g^{-1}.

There was also visible difference in the crystals formed under the presence of field from that of the crystals formed in the absence of field. The optical microscopy images of the crystals generated under 0.19 T field and in the absence of field are given in Figure 6.13. The former crystals appeared dark yellowish to brownish, while the latter ones were canary yellow. The apparent difference in colour of the crystals could be due to difference in the packing of NPs (as mentioned above) in the two types of crystals and vice versa, where both the crystals were made starting from the same initial concentration of NPs.

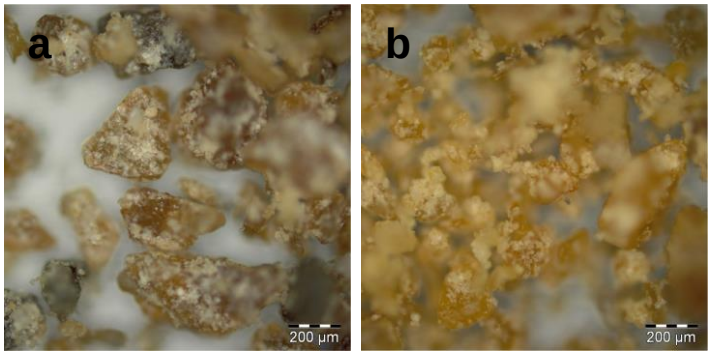

Figure 6.13. Optical micrographs of Fe_3O_4 NP supercrystals grown in the (a) presence (0.19 T), and (b) absence of magnetic field.

Further, it was interesting to explore the supercrystals made using Fe_3O_4@Au core–shell NPs as building blocks. The reason for using Fe_3O_4@Au NPs was to have dual properties – superparamagnetism due to Fe_3O_4 core, and optical property as a result of the Au shell. The synthesis of Fe_3O_4@Au NPs involved the coating of Fe_3O_4 NPs with Au. [68] For this, an Fe_3O_4 NP dispersion in chloroform was treated with $HAuCl_4$ in the presence of oleylamine. Oleylamine served as a reducing as well as a capping agent for the NPs. The reaction was allowed to continue for 20 h. After this time, the colour of the solution appeared to be reddish, suggesting the formation of Au NPs in the medium. Following washings of the solution, by means of centrifugal precipitation, the particles were redispersed in chloroform. UV/Vis spectra of this solution and of Fe_3O_4 NP dispersion in chloroform (that was used for the synthesis of Fe_3O_4@Au NPs) were recorded and the results are shown in Figure 6.14. An extinction band at 524 nm (Figure 6.14, ii) is due to the SPR of nano-sized Au. [346] Such band was, however, not observed in the case of Fe_3O_4 NP dispersion only (Figure 6.14, i). This confirmed that the reddish solution (mentioned above) contained Au NPs, in addition to Fe_3O_4 NPs. The TEM experiments served emphatically as an evidence of the formation of core–shell Fe_3O_4@Au NPs. A TEM micrograph, of the sample mentioned (ii) in Figure 6.15, does not give a clear impression of the core–shell morphology of particles at low resolution (Figure 6.15a), however, at higher resolution (Figure 6.15b) the shell surrounding the core particles was clearly discernible. The dark central region of each particle was due to the Fe_3O_4 NP core, while the outer lighter region was for the Au shell. An IFFT image derived from a region of one such particle showed the presence of (hkl) planes due to both Au and Fe_3O_4 crystals. The *d*-values (marked in Figure 6.15b) corresponded to (111) planes of an Au lattice (d = 0.23 nm), and to (400) planes from Fe_3O_4 (d = 0.20 nm). In addition, powder XRD

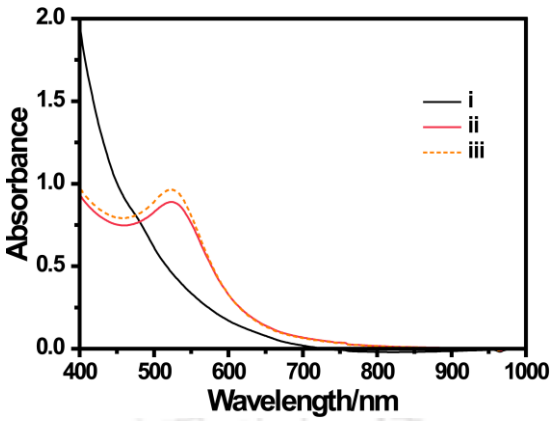

Figure 6.14. UV/Vis spectra of dispersions of (i) Fe_3O_4 NPs, (ii) Fe_3O_4@Au NPs, and (iii) Fe_3O_4@Au NPs mixed PEG.

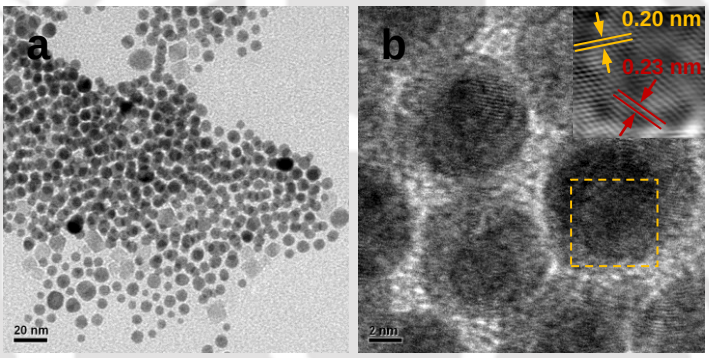

Figure 6.15. (a) Low and (b) high resolution TEM images of Fe_3O_4@Au NPs. Inset in (b) is the IFFT image of the select region of a core–shell particle.

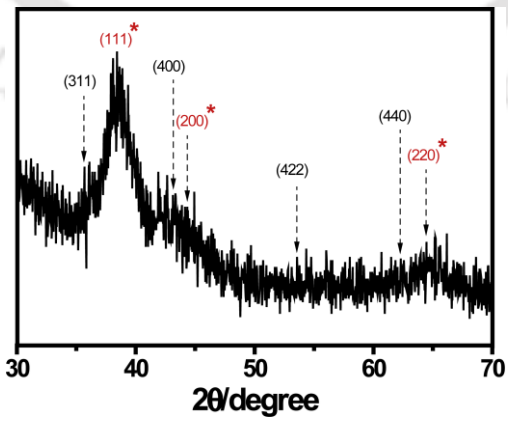

Figure 6.16. Powder XRD patterns of Fe_3O_4@Au NPs. Diffractions due to planes belonging to Fe_3O_4 and Au crystals are indicated; those shown with asterisks are for Au.

pattern of the NPs (Figure 6.16) showed diffraction peaks at 2θ values 38.4, 44.3, 64.5° corresponding to (111), (200), (220) planes of an *fcc* lattice of Au. Diffractions due to Fe_3O_4 NP crystals could also be identified, the planes viz., (311), (400), (422), (440) occurring at the angles 35.7, 43.1, 53.6, 62.3° were relevant.

Following synthesis of Fe_3O_4@Au NPs, the subsequent step consisted of subjecting a PEG containing dispersion of Fe_3O_4@Au NP to a magnetic field, similar to the procedure followed for growing Fe_3O_4 NP supercrystals. The dispersion of such a mixture of NPs and PEG in chloroform showed an SPR band due to Au nanoshell at 523 nm (Figure 6.14, iii), signifying no change of particles in the medium with respect to the as-made solution. Crystals had been grown in the presence of 0.19 T field and they were compared with those grown in the absence of field. The as-grown crystals of both types were maroon-coloured in appearance. The reflectance mode UV/Vis spectra of the crushed crystals, grown in the presence and absence of magnetic fields, exhibited plasmon band at around 531 nm (Figure 6.17a, i and ii). A redshift of this band (by ~8 nm), with respect to the spectrum of the initial solution (Figure 6.14, iii) from which the crystals were grown, indicated modest clustering of NPs in the crystals. There was also a reduction in the peak intensity of the band for the crystals grown in the presence of field than that for the crystals grown as such. An obvious reason for this difference was that the NPs subjected under the influence of magnetic field underwent higher degree of agglomeration. Therefore, free isolated NPs would be barely available in the crystals and consequentially the longitudinal oscillation of NP aggregates would overwhelm the transverse oscillation, thereby resulting in the broadness of band in the optical resonance of NP supercrystals. As a matter of fact, broadness of band could also be seen in the case of crystals grown in the absence of field, although the peak intensity was higher than the band for the crystals grown in the presence of field. The line broadening of both the curves in Figure 6.17a was interpreted by deconvoluting the curves using Lorentzian peak-fitting function available as an in-built program in the Origin Software (version 7.0, being used here). On deconvolution of the curves (i and ii, in Figure 6.17a), each spectrum was reduced to three component spectra (dotted lines in Figures 6.17b, c), where the curves in red and purple signify bands due to transverse and longitudinal oscillations of NPs respectively, and the blue curves due to scattering of light. The showing up of longitudinal band affirmed the presence of NPs in the crystals in their agglomerated forms, thus explaining the cause for the broadness of the spectra in Figure 6.17a. However, quantitative distinction of the two types of crystals could not be made based on the deconvolution curve fitting analyses.

On re-dissolution of the crystals back in chloroform, dual bands – transverse and longitudinal – appeared in the spectra of both the types of crystals (Figure 6.17d, i and ii).

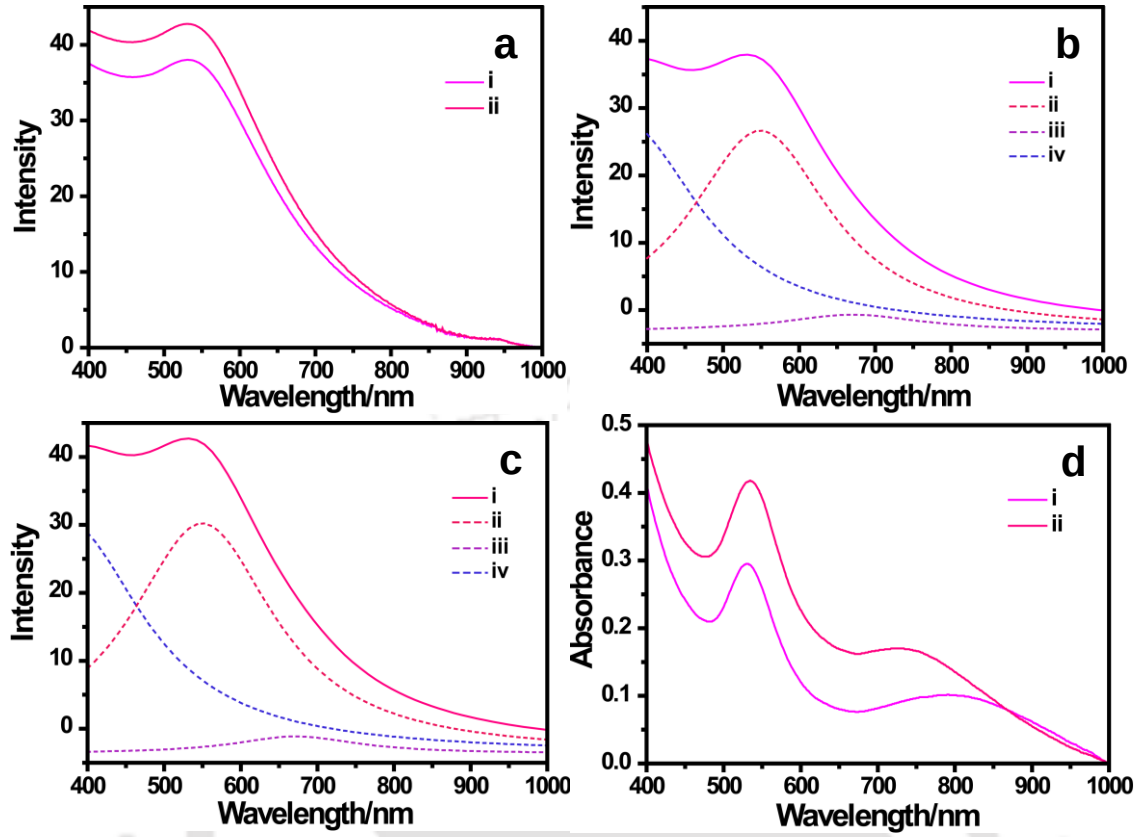

Figure 6.17. (a) UV/Vis spectra (recorded in the reflectance) of crushed Fe_3O_4@Au NP supercrystals generated (i) under 0.19 T field, and (ii) in the absence of external field. (b) and (c) Spectra (solid lines) referred as (i) and (ii) in (a) with their corresponding deconvoluted curves (dotted lines). (d) UV/Vis spectra of the re-dissolved crystals generated (i) under 0.19 T field, and (ii) in the absence of external field.

While the position of the transverse band was at around 532 nm, the longitudinal bands appeared at 790 and 726 nm respectively for the solutions of crystals made in the presence and absence of external fields. The appearance of long wavelength band suggested the presence of clusters of NPs in solution that did not break up even on dissolution of the crystals. Further, for the crystals made in the presence of magnetic field, the longitudinal band existed far to the red side (by ca. 60 nm) compared to the crystals prepared in the absence of field, in addition to the occurrence of its transverse and longitudinal bands at lower intensities. Such an observation could be interpreted as due to a pronounced packing of NPs, in the crystals grown under the magnetic field, leading to an effective coupling between the plasmons of neighboring NPs. The NP supercrystals could, thus, prove to be ideal for applications in waveguides working from the visible to the near-infrared (NIR) region of the electromagnetic spectrum. [277, 308, 310]

TEM observation of the crystals grown in the presence of 0.19 T field was particularly interesting. While the supercrystals of Fe_3O_4 NPs were elongated in shapes, those of Fe_3O_4@Au NPs were spherical and appeared as honey-comb like structures (Figure 6.18). One of the reasons for the occurrence of structures in such geometries could be due to weaker magnetic response of the core–shell NPs, owing to coating of Fe_3O_4 NPs with Au, than Fe_3O_4 NPs only. The packing of particles was seemingly identical to the crystals constituted of Fe_3O_4 NPs only (Figure 6.6d). The presence of particles in close vicinity to each other in the crystals was responsible for the broadness of the band in the UV/Vis

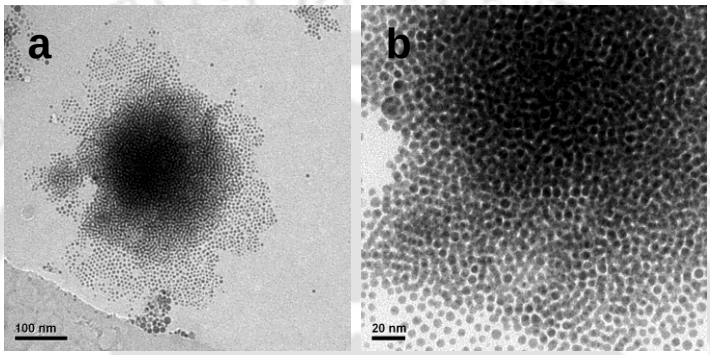

Figure 6.18. (a, b) TEM images of Fe_3O_4@Au NP supercrystals grown in the presence of 0.19 T magnetic field.

spectrum (Figure 6.17a, i). Also, it was for the tight packing of particles that the crystals on re-dissolution did not help segregate them and therefore led to the appearance of longer wavelength band in the UV/Vis spectrum (Figure 6.17d, i).

Electron diffraction from a dense region of a crystal showed sharp ring patterns (Figure 6.19a). Again, as has been explained in the case of supercrystals of Fe_3O_4, the presence of larger content of PEG would have diminished the visibility of diffractions arising from the crystals of Au and Fe_3O_4, although diffractions from both the materials had resulted, as explained in the text that follows. Powder XRD studies of the crystals of the two types (grown in the absence and presence of fields) showed the diffractions due to Fe_3O_4 and Au crystals (as has been discussed above for the Fe_3O_4@Au NPs), in addition to diffractions from PEG crystals (Figure 6.19b).

The crystals showed magnetic properties, as determined from VSM measurements. The results are shown in Figure 6.20. The saturation magnetization of Fe_3O_4@Au NPs was relatively low (Figure 6.20, i), which was indicative of the weak magnetic behaviour of the core–shell particles, cause being the surface coating of Fe_3O_4 NPs with Au. On formation of crystals further reduction in their magnetic property occurred (Figure 6.20, ii, iii), like

the supercrystals of bare Fe_3O_4 NPs.

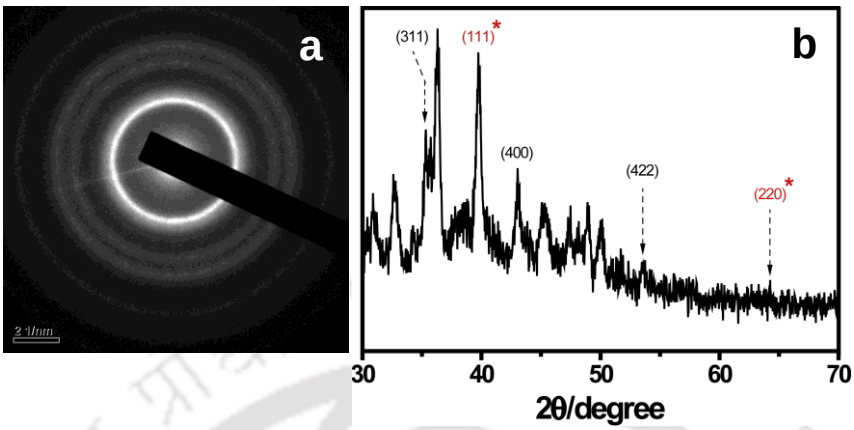

Figure 6.19. (a) SAED and (b) powder XRD patterns of Fe_3O_4@Au NP supercrystals grown in the presence of 0.19 T magnetic field. The planes indicated with asterisks in (b) are for *fcc* Au NP.

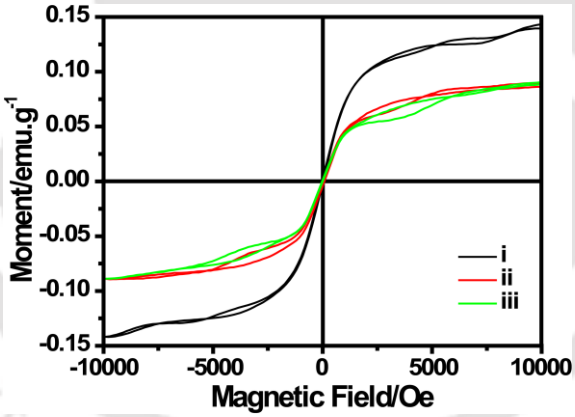

Figure 6.20. Hysteresis loops for (i) Fe_3O_4@Au NPs, and Fe_3O_4@Au NP supercrystals grown in the (ii) absence and (iii) presence (0.19 T) of magnetic field.

Further, observation of crushed samples of the crystals in a microscope showed purple colour of the crystals (Figure 6.21). The colour was indistinguishable for the crystals grown in the presence and absence of magnetic fields. The observed colour was characteristic of Au NPs present in agglomerated forms in the crystals (as observed in Chapter 5), which was consistent with the UV/Vis and TEM experiments.

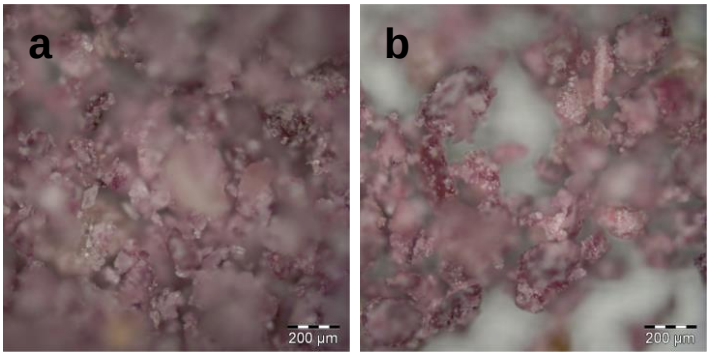

Figure 6.21. Optical micrographs of Fe_3O_4@Au NP supercrystals grown in the (a) presence (0.19 T), and (b) absence of magnetic field.

6.3. CONCLUSIONS

The work consisted of generation of supercrystals of magnetic NPs, such as Fe_3O_4 and Fe_3O_4@Au, in 2D and 3D. The crystals of the former NPs were magnetic, whereas that of the latter were magnetic as well as supported plasmon resonance (as a result of Au shell). Interestingly, in the case of supercrystals of Fe_3O_4@Au, longitudinal plasmon resonance occurred far to the NIR region of the electromagnetic spectrum. On observation in an optical microscope, the crystals of Fe_3O_4 NPs appeared dark yellowish to brownish colour while that of Fe_3O_4@Au NPs were purplish. The crystals could be deemed to be potentially useful in the data storage (owing to their magnetic properties) and waveguide (optical property) applications, apart from contemplating of their use in sensing and catalysis [365].

Chapter 7

Thesis Overview and Future Outlook

7.1. OVERVIEW OF THE THESIS

This thesis has touched on the syntheses of zero-dimensional (0D) nanoparticles (NPs) – based on inorganic–organic hybrid crystals – on one hand, and generation of higher order architectures (1D, 2D, 3D) using such NPs as building blocks, on the other. More specifically, NPs of metals, oxides of metals, and organic molecules were of interest. Toward 0D NPs, generation of core–shell crystalline NPs was of main focus. For instance, core–shell NPs have been generated by having metal NP as core and an organic crystal as shell. This is discussed in Chapter 2, where the synthesis of Ag@pHA NPs and their detailed characterization have been demonstrated. Also, core–shell NPs having composition that is structurally reverse to the NPs mentioned in Chapter 2 is described in Chapter 3, viz., the generation of pHA@Au NPs. Further, the release of the organic core (pHA moieties) following etching of the Au shell has been worked out.

Chapters 4 till 6 discuss on the generation of higher order superstructures of NPs and study of the possible properties of such structures. Chemical and physical means have been of relevance in generating the structures. For example, Chapter 4 describes the formation of 1D linear assembly of Au NPs by treatment of citrate-stabilized Au NPs with protonated-pAA moieties. The formation of assembly was marked by the appearance of LSPR band in the UV/Vis spectrum. Interestingly, the LSPR band could be tuned by two parameters, such as, concentration of pAA molecules and using NPs of different sizes in the initial solution. With an aim to use similar NP-molecule interaction as strategy, it has been attempted to construct 3D crystals of Au NPs by treatment of the NPs with pHA molecules. The work is described in Chapter 5. The reason for using pHA molecules is that it can easily be crystallized and, in addition, it can bind with metal NPs through its –$NHCOCH_3$ group. The outcome of the work was the formation of 3D composite crystals consisting of pHA crystals in which Au NPs were embedded. The Au NPs were present in isolated and agglomerated forms in the crystals. The optical property of the crystals arose due to the plasmonic signatures of Au NPs; the crystallinity of pHA could be tuned by varying the ratio of concentrations of Au NPs to pHA. The color of the crystals was indicative of the nature (isolated or agglomerated form) in which Au NPs were present in

the crystals. However, periodicity due to Au NPs was not observed in the crystals.

Simple solution based synthetic strategy, as described above, was not fruitful for constructing organized 2D and 3D architectures of NPs. Therefore, attention was directed to the use of physical means, such as, magnetic field for assembling NPs with superparamagnetic properties. PEG stabilized-magnetite (Fe_3O_4) NPs were used in this regard. They could be organized in the forms of 2D and 3D supercrystals by suspending their solution under the influence of an external magnetic field, as has been described in Chapter 6. The crystals of core–shell Fe_3O_4@Au NPs have also been generated. The supercrystals of both the NPs (Fe_3O_4 and Fe_3O_4@Au) were magnetic in nature. Fe_3O_4@Au NP supercrystals, in addition, showed optical properties.

It may be noted that, in all the works described above, the discussion centered around the context of inorganic–organic hybrid, which is the very theme of the thesis.

7.2. FUTURE OUTLOOK

Research on NP self-assembly is developing at a rapid pace in several directions to bring forth exquisite structures with brand new properties. What is more significant is to pay interest on the generation of robust multifunctional structures. In order to explore new properties and applications of 1D NP assemblies, it is important to pay particular attention to their methods of preparation. The properties of 1D assemblies depend much on the interparticle distance, so as to realize their applications in electronic and photonic devices, telecommunications, and sensors. [185] Again, chains of NPs containing multiple components exhibit superior application potentials. For instance, chains of metal and semiconductor NPs can find use as prototypes of Schottky diodes, while that of metal and magnetic NPs are useful as spintronic devices. [185] Furthermore, nature provides classic examples of remarkably complex, and yet highly organized self-assembled hierarchical structures. It is possible to have control over the types of NP assemblies in the laboratory and to improve their qualities, if some of the forms of self-assembly found in nature is, at least, partially followed.

It is appropriate to work out the design rules that would pave the way for the generation of complex hierarchical structures, by exploiting the analogy of NPs with atoms and molecules. First step towards this is the robust and highly reproducible synthesis of NPs, with close to 100% yield, along with well-defined sizes, shapes, aspect ratios and chemical heterogeneity. Fractionation of NPs following their synthesis is ideal for enhancing their properties and self-assembly.

It is also equally important to understand the roles of thermal fluctuations and kinetic factors in the formation of certain structures. [366] In addition, simulation studies

relating to self-assembly formation with particular emphasis on thermodynamic parameters and architectural features are to be considered in order to predict new structures, and guide the formation of existing nanostructures. [367, 368]

Again, hybrid inorganic–organic materials are essential in the development of advanced functional nanostructures. Research in the areas of functional hybrid inorganic–organic materials is fostered by the growing interest of chemists, physicists, biologists and materials scientists. The primary aim being is to create smart materials that benefit from the best of the three realms: inorganic, organic and biological. Today, the application potentials of hybrid materials are becoming a reality. Many hybrid materials are entering niche markets, and this is going to expand in the future. While the design of new functional hybrid materials with enhanced properties is appealing, it is important to also bear in mind that a harmony between the environment and human activities is highly desirable. As researchers, we must respect the environment and resort more into recyclability and reliability.

Bibliography

[1] Kreibig, U.; Vollmer, M. *Optical Properties of Metal Clusters*; Springer: Berlin, 1995.

[2] Schmid, G. *Clusters and Colloids – From Theory to Applications*; VCH: Weinheim, Germany, 1994.

[3] Ghosh, S. K.; Kundu, S.; Mandal, M.; Pal, T. *Langmuir* **2002**, *18*, 8756–8760.

[4] Ghosh, S. K.; Pal, T.; Kundu, S.; Nath, S.; Pal, T. *Chem. Phys. Lett.* **2004**, *395*, 366–372.

[5] Ghosh, S. K.; Pal, A.; Kundu, S.; Nath, S.; Panigrahi, S.; Pal, T. *Chem. Phys. Lett.* **2005**, *412*, 5–11.

[6] Kubo, R. *J. Phys. Soc. Jpn.* **1962**, *17*, 975–986.

[7] Jackson, J. D. *Classical Electrodynamics*; Wiley: New York, 1975; p 98.

[8] Efrima, S.; Metiu, H. *J. Chem. Phys.* **1979**, *70*, 1602–1613.

[9] Aravind, P. K.; Metiu, H. *Chem. Phys. Lett.* **1980**, *74*, 301–305.

[10] Gersten, J. I.; Nitzan, A. *J. Chem. Phys.* **1980**, *73*, 3023–3037.

[11] Wang, D.-S.; Chew, H.; Kerker, M. *Appl. Opt.* **1980**, *19*, 2256–2257.

[12] Mirkin, C. A.; Ratner, M. A. *Annu. Rev. Phys. Chem.* **1992**, *43*, 719–754.

[13] Rampi, M. A.; Schueller, O. J. A.; Whitesides, G. M. *Appl. Phys. Lett.* **1998**, *72*, 1781–1783.

[14] Atwater, H. A. *Sci. Am.* **2007**, *296*, 56–63.

[15] Compton, D.; Comish, L.; van der Lingen, E. *Gold Bull.* **2003**, *36*, 10–16.

[16] Leonhardt, U. *Nat. Photon.* **2007**, *1*, 207–208.

[17] Faraday, M. *Philos. Trans. R. Soc. London, Ser. A* **1857**, *147*, 145–181.

[18] Mie, G. *Ann. Phys.* **1908**, *25*, 377–445.

[19] Kerker, M. *The Scattering of Light and other Electromagnetic Radiation*; Academic Press: New York, 1969.

[20] Lazarides, A. A.; Kelly, K.; Schatz, G. C. *Proceedings of the Materials Research Society Meeting*; Boston, 2001; p 635.

[21] Rayleigh, J. W. S. *Proc. R. Soc. London, Ser. A* **1907**, *79*, 399–416.

[22] Rayleigh, J. W. S. *Philos. Mag.* **1907**, *14*, 60–65.

[23] (a) Landau, L. M.; Lifshitz, E. M. *Electrodynamics of Continuous Media*; Pergamon: Oxford, 1971. (b) Jackson, J. D. *Classical Electrodynamics*; Wiley: New York, 1975.

[24] Turkevich, J.; Stevenson, P. C.; Hillier, J. *Discuss. Faraday Soc.* **1951**, *11*, 55–75.

[25] Enüstün, B. V.; Turkevich, J. *J. Am. Chem. Soc.* **1963**, *85*, 3317–3328.

[26] Frens, G. *Nat. Phys. Sci.* **1973**, *241*, 20–22.

[27] Giersig, M.; Mulvaney, P. *Langmuir* **1993**, *9*, 3408–3413.

[28] Brust, M.; Walker, M.; Bethell, D.; Schiffrin, D. J.; Whyman, R. J. *Chem. Soc., Chem. Commun.* **1994**, 801–802.

[29] Alvarez, M. M.; Khoury, J. T.; Schaaff, T. G.; Shafigullin, M. N.; Vezmar, I.; Whetten, R. L. *J. Phys. Chem. B* **1997**, *101*, 3706–3712.

[30] Lyon, L. A.; Pena, D. J.; Natan, M. J. *J. Phys. Chem. B* **1999**, *103*, 5826–5831.

Bibliography

[31] Link, S.; El-Sayed, M. A. *J. Phys. Chem. B* **1999**, *103*, 8410–8426.

[32] Jain, P. K.; Huang, X.; El-Sayed, I. H.; El-Sayed, M. A. *Acc. Chem. Res.* **2008**, *41*, 1578–1586.

[33] Urbanska, K.; Romanowska-Dixon, B.; Matuszak, Z.; Oszajca, J.; Nowak-Sliwinska, P.; Stochel, G. *Acta Biochim. Pol.* **2002**, *43*, 387–391.

[34] Du, H.; Fuh, R. A.; Li, J.; Corkan, A.; Lindsey, J. S. *Photochem. Photobiol.* **1998**, *68*, 141–142.

[35] Murphy, C. J.; Sau, T. K.; Gole, A. M.; Orendorff, C. J.; Gao, J.; Gou, L.; Hunyadi, S. E.; Li, T. *J. Phys. Chem. B* **2005**, *109*, 13857–13870.

[36] Link, S.; Mohamed, M. B.; El-Sayed, M. A. *J. Phys. Chem. B* **2005**, *109*, 10531–10532.

[37] Schwartzberg, A. M.; Zhang, J. Z. *J. Phys. Chem. C* **2008**, *112*, 10323–10337.

[38] Weissleder, R. *Nat. Biotechnol.* 2001, 19, 316–317.

[39] Weiser, H. B. *Inorganic Colloid Chemistry*; Wiley: New York, 1933; Vol. 1.

[40] Searle, A. B. *The Use of Colloids in Health and Disease*; E.P. Dutton: New York, 1919.

[41] Wiley, B.; Sun, Y.; Xia, Y. *Acc. Chem. Res.* **2007**, *40*, 1067–1076.

[42] Ru, E. L.; Etchegoin, P. *Principles of Surface Enhanced Raman Spectroscopy*; Elsevier: Oxford, U.K., 2009.

[43] Lal, S.; Link, S.; Halas, N. J. *Nat. Photon.* **2007**, *1*, 641–648.

[44] Link, S.; El-Sayed, M A. *J. Phys. Chem. B* **1999**, *103*, 8410–8426.

[45] Lee, P. C.; Meisel, D. *J. Phys. Chem.* **1982**, *86*, 3391–3395.

[46] Creighton, J. A.; Blatchford, C. G.; Albrecht, M. G. *J. Chem. Soc. Farad. Trans. II* **1979**, *75*, 790–798.

[47] Ahamed, M.; Karns, M.; Goodson, M.; Rowe, J.; Hussain, S. M.; Schlager, J. J.; Hong, Y. *Toxicol. Appl. Pharmacol.* **2008**, *233*, 404–410.

[48] Durán, N.; Marcato, P. D.; Conti, R. D.; Alves, O. L.; Costa, F. T. M.; Brocchi, M. *J. Braz. Chem. Soc.* **2010**, *21*, 949–959.

[49] Hood, E. *Environ. Health Perspect.* **2004**, *112*, A741–A749.

[50] Wijnhoven, S. W. P.; Peijnenburg, W. J. G. M.; Herberts, C. A.; Hagens, W. I.; Oomen, A. G.; Heugens, E. H. W.; Roszek, B.; Bisschops, J.; Gosens, I.; Van De Meent, D.; Dekkers, S.; De Jong, W. H.; Van Zijverden, M.; Sips, A. J. A. M.; Geertsma, R. E. *Nanotoxicology* **2009**, *3*, 109–138.

[51] Lu, A.- H.; Salabas, E. L.; Schüth, F. *Angew. Chem., Int. Ed.* **2007**, *46*, 1222–1244.

[52] Kim, D. K.; Mikhaylova, M.; Zhang, Y.; Muhammed, M. *Chem. Mater.* **2003**, *15*, 1617–1627.

[53] Laurent, S.; Forge, D.; Port, M.; Roch, A.; Robic, C.; Elst, L. V.; Muller, R. N. *Chem. Rev.* **2008**, *108*, 2064–2110.

[54] Teja, A. S.; Koh P.-Y. *Progress in Crystal Growth and Characterization of Materials* **2009**, *55*, 22–45.

[55] Durán, J. D. G.; Arias, J. L.; Gallardo, V.; Delgado, A. V. *J. Pharm. Sci.* **2008**, *97*, 2948–2983.

[56] Jiles, D. C. *Acta Mater.* **2003**, *51*, 5907–5939.

[57] Bulte, J. W. M.; Kraitchman, D. L. *NMR Biomed.* **2004**, *17*, 484–499.

[58] Shubayev, V. I.; Pisanic, T. R., II; Jin, S. *Adv. Drug Delivery Rev.* **2009**, *61*, 467–477.

[59] Lu, A.- H.; Schmidt, W.; Matoussevitch, N.; Bönnemann, H.; Spliethoff, B.; Tesche, B,; Bill, E.; Kiefer, W.; Schüth F. *Angew. Chem., Int. Ed.* **2004**, *43*, 4303–4306.

[60] Awschalom, D. D.; DiVincenzo, D. P. *Phys. Today* **1995**, *48*, 43–48.

[61] Raj, K.; Moskowitz, R. *J. Magn. Magn. Mater.* **1990**, *85*, 233–245.

[62] Elliott, D . W.; Zhang, W.- X. *Environ. Sci. Technol.* **2001**, *35*, 4922–4926.

[63] Philip, J.; Shima, P. D.; Raj, B. *Appl. Phys. Lett.* **2008**, *92*, 043108(1)–043108(3).

[64] Si, S.; Li, C.; Wang, X.; Yu, D.; Peng, Q.; Li, Y. *Cryst. Growth Des.* **2005**, *5*, 391–393.

[65] Philip, J.; Jaykumar, T.; Kalyanasundaram, P.; Raj, B. *Meas. Sci. Technol.* **2003**, *14*, 1289–1294.

[66] Zhang, C.; Wängler, B.; Morgenstern, B.; Zentgraf, H.; Eisenhut, M.; Untenecker, H.; Krüger, R.; Huss, R.; Seliger, C.; Semmler, W.; Kiessling, F. *Langmuir* **2007**, *23*, 1427–1434.

[67] Tartaj, P.; González-Carreño, T.; Serna, C. J. *Adv. Mater.* **2001**, *13*, 1620–1624.

[68] Xu, Z.; Hou, Y.; Sun, S. *J. Am. Chem. Soc.* **2007**, *129*, 8698–8699.

[69] Zhao, Y. S.; Fu, H. B.; Peng, A.; Ma, Y.; Xiao, D.; Yao, J. *Adv. Mater.* **2008**, *20*, 2859–2876.

[70] Forrest, S. R. *Chem. Rev.* **1997**, *97*, 1793–1896.

[71] Forrest, S. R. *MRS Bull.* **2001**, *26*, 108–112.

[72] Pope, M.; Swenberg, C. E. *Electronic Processes in Organic Crystals*; Clarendon Press: Oxford, 1999; p 78.

[73] Xiao, D.; Xi, L.; Yang, W.; Fu, H.; Shuai, Z.; Fang, Y.; Yao, J. *J. Am. Chem. Soc.* **2003**, *125*, 6740–6745.

[74] Patra, A.; Hebalkar, N.; Sreedhar, B.; Sarkar, M.; Samanta, A.; Radhakrishnan, T. P. *Small* **2006**, *2*, 650–659.

[75] Fu, H.- B.; Yao, J.- N. *J. Am. Chem. Soc.* **2001**, *123*, 1434–1439.

[76] Burda, C.; Chen, X.; Narayanan, R.; El-Sayed, M. A. *Chem. Rev.* **2005**, *105*, 1025–1102.

[77] Kelly, K. L.; Coronado, E.; Zhao, L. L.; Schatz, G. C. *J. Phys. Chem. B* **2003**, *107*, 668–677.

[78] Nizamoglu, S.; Sun, X. W.; Demir, H. V. *Appl. Phys. Lett.* **2010**, *97*, 263106(1)–263106(3).

[79] Basko, D. M.; La Rocca, G. C.; Bassani, F.; Agranovich, V. M. *Phy. Rev. B* **2005**, *71*, 165330(1)–165330(8).

[80] Granqvist, C. G.; Buhrman, R. A. *J. Appl. Phys.* **1976**, *47*, 2200–2219.

[81] Matsui, A.; Mizuno, K.; Nishi, O.; Matsushima, Y.; Shimizu, M.; Goto, T.; Takeshima, M. *Chemical Physics* **1995**, *194*, 167–174.

[82] Kasai, H.; Nalwa, H. S.; Oikawa, H.; Okada, S.; Matsuda, H.; Minami, N.; Kakuta, A.; Ono, K.; Mukoh, A.; Nakanishi, H. *Jpn. J. Appl. Phys.* **1992**, *31*, L1132–L1134.

[83] Katagi, H.; Kasai, H.; Okada, S.; Oikawa, H.; Komatsu, K.; Matsuda, H.; Liu, Z.; Nakanishi,

H. *Jpn. J. Appl. Phys.* **1996**, *35*, L1364–L1366.

[84] Yanagawa, T.; Kurokawa, Y.; Kasai, H.; Nakanishi, H. *Opt. Commun.* **1997**, *137*, 103–106.

[85] Kasai, H.; Kamatani, H.; Okada, S.; Oikawa, H.; Matsuda, H.; Nakanishi, H. *Jpn. J. Appl. Phys.* **1996**, *35*, L221–L223.

[86] Chaudhuri, R. G.; Paria, S. *Chem. Rev.* **2012**, *112*, 2373–2433.

[87] Rodríguez-González, B.; Burrows, A.; Watanabe, M.; Kiely, C. J.; Liz-Marzán, L. M. *J. Mater. Chem.* **2005**, *15*, 1755–1759.

[88] Wang, L.; Luo, J.; Fan, Q.; Suzuki, M.; Suzuki, I. S.; Engelhard, M. H.; Lin, Y.; Kim, N.; Wang, J. Q.; Zhong, C.- J. *J. Phys. Chem. B* **2005**, *109*, 21593–21601.

[89] Lu, W.; Wang, B.; Zeng, J.; Wang, X.; Zhang, S.; Hou, J. G. *Langmuir* **2005**, *21*, 3684–3687.

[90] Peng, X.; Schlamp, M. C.; Kadavanich, A. V.; Alivisatos, A. P. *J. Am. Chem. Soc.* **1997**, *119*, 7019–7029.

[91] Zhang, L.; Blom, D. A.; Wang, H. *Chem. Mater.* **2011**, *23*, 4587–4598.

[92] Clark, H. A.; Campagnola, P. J.; Wuskell, J. P.; Lewis, A.; Loew, L. M. *J. Am. Chem. Soc.* **2000**, *122*, 10234–10235.

[93] Longo, A.; Carotenuto, G.; Palomba, M.; Nicola, S. D. *Polymers* **2011**, *3*, 1794–1804.

[94] De, M.; Ghosh, P. S.; Rotello, V. M. *Adv. Mater.* **2008**, *20*, 4225–4241.

[95] Reddy, L. H.; Arias, J. L.; Nicolas, J.; Couvreur, P. *Chem. Rev.* **2012**, *112*, 5818–5878.

[96] Soppimath, K. S.; Tan, D. C.- W.; Yang, Y.- Y. *Adv. Mater.* **2005**, *17*, 318–323.

[97] Gupta, A. K.; Gupta, M. *Biomaterials* **2005**, *26*, 3995–4021.

[98] Dobson, J. *Drug Dev. Res.* **2006**, *67*, 55–60.

[99] Phadtare, S.; Kumar, A.; Vinod, V. P.; Dash, C.; Palaskar, D. V.; Rao, M.; Shukla, P. G.; Sivaram, S.; Sastry, M. *Chem. Mater.* **2003**, *15*, 1944–1949.

[100] Cheng, Z.; Zhang, L.; Zhu, X.; Kang, E. T.; Neoh, K. G. J. *Polym. Sci., Part A: Polym. Chem.* **2008**, *46*, 2119–2131.

[101] Yang, Z.; Yang, L.; Zhang, Z.; Wu, N.; Xie, J.; Cao, W. *Colloids Surf., A* **2008**, *312*, 113–117.

[102] Moore, L. R.; Zborowski, M.; Nakamura, M.; McCloskey, K.; Gura, S.; Zuberi, M.; Margel, S.; Chalmers, J. J. *J. Biochem. Biophys. Methods* **2000**, *44*, 115–130.

[103] Sung, Y.- M.; Lee, J.- K. *Cryst. Growth Des.* **2004**, *4*, 737–742.

[104] Song, C.; Gu, G.; Lin, Y.; Wang, H.; Guo, Y.; Fu, X.; Hu, Z. *Mater. Res. Bull.* **2003**, *38*, 917–924.

[105] Song, C.; Yang, M.; Wang, D.; Hu, Z. *Mater. Res. Bull.* **2010**, *45*, 1021–1025.

[106] Sun, Y.; Zhou, B.; Gao, P.; Mu, H.; Chu, L. *J. Alloys Compd.* **2010**, *490*, L48–L51.

[107] Caruso, F.; Caruso, R. A.; Möhwald, H. *Science* **1998**, *282*, 1111–1114.

[108] Caruso, R. A.; Susha, A.; Caruso, F. *Chem. Mater.* **2001**, *13*, 400–409.

[109] Fowler, C. E.; Khushalani, D.; Mann, S. *Chem. Commun.* **2001**, 2028–2029.

[110] Park, J.- H.; Oh, C.; Shin, S.- I.; Moon, S.- K.; Oh, S.- G. *J. Colloid Interface Sci.* **2003**, *266*, 107–114.

[111] Park, D.- H.; Kim, J.- E.; Oh, J.- M.; Shul, Y.- G.; Choy, J.- H. *J. Am. Chem. Soc.* **2010**, *132*, 16735–16736.

[112] Kirsch, S.; Doerk, A.; Bartsch, E.; Sillescu, H.; Landfester, K.; Spiess, H. W.; Maechtle, W. *Macromolecules* **1999**, *32*, 4508–4518.

[113] Ni, K. F.; Sheibat-Othman, N.; Shan, G. R.; Fevotte, G.; Bourgeat-Lami, E. *Macromolecules* **2005**, *38*, 9100–9109.

[114] Lu, Y.; Wittemann, A.; Ballauff, M.; Drechsler, M. *Macromol. Rapid Commun.* **2006**, *27*, 1137–1141.

[115] Atanasov, V.; Sinigersky, V.; Klapper, M.; Müllen, K. *Macromolecules* **2005**, *38*, 1672–1683.

[116] Nah, J.- W.; Jeong, Y.- I.; Cho, C.- S. *J. Polym. Sci. B Polym. Phys.* **1998**, *36*, 415–423.

[117] Oldenberg, S. J.; Averitt, R. D.; Westcott, S. L.; Halas, N. J. *Chem. Phys. Lett.* **1998**, *288*, 243–247.

[118] Daniel, M.- C.; Astruc, D. *Chem. Rev.* **2004**, *104*, 293–346.

[119] Caruso, F. *Adv. Mater.* **2001**, *13*, 11–22.

[120] Mukherjee, S.; Sobhani, H.; Lassiter, J. B.; Bardhan, R.; Nordlander, P.; Halas, N. J. *Nano Lett.* **2010**, *10*, 2694–2701.

[121] Balakrishnan, S.; Bonder, M. J.; Hadjipanayis, G. C. *J. Magn. Magn. Mater.* **2009**, *321*, 117–122.

[122] Kim, M.- J.; Chao, Y.- H.; Kim, D. H.; Kim, K. H. *Magnetics, IEEE Transactions on* **2009**, *45*, 2446–2449.

[123] Laurent, S.; Forge, D.; Port, M.; Roch, A.; Robic, C.; Elst, L. V.; Muller, R. N. *Chem. Rev.* **2008**, *108*, 2064–2110.

[124] Salgueiriño-Maceira, V.; Correa-Duarte, M. A. *Adv. Mater.* **2007**, *19*, 4131–4144.

[125] Kortan, A. R.; Hull, R.; Opila, R. L.; Bawendi, M. G.; Steigerwald, M. L.; Carroll, P. J.; Brus, L. E. *J. Am. Chem. Soc.* **1990**, *112*, 1327–1332.

[126] Qi, L.; Ma, J.; Cheng, H.; Zhao, Z. *Colloids Surf., A.* **1996**, *111*, 195–202.

[127] Mews, A.; Eychmüller, A.; Giersig, M.; Schooss, D.; Weller, H. *J. Phys. Chem.* **1994**, *98*, 934–941.

[128] Ma, G. H.; He, J.; Rajiv, K.; Tang, S. H.; Yang, Y.; Nogami, M. *Appl. Phys. Lett.* **2004**, *84*, 4684–4685.

[129] Kamat, P. V.; Shanghavi, B. *J. Phys. Chem. B* **1997**, *101*, 7675–7679.

[130] Scodeller, P.; Flexer, V.; Szamocki, R.; Calvo, E. J.; Tognalli, N.; Troiani, H.; Fainstein, A. *J. Am. Chem. Soc.* **2008**, *130*, 12690–12697.

[131] Babes, L.; Denizot, B.; Tanguy, G.; Le Jeune, J. J.; Jallet, P. *J. Colloid Interface Sci.* **1999**, *212*, 474–482.

[132] De Farias, P. M. A.; Santos, B. S.; Menezes, F. D.; Brasil, A. G., Jr.; Ferreira, R.; Motta, M. A.; Castro-Neto, A. G.; Vieira, A. A. S.; Silva, D. C. N.; Fontes, A.; Cesar, C. L. *Appl. Phys. A: Mater. Sci. Process.* **2007**, *89*, 957–961.

[133] de Menezes, F. D.; Brasil Jr., A. G.; Moreira, W. L.; Barbosa, L. C.; Cesar, C. L.; Ferreira, R.

de C.; de Farias, P. M. A.; Santos, B. S. *Microelectron. J.* **2005**, *36*, 989–991.

[134] Schreder, B.; Schmidt, T.; Ptatschek, V.; Spanhel, L.; Materny, A.; Kiefer, W. *J. Cryst. Growth* **2000**, *214/215*, 782–786.

[135] Zimmer, J. P.; Kim, S.- W.; Ohnishi, S.; Tanaka, E.; Frangioni, J. V.; Bawendi, M. G. *J. Am. Chem. Soc.* **2006**, *128*, 2526–2527.

[136] Dresco, P. A.; Zaitsev, V. S.; Gambino, R. J.; Chu, B. *Langmuir* **1999**, *15*, 1945–1951.

[137] Sounderya, N.; Zhang, Y. *Recent Pat. Biomed. Eng.* **2008**, *1*, 34–42.

[138] Yan, E.; Ding, Y.; Chen, C.; Li, R.; Hu, Y.; Jiang, X. *Chem. Commun.* **2009**, 2718–2720.

[139] Jaiswal, J. K.; Mattoussi, H.; Mauro, J. M.; Simon, S. M. *Nat. Biotechnol.* **2003**, *21*, 47–51.

[140] Michalet, X.; Pinaud, F. F.; Bentolila, L. A.; Tasy, J. M.; Doose, S.; Li, J. J.; Sundaresan, G.; Wu, A. M.; Gambhir, S. S.; Weiss, S. *Science* **2005**, *307*, 538–544.

[141] Kickelbick, G. *Hybrid Materials*; Wiley-VCH: Weinheim, 2007.

[142] Guli, M.; Lambert, E. M.; Li, M.; Mann, S. *Angew. Chem., Int. Ed.* **2010**, *49*, 520–523.

[143] Muskens, O. L.; England, M. W.; Danos, L.; Li, M.; Mann, S. *Adv. Funct. Mater.* **2012**, *23*, 281–290.

[144] Wei, H.; Lu, Y. *Chem. Asian J.* **2012**, *7*, 680–683.

[145] Falkner, J. C.; Turner, M. E.; Bosworth, J. K.; Trentler, T. J.; Johnson, J. E.; Lin, T.; Colvin, V. L. *J. Am. Chem. Soc.* **2005**, *127*, 5274–5275.

[146] Fujiki, Y.; Tokunaga, N.; Shinkai, S.; Sada, K. *Angew. Chem., Int. Ed.* **2006**, *45*, 4764–4767.

[147] Fujiki, Y.; Shinkai, S.; Sada, K. *Cryst. Growth Des.* **2009**, *9*, 2751–2755.

[148] Sindoro, M.; Feng, Y.; Xing, S.; Li, H.; Xu, J.; Hu, H.; Liu, C.; Wang, Y.; Zhang, H.; Shen, Z.; Chen, H. *Angew. Chem., Int. Ed.* **2011**, *50*, 1–6

[149] Corbierre, M. K.; Cameron, N. S.; Sutton, M.; Mochrie, S. G. J.; Lurio, L. B.; Rühm, A.; Lennox, R. B. *J. Am. Chem. Soc.* **2001**, *123*, 10411–10412.

[150] Mejía, M. L.; Agapiou, K.; Yang, X.; Holliday, B. J. *J. Am. Chem. Soc.* **2009**, *131*, 18196–18197.

[151] Sun, Y. G.; Xia, Y. N. *Science* **2002**, *298*, 2176–2179.

[152] Brust, M.; Walker, M.; Bethell, D.; Schiffrin, D. J.; Whyman, R. *J. Chem. Soc., Chem. Commun.* **1994**, 801–802.

[153] Hulteen, J. C.; Treichel, D. A.; Smith, M. T.; Duval, M. L.; Jensen, T. R.; Van Duyne, R. P. *J. Phys. Chem. B* **1999**, *103*, 3854–3863.

[154] Murray, C. B.; Norris, D. J.; Bawendi, M. G. *J. Am. Chem. Soc.* **1993**, *115*, 8706–8715.

[155] Peng, X.; Wilson, T. E.; Alivisatos, A. P.; Schultz, P. G. *Angew. Chem., Int. Ed.* **1997**, *36*, 145–147.

[156] Sun, S. H. *Adv. Mater.* **2006**, *18*, 393–403.

[157] Boal, A. K.; Das, K.; Gray, M.; Rotello, V. M. *Chem. Mater.* **2002**, *14*, 2628–2636.

[158] Caswell, K. K.; Wilson, J. N.; Bunz, U. H. F.; Murphy, C. J. *J. Am. Chem. Soc.* **2003**, *125*, 13914–13915.

[159] Kang, Y. J.; Erickson, K. J.; Taton, T. A. *J. Am. Chem. Soc.* **2005**, *127*, 13800–13801.

[160] DeVries, G. A.; Brunnbauer, M.; Hu, Y.; Jackson, A. M.; Long, B.; Neltner, B. T.; Uzun, O.; Wunsch, B. H.; Stellacci, F. *Science* **2007**, *315*, 358–361.

[161] Nie, Z. H.; Fava, D.; Kumacheva, E.; Zou, S.; Walker, G. C.; Rubinstein, M. *Nat. Mater.* **2007**, *6*, 609–614.

[162] Tang, Z. Y.; Zhang, Z. L.; Wang, Y.; Glotzer, S. C.; Kotov, N. A. *Science* **2006**, *314*, 274–278.

[163] Zhao, N. N.; Liu, K.; Greener, J.; Nie, Z. H.; Kumacheva, E. *Nano Lett.* **2009**, *9*, 3077–3081.

[164] Park, S.; Lim, J.- H.; Chung, S.- W.; Mirkin, C. A. *Science* **2004**, *303*, 348–351.

[165] Nikolic, M. S.; Olsson, C.; Salcher, A.; Kornowski, A.; Rank, A.; Schubert, R.; Frömsdorf, A.; Weller, H.; Förster, S. *Angew. Chem., Int. Ed.* **2009**, *48*, 2752–2754.

[166] Kalsin, A. M.; Fialkowski, M.; Paszewski, M.; Smoukov, S. K.; Bishop, K. J. M.; Grzybowski, B. A. *Science* **2006**, *312*, 420–424.

[167] Nykypanchuk, D.; Maye, M. M.; van der Lelie, D.; Gang, O. *Nature* **2008**, *451*, 549–552.

[168] Park, S. Y.; Lytton-Jean, A. K. R.; Lee, B.; Weigand, S.; Schatz, G. C.; Mirkin, C. A. *Nature* **2008**, *451*, 553–556.

[169] Iacovella, C. R.; Glotzer, S. C. *Nano Lett.* **2009**, *9*, 1206–1211.

[170] Sharma, J.; Chhabra, R.; Cheng, A.; Brownell, J.; Liu, Y.; Yan, H. *Science* **2009**, *323*, 112–116.

[171] Murray, C. B.; Kagan, C. R.; Bawendi, M. G. *Science* **1995**, *270*, 1335–1338.

[172] Motte, L.; Billoudet, F.; Pileni, M.- P. *J. Phys. Chem.* **1995**, *99*, 16425–16429.

[173] Pileni, M.- P. *J. Phys. Chem. B* **2001**, *105*, 3358–3371.

[174] Pileni, M.- P. *J. Phys.: Condens. Matter* **2006**, *18*, S65–S84.

[175] Brust, M.; Bethell, D.; Schiffrin, D. J.; Kiely, C. J. *Adv. Mater.* **1995**, *7*, 795–797.

[176] Harfenist, S. A.; Wang, Z. L.; Alvarez, M. M.; Vezmar, I.; Whetten, R. L. *J. Phys. Chem.* **1996**, *100*, 13904–13910.

[177] Motte, L.; Billoudet, F.; Lacaze, E.; Pileni, M.- P. *Adv. Mater.* **1996**, *8*, 1018–1020.

[178] Whetten, R. L.; Khoury, J. T.; Alvarez, M. M.; Murthy, S.; Vezmar, I.; Wang, Z. L.; Stephens, P. W.; Cleveland, C. L.; Luedtke, W. D.; Landman, U. *Adv. Mater.* **1996**, *8*, 428–433.

[179] Murthy, S.; Wang, Z. L.; Whetten, R. L. *Philos. Mag. Lett.* **1997**, *75*, 321–327.

[180] Korgel, B. A.; Fitzmaurice, D. *Phys. Rev. B: Solid State* **1999**, *59*, 14191–14201.

[181] Bishop, K. J. M.; Wilmer, C. E.; Soh, S.; Grzybowski, B. A. *Small* **2009**, *5*, 1600–1630.

[182] Murugadoss, A.; Kar, M.; Chattopadhyay, A. *J. Colloid Interface Sci.* **2008**, *324*, 230–235.

[183] Shirman, T.; Arad, T.; van der Boom, M. E. *Angew. Chem., Int. Ed.* **2009**, *48*, 1–5.

[184] Ni, W.; Mosquera, R. A.; Pérez-Juste, J.; Liz-Marzán, L. M. *J. Phys. Chem. Lett.* **2010**, *1*, 1181–1185.

[185] Tang, Z.; Kotov, N. A. *Adv. Mater.* **2005**, *17*, 951–962.

[186] Murugadoss, A.; Chattopadhyay, A. *J. Phys. Chem. C* **2008**, *112*, 11265–11271.

[187] Lin, S.; Li, M.; Dujardin, E.; Girard, C.; Mann, S. *Adv. Mater.* **2005**, *17*, 2553–2559.

Bibliography

[188] Si, S.; Kotal, A.; Mandal, T. K. *J. Phys. Chem. C* **2007**,*111*, 1248–1255.

[189] Shipway, A. N.; Katz, E.; Willner, I. *Chem. Phys. Chem.* **2000**, *1*, 18–52.

[190] Nath, N.; Chilkoti, A. *J. Am. Chem. Soc.* **2001**, *123*, 8197–8202.

[191] Kwon, K.- W.; Shim, M. *J. Am. Chem. Soc.* **2005**, *127*, 10269–10275.

[192] Cha, J. N.; Birkedal, H.; Euliss, L. E.; Bartl, M. H.; Wong, M. S.; Deming, T. J.; Stucky, G. D. *J. Am. Chem. Soc.* **2003**, *125*, 8285–8289.

[193] Zheng, N.; Fan, J.; Stucky, G. D. *J. Am. Chem. Soc.* **2006**, *128*, 6550–6551.

[194] Dumestre, F.; Chaudret, B.; Amiens, C.; Renaud, P.; Fejes, P. *Science* **2004**, *303*, 821–823.

[195] Fan, H.; Chen, Z.; Brinker, C. J.; Clawson, J.; Alam, T. *J. Am. Chem. Soc.* **2005**, *127*, 13746–13747.

[196] Murray, C. B.; Kagan, C. R.; Bawendi, M. G. *Annu. Rev. Mater. Sci.* **2000**, *30*, 545–610.

[197] Jańczewski, D.; Tomczak, N.; Liu, S.; Han, M.-Y.; Vancso, G. J. *Chem. Commun.* **2010**, *46*, 3253–3255.

[198] Goubet, N.; Portalès, H.; Yan, C.; Arfaoui, I.; Albouy, P.- A.; Mermet, A.; Pileni, M.- P. *J. Am. Chem. Soc.* **2012**, *134*, 3714–3719.

[199] Rycenga, M.; McLellan, J. M.; Xia, Y. *Adv. Mater.* **2008**, *20*, 2416–2420.

[200] Thomas, K. G.; Barazzouk, S.; Ipe, B. I.; Joseph, S. T. S.; Kamat, P. V. *J. Phys. Chem. B* **2004**, *108*, 13066–13068.

[201] Nie, Z. H.; Fava, D.; Rubinstein, M.; Kumacheva, E. *J. Am. Chem. Soc.* **2008**, *130*, 3683–3689.

[202] Fava, D.; Nie, Z. H.; Winnik, M. A.; Kumacheva, E. *Adv. Mater.* **2008**, *20*, 4318–4322.

[203] Baranov, D.; Fiore, A.; van Huis, M.; Giannini, C.; Falqui, A.; Lafont, U.; Zandbergen, H.; Zanella, M.; Cingolani, R.; Manna, L. *Nano Lett.* **2010**, *10*, 743–749.

[204] Nikoobakht, B.; Wang, Z. L.; El-Sayed, M. A. *J. Phys. Chem. B* **2000**, *104*, 8635–8640.

[205] Dujardin, E.; Hsin, L.- B.; Wang, C. R. C.; Mann, S. *Chem. Commun.* **2001**, 1264–1265.

[206] Nakata, K.; Hu, Y.; Uzun, O.; Bakr, O.; Stellacci, F. *Adv. Mater.* **2008**, *20*, 4294–4299.

[207] Maye, M. M.; Nykypanchuk, D.; Cuisinier, M.; van der Lelie, D.; Gang, O. *Nat. Mater.* **2009**, *8*, 388–391.

[208] Tang, Z.; Kotov, N. A.; Giersig, M. *Science* **2002**, *297*, 237–240.

[209] Liao, J.; Zhang, Y.; Yu, W.; Xu, L.; Ge, C.; Liu, J.; Gu, N. *Colloids Surf., A* **2003**, *223*, 177–183.

[210] Courty, A.; Fermon, C.; Pileni, M.- P. *Adv. Mater.* **2001**, *13*, 254–258.

[211] Courty, A.; Araspin, O.; Fermon, C.; Pileni, M.- P. *Langmuir* **2001**, *17*, 1372–1380.

[212] Courty, A.; Mermet, A.; Albouy, P. A.; Duval, E.; Pileni, M.- P. *Nat. Mater.* **2005**, *4*, 395–398.

[213] Zaitseva, N.; Dai, Z. R.; Leon, F. R.; Krol, D. *J. Am. Chem. Soc.* **2005**, *127*, 10221–10226.

[214] Lisiecki, I.; Albouy, P.- A.; Pileni, M.- P. *Adv. Mater.* **2003**, *15*, 712–716.

[215] Lisiecki, I.; Albouy, P.- A.; Pileni, M.- P. *J. Phys. Chem. B* **2004**, *108*, 20050–20055.

[216] Lu, W.; Liu, Q.; Sun, Z.; He, J.; Ezeolu, C.; Fang, J. *J. Am. Chem. Soc.* **2008**, *130*, 6983–

6991.

[217] Redl, F. X.; Cho, K.- S.; Murray, C. B.; O'Brien, S. *Nature* **2003**, *423*, 968–971.

[218] Zhuang, J.; Wu, H.; Yang, Y.; Cao, Y. C. *J. Am. Chem. Soc.* **2007**, *129*, 14166–14167.

[219] Zhang, L.; Wu, J.; Liao, H.; Hou, Y.; Gao, S. Chem. Commun. **2009**, 4378–4380.

[220] Mirkin, C. A.; Letsinger, R. L.; Mucic, R. C.; Storhoff, J. J. *Nature* **1996**, *382*, 607–609.

[221] Alivisatos, A. P.; Johnsson, K. P.; Peng, X.; Wilson, T. E.; Loweth, C. J.; Bruchez Jr, M. P.; Schultz, P. G. *Nature* **1996**, *382*, 609–611.

[222] Leunissen, M. E.; Christova, C. G.; Hynninen, A.- P.; Royall, C. P.; Campbell, A. I.; Imhof, A.; Dijkstra, M.; van Roij, R.; van Blaaderen, A. *Nature* **2005**, *437*, 235–240.

[223] Li, L.; Wang, Q. *ACS Nano* **2013**, *7*, 3053–3060.

[224] Murugadoss, A.; Pasricha, R.; Chattopadhyay, A. *J. Colloid Interface Sci.* **2007**, *311*, 303–310.

[225] Wang, D.; Xie, T.; Peng, Q.; Li, Y. *J. Am. Chem. Soc.* **2008**, *130*, 4016–4022.

[226] Correa-Duarte, M. A.; Pérez-Juste, J.; Sánchez-Iglesias, A.; Giersig, M.; Liz-Marzán, L. M. *Angew. Chem., Int. Ed.* **2005**, *44*, 4375–4378.

[227] Wang, H.; Lin, W.; Fritz, K. P.; Scholes, G. D.; Winnik, M. A.; Manners, I. *J. Am. Chem. Soc.* **2007**, *129*, 12924–12925.

[228] Zhang, Q. L.; Gupta, S.; Emrick, T.; Russell, T. P. *J. Am. Chem. Soc.* **2006**, *128*, 3898–3899.

[229] Dujardin, E.; Peet, C.; Stubbs, G.; Culver, J. N.; Mann, S. *Nano Lett.* **2003**, *3*, 413–417.

[230] Aldaye, F. A.; Palmer, A. L.; Sleiman, H. F. *Science* **2008**, *321*, 1795–1799.

[231] Warner, M. G.; Hutchison, J. E. *Nat. Mater.* **2003**, *2*, 272–277.

[232] Kinge, S.; Crego-Calama, M.; Reinhoudt, D. N. *ChemPhysChem* **2008**, *9*, 20–42.

[233] Engtrakul, C.; Kim, Y.- H.; Nedeljković, J. M.; Ahrenkiel, S. P.; Gilbert, K. E. H.; Alleman, J. L.; Zhang, S. B.; Mićić, O. I.; Nozik, A. J.; Heben, M. J. *J. Phys. Chem. B* **2006**, *110*, 25153–25157.

[234] Georgakilas, V.; Gournis, D.; Tzitzios, V.; Pasquato, L.; Guldi, D. M.; Prato, M. *J. Mater. Chem.* **2007**, *17*, 2679–2694.

[235] Ryadnov, M. G.; Woolfson, D. N. *J. Am. Chem. Soc.* **2004**, *126*, 7454–7455.

[236] Györvary, E.; Schroedter, A.; Talapin, D. V.; Weller, H.; Pum, D.; Sleytr, U. B. *J. Nanosci Nanotechnol.* **2004**, *4*, 115–120.

[237] Chen, C.- L.; Zhang, P.; Rosi, N. L. *J. Am. Chem. Soc.* **2008**, *130*, 13555–13557.

[238] Seeman, N. C.; *Nature* **2003**, *421*, 427–431.

[239] Li, H.; Park, S. H.; Reif, J. H.; LaBean, T. H.; Yan, H. *J. Am. Chem. Soc.* **2004**, *126*, 418–419.

[240] Wang, G.; Murray, R. W. *Nano Lett.* **2004**, *4*, 95–101.

[241] Niemeyer, C. M.; Simon, U. *Eur. J. Inorg. Chem.* **2005**, 3641–3655.

[242] Pal, S.; Deng, Z.; Ding, B.; Yan, H.; Liu, Y. *Angew. Chem., Int. Ed.* **2010**, *49*, 1–5.

[243] Artemyev, M.; Kisiel, D.; Abmiotko, S.; Antipina, M. N.; Khomutov, G. B.; Kislov, V. V.; Rakhnyanskaya, A. A. *J. Am. Chem. Soc.* **2004**, *126*, 10594–10597.

Bibliography

[244] Dong, L.; Hollis, T.; Connolly, B. A.; Wright, N. G.; Horrocks, B. R.; Houlton, A. *Adv. Mater.* **2007**, *19*, 1748–1751.

[245] Zhang, L.; Eisenberg, A. *Science* **1995**, *268*, 1728–1731.

[246] Tao, A. R.; Huang, J. X.; Yang, P. D. *Acc. Chem. Res.* **2008**, *41*, 1662–1673.

[247] Collier, C. P.; Saykally, R. J.; Shiang, J. J.; Henrichs, S. E.; Heath, J. R. *Science* **1997**, *277*, 1978–1981.

[248] Tao, A.; Sinsermsuksakul, P.; Yang, P. D. *Nat. Nanotech.* **2007**, *2*, 435–440.

[249] Shevchenko, E. V.; Talapin, D. V.; Kotov, N. A.; O'Brien, S.; Murray, C. B. *Nature* **2006**, *439*, 55–59.

[250] Courty, A.; Mermet, A.; Albouy, P. A.; Duval, E.; Pileni, M. P. *Nat. Mater.* **2005**, *4*, 395–398.

[251] Cheng, W. L.; Campolongo, M. J.; Cha, J. J.; Tan, S. J.; Umbach, C. C.; Muller, D. A.; Luo, D. *Nat. Mater.* **2009**, *8*, 519–525.

[252] Böker, A.; He, J.; Emrick, T.; Russell, T. P. *Soft Matter* **2007**, *3*, 1231–1248.

[253] Lin, Y.; Skaff, H.; Emrick, T.; Dinsmore, A. D.; Russell, T. P. *Science* **2003**, *299*, 226–229.

[254] Volinsky, R.; Jelinek, R. *Angew. Chem., Int. Ed.* **2009**, *48*, 4540–4542.

[255] Huang, J. X.; Kim, F.; Tao, A. R.; Connor, S.; Yang, P. D. *Nat. Mater.* **2005**, *4*, 896–900.

[256] Bentzon, M. D.; van Wonterghem, J.; Mørup, S.; Thölen, A.; Koch, C. J. W. *Philos. Mag. B* **1989**, *60*, 169–178.

[257] Bentzon, M. D.; Thölén, A. R. *Ultramicroscopy* **1991**, *38*, 105–115.

[258] Lin, Y.; Skaff, H.; Böker, A.; Dinsmore, A. D.; Emrick, T.; Russell, T. P. *J. Am. Chem. Soc.* **2003**, *125*, 12690–12691.

[259] Böker, A.; Lin, Y.; Chiapperini, K.; Horowitz, R.; Thompson, M.; Carreon, V.; Xu, T.; Abetz, C.; Skaff, H.; Dinsmore, A. D.; Emrick, T.; Russell, T. P. *Nat. Mater.* **2004**, *3*, 302–306.

[260] Zhuang, Z.; Peng, Q.; Zhang, B.; Li, Y. *J. Am. Chem. Soc.* **2008**, *130*, 10482–10483.

[261] Korth, B. D.; Keng, P.; Shim, I.; Bowles, S. E.; Tang, C.; Kowalewski, T.; Nebesny, K. W.; Pyun, J. *J. Am. Chem. Soc.* **2006**, *128*, 6562–6563.

[262] Sheparovych, R.; Sahoo, Y.; Motornov, M.; Wang, S.; Luo, H.; Prasad, P. N.; Sokolov, I.; Minko, S. *Chem. Mater.* **2006**, *18*, 591–593.

[263] Lalatonne, Y.; Richardi, J.; Pileni, M.- P. *Nat. Mater.* **2004**, *3*, 121–125.

[264] Chiang, I- C.; Chen, D.- H. *Adv. Funct. Mater.* **2007**, *17*, 1311–1316.

[265] Tripp, S. L.; Dunin-Borkowski, R. E.; Wei, A. *Angew. Chem., Int. Ed.* **2003**, *42*, 5591–5593.

[266] Held, G. A.; Grinstein, G.; Doyle, H.; Sun, S. H.; Murray, C. B. *Phys. Rev. B* **2001**, *64*, 012408 (1)–012408(4).

[267] Ahniyaz, A.; Sakamoto, Y.; Bergström, L. *Proc. Natl Acad. Sci. USA* **2007**, *104*, 17570–17574.

[268] Hermanson, K. D.; Lumsdon, S. O.; Williams, J. P.; Kaler, E. W.; Velev, O. D. *Science* **2001**, *294*, 1082–1086.

[269] Velev, O. D.; Bhatt, K. H. *Soft Matter* **2006**, *2*, 738–750.

[270] Acharya, S.; Patla, I.; Kost, J.; Efrima, S.; Golan, Y. *J. Am. Chem. Soc.* **2006**, *128*, 9294–9295.

[271] Ryan, K. M.; Mastroianni, A.; Stancil, K. A.; Liu, H. T.; Alivisatos, A. P. *Nano Lett.* **2006**, *6*, 1479–1482.

[272] Gupta, S.; Zhang, Q. L.; Emrick, T.; Russell, T. P. *Nano Lett.* **2006**, *6*, 2066–2069.

[273] Duan, X. F.; Lieber, C. M. *Adv. Mater.* **2000**, *12*, 298–302.

[274] Gong, T. Y.; Marr, D. W. M. *Appl. Phys. Lett.* **2004**, *85*, 3760–3762.

[275] Bechinger, C.; Brunner, M.; Leiderer, P. *Phys. Rev. Lett.* **2001**, *86*, 930–933.

[276] Klajn, R.; Bishop, K. J. M.; Grzybowski, B. A. *Proc. Natl. Acad. Sci. U.S.A.* **2007**, *104*, 10305–10309.

[277] Quinten, M.; Leitner, A.; Krenn, J. R.; Aussenegg, F. R. *Opt. Lett.* **1998**, *23*, 1331–1333.

[278] Ghosh, S. K.; Pal, T. *Chem. Rev.* **2007**, *107*, 4797–4862.

[279] Su, K.- H.; Wei, Q.- H.; Zhang, X.; Mock, J. J.; Smith, D. R.; Schultz, S. *Nano Lett.* **2003**, *3*, 1087–1090.

[280] Chen, C.- F.; Tzeng, S.- D.; Chen, H.- Y.; Lin, K.- J.; Gwo, S. *J. Am. Chem. Soc.* **2008**, *130*, 824–826.

[281] Zhu, M.- Q.; Wang, L.- Q.; Exarhos, G.- J.; Li, A. D. Q. *J. Am. Chem. Soc.* **2004**, *126*, 2656–2657.

[282] Zheng, J. W.; Constantinou, P. E.; Micheel, C.; Alivisatos, A. P.; Kiehl, R. A.; Seeman, N. C. *Nano Lett.* **2006**, *6*, 1502–1504.

[283] Frankamp, B. L.; Boal, A. K.; Rotello, V. M. *J. Am. Chem. Soc.* **2002**, *124*, 15146–15147.

[284] Jain, P. K.; Eustis, S.; El-Sayed, M. A. *J. Phys. Chem. B* **2006**, *110*, 18243–18253.

[285] Kreibeg, U.; Vollmer, M. *Optical Properties of Metal Clusters*; Springer Verlag: New York, 1995; Vol. 25, p 532.

[286] Markovich, G.; Collier, C. P.; Henrichs, S. E.; Remacle, F.; Levine, R. D.; Heath, J. R. *Ann. Chem. Res.* **1999**, *32*, 415–423.

[287] Koole, R.; Liljeroth, P.; Donega, C. D.; Vanmaekelbergh, D.; Meijerink, A. *J. Am. Chem. Soc.* **2006**, *128*, 10436–10441.

[288] Crooker, S. A.; Hollingsworth, J. A.; Tretiak, S.; Klimov, V. I. *Phys. Rev. Lett.* **2002**, *89*, 186802(1) –186802(4).

[289] Lee, J.; Govorov, A. O.; Kotov, N. A. *Nano Lett.* **2005**, *5*, 2063–2069.

[290] Wang, C.- J.; Huang, L.; Parviz, B. A.; Lin, L. Y. *Nano Lett.* **2006**, *6*, 2549–2553.

[291] Tang, Z. Y.; Ozturk, B.; Wang, Y.; Kotov, N. A. *J. Phys. Chem. B* **2004**, *108*, 6927–6931.

[292] Wargnier, R.; Baranov, A. V.; Maslov, V. G.; Stsiapura, V.; Artemyev, M.; Pluot, M.; Sukhanova, A.; Nabiev, I. *Nano Lett.* **2004**, *4*, 451–457.

[293] Zaitseva, N.; Dai, Z. R.; Leon, F. R.; Krol, D. *J. Am. Chem. Soc.* **2005**, *127*, 10221–10226.

[294] Govorov, A. O.; Bryant, G. W.; Zhang, W.; Skeini, T.; Lee, J.; Kotov, N. A.; Slocik, J. M.; Naik, R. R. *Nano Lett.* **2006**, *6*, 984–994.

[295] Lee, J.; Hernandez, P.; Lee, J.; Govorov, A. O.; Kotov, N. A. *Nat. Mater.* **2007**, *6*, 291–295.

[296] Zhang, W.; Govorov, A. O.; Bryant, G. W. *Phys. Rev. Lett.* **2006**, *97*, 146804(1)–146804(4).

[297] Kulakovich, O.; Strekal, N.; Yaroshevich, A.; Maskevich, S.; Gaponenko, S.; Nabiev, I.; Woggon, U.; Artemyev, M. *Nano Lett.* **2002**, *2*, 1449–1452.

[298] Gueroui, Z.; Libchaber, A. *Phys. Rev. Lett.* **2004**, *93*, 166108(1)–166108(4).

[299] Lee, J.; Govorov, A. O.; Dulka, J.; Kotov, N. A. *Nano Lett.* **2004**, *4*, 2323–2330.

[300] Cheng, M.- T.; Liu, S.- D.; Zhou, H.- J.; Hao, Z.- H.; Wang, Q.- Q. *Opt. Lett.* **2007**, *32*, 2125–2127.

[301] Lee, J.; Javed, T.; Skeini, T.; Govorov, A. O.; Bryant, G. W.; Kotov, N. A. *Angew. Chem., Int. Ed.* **2006**, *45*, 4819–4823.

[302] Lu, A.- H.; Salabas, E. L.; Schüth, F. *Angew. Chem., Int. Ed.* **2007**, *46*, 1222–1244.

[303] Pileni, M.- P. *Acc. Chem. Res.* **2007**, *40*, 685–693.

[304] Petit, C.; Russier, V.; Pileni, M.- P. *J. Phys. Chem. B* **2003**, *107*, 10333–10336.

[305] Li, Y.; Zhang, X. L.; Qiu, R.; Kang, Y. S. *J. Ind. Eng. Chem.* **2008**, 14, 22–27.

[306] Lisiecki, I.; Parker, D.; Salzemann, C.; Pileni, M.- P. *Chem. Mater.* **2007**, *19*, 4030–4036.

[307] Lalatonne, Y.; Motte, L.; Russier, V.; Ngo, A. T.; Bonville, P.; Pileni M.- P. *J. Phys. Chem. B* **2004**, *108*, 1848–1854.

[308] Maier, S. A.; Brongersma, M. L.; Kik, P. G.; Meltzer, S.; Requicha, A. A. G.; Atwater, H. A. *Adv. Mater.* **2001**, *13*, 1501–1505.

[309] Ozbay, E. *Science* **2006**, *311*, 189–193.

[310] Maier, S. A.; Kik, P. G.; Atwater, H. A.; Meltzer, S.; Harel, E.; Koel, B. E.; Requicha, A. A. G. *Nat. Mater.* **2003**, *2*, 229–232.

[311] Sanders, A. W.; Routenberg, D. A.; Wiley, B. J.; Xia, Y.; Dufresne, E. R.; Reed, M. A. *Nano Lett.* **2006**, *6*, 1822–1826.

[312] Lee, J.; Govorov, A. O.; Kotov, N. A. *Angew. Chem., Int. Ed.* **2005**, *44*, 7439–7442.

[313] Elghanian, R.; Storhoff, J. J.; Mucic, R. C.; Letsinger, R. L.; Mirkin, C. A. *Science* **1997**, *277*, 1078–1081.

[314] Lee, J.- S.; Han, M. S.; Mirkin, C. A. *Angew. Chem., Int. Ed.* **2007**, *46*, 4093–4096.

[315] Sönnichsen, C.; Reinhard, B. M.; Liphardt, J.; Alivisatos, A. P. *Nat. Biotechnol.* **2005**, *23*, 741–745.

[316] Reinhard, B. M.; Sheikholeslami, S.; Mastroianni, A.; Alivisatos, A. P.; Liphardt, J. *Proc. Natl Acad. Sci. USA* **2007**, *104*, 2667–2672.

[317] Liu, G. L.; Yin, Y.; Kunchakarra, S.; Mukherjee, B.; Gerion, D.; Jett, S. D.; Bear, D. G.; Gray, J. W.; Alivisatos, A. P.; Lee, L. P.; Chen, F. F. *Nat. Nanotech.* 2006, 1, 47–52.

[318] Choi, Y.; Ho, N.- H.; Tung, C.- H. *Angew. Chem., Int. Ed.* **2007**, *46*, 707–709.

[319] Li, H. X.; Rothberg, L. *Proc. Natl Acad. Sci. USA* **2004**, *101*, 14036–14039.

[320] Sudeep, P. K.; Joseph, S. T. S.; Thomas, K. G. *J. Am. Chem. Soc.* **2005**, *127*, 6516–6517.

[321] Brown, L. V.; Sobhani, H.; Lassiter, J. B.; Nordlander, P.; Halas, N. J. *ACS Nano* **2010**, *4*, 819–832.

[322] Yang, Z.- J.; Zhang, Z.- S.; Zhang, W.; Hao, Z.- H.; Wang, Q.- Q. *Appl. Phys. Lett.* **2010**,

96, 131113(1)–131115(3).

[323] Mirin, N. A.; Bao, K.; Nordlander P. *J. Phys. Chem. A* **2009**, *113*, 4028–4034.

[324] Liu, N.; Langguth, L.; Weiss, T.; Kästel, J.; Fleischhauer, M.; Pfau, T.; Giessen, H. *Nat. Mater.* **2009**, *8*, 758–762.

[325] Tassin, P.; Zhang, L.; Koschny, T.; Economou, E. N.; Soukoulis, C. M. *Phys. Rev. Lett.* **2009**, *102*, 053901(1)–053901(4).

[326] Luk′yanchuk, B.; Zheludev, N. I.; Maier, S. A.; Halas, N. J.; Nordlander, P.; Giessen, H.; Chong, C. T. *Nat. Mater.* **2010**, *9*, 707–715.

[327] Nie, S. M.; Emory, S. R. *Science* **1997**, *275*, 1102–1106.

[328] Kneipp, J.; Kneipp, H.; Kneipp, K. *Chem. Soc. Rev.* **2008**, *37*, 1052–1060.

[329] Moskovits, M. *J. Raman Spectrosc.* **2005**, *36*, 485–496.

[330] Graham, D.; Thompson, D. G.; Smith, W. E.; Faulds, K. *Nat. Nanotech.* **2008**, *3*, 548–551.

[331] Hao, E.; Schatz, G. C. *J. Chem. Phys.* **2004**, *120*, 357–366.

[332] Oh, E.; Hong, M.-Y.; Lee, D.; Nam, S.- H.; Yoon, H. C.; Kim, H.- S. *J. Am. Chem. Soc.* **2005**, *127*, 3270–3271.

[333] Tseng, R. J.; Tsai, C. L.; Ma, L. P.; Ouyang, J. Y.; Ozkan, C. S.; Yang, Y. *Nat. Nanotech.* **2006**, *1*, 72–77.

[334] Sun, S. H.; Murray, C. B.; Weller, D.; Folks, L.; Moser, A. *Science* **2000**, *287*, 1989–1992.

[335] Hoinville, J.; Bewick, A.; Gleeson, D.; Jones, R.; Kasyutich, O.; Mayes, E.; Nartowski, A.; Warne, B.; Wiggins, J.; Wong, K. *J. Appl. Phys.* **2003**, *93*, 7187–7189.

[336] Bao, J.; Chen, W.; Liu, T.; Zhu, Y.; Jin, P.; Wang, L.; Liu, J.; Wei, Y.; Li, Y. *ACS Nano* **2007**, *1*, 293–298.

[337] Abu-Reziq, R.; Wang, D.; Post, M.; Alper, H. *Adv. Synth. Catal.* **2007**, *349*, 2145–2150.

[338] Gopalakrishnan, G.; Danelon, C.; Izewska, P.; Prummer, M.; Bolinger, P.- Y.; Geissbhler, I.; Demurtas, D.; Dubochet, J.; Vogel, H. *Angew. Chem., Int. Ed.* **2006**, *45*, 5478–5483.

[339] Zebli, B.; Susha, A. S.; Sukhorukov, G. B.; Rogach, A. L.; Parak, W. J. *Langmuir* **2005**, *21*, 4262–4265.

[340] Skirtach, A. G.; Javier, A. M.; Kreft, O.; Köhler, K.; Alberola, A. P.; Möhwald, H.; Parak, W. J.; Sukhorukov, G. B. *Angew. Chem., Int. Ed.* **2006**, *45*, 4612–4617.

[341] Peer, D.; Karp, J. M.; Hong, S. P.; Farokhzad, O. C.; Margalit, R.; Langer, R. *Nat. Nanotech.* **2007**, *2*, 751–760.

[342] Cao, Y. W.; Jin, R.; Mirkin, C. A. *J. Am. Chem. Soc.* **2001**, *123*, 7961–7962.

[343] Liz-Marzán, L. M.; Giersig M.; Mulvaney, P. *Langmuir* **1996**, *12*, 4329–4335.

[344] Shi, W.; Zeng, H.; Sahoo, Y.; Ohulchanskyy, T. Y.; Ding, Y.; Wang, Z. L.; Swihart, M.; Prasad, P. N. *Nano Lett.* **2006**, *6*, 875–881.

[345] Reimer, L. *Transmission electron microscopy:Physics of image formation and microanalysis*; Springer-Verlag Press: Berlin, Heidelberg, New York, Tokyo, 1993; pp. 431–463.

[346] Schmid, G. *Clusters and Colloids: From Theory to Applications*; Wiley-VCH: Weinheim, 1994; p 506.

Bibliography

[347] Rodríguez-Lorenzo, L.; Romo-Herrera, J. M.; Pérez-Juste, J.; Alvarez-Puebla, R. A.; Liz-Marzán, L. M. *J. Mater. Chem.* **2011**, *21*, 11544–11549.

[348] Rodríguez-Fernández, J.; Pérez-Juste, J.; Mulvaney, P.; Liz-Marzán, L. M. *J. Phys. Chem. B* **2005**, *109*, 14257–14261.

[349] Sahoo, A. K.; Sk, M. Palashuddin; Ghosh, S. S.; Chattopadhyay, A. *Nanoscale* **2011**, *3*, 4226–4233.

[350] Sahoo, A. K.; Sharma, S.; Chattopadhyay, A.; Ghosh, S. S. *Nanoscale* **2012**, *4*, 1688–1694.

[351] Connor, E. E.; Mwamuka, J.; Gole, A.; Murphy, C. J.; Wyatt, M. D. *Small* **2005**, *1*, 325–327.

[352] Leonov, A. P.; Zheng, J.; Clogston, J. D.; Stern, S. T.; Patri, A. K.; Wei, A. *ACS Nano* **2008**, *2*, 2481–2488.

[353] Otsukaa, H.; Nagasaki, Y.; Kataoka, K. *Adv. Drug Deliv. Rev.* **2003**, *55*, 403–419.

[354] Susumu, K.; Mei, B. C.; Mattoussi, H. *Nat. Protoc.* **2009**, *4*, 424–436.

[355] Nicol, M. J.; Fleming, C.; Paul, R. A. *The Chemistry of the Extraction of Gold.* South African Institute of Mining and Metallurgy, The Extractive Metallurgy of Gold in South Africa. 1987; Vol. 2, pp. 831-905.

[356] Kellum, J. A.; Elbers, P. *WG Stewart's Textbook of Acid-Base.*; AcidBase.org/Paul: WG Elbers, Amsterdam, The Netherlands, 2009, pp. 68-69.

[357] Farrar, Jr., G. E.; Bower, R. J. *Annu. Rev. Physiol.* **1967**, *29*, 141–168.

[358] Haisa, M.; Kashino, S.; Kawai, R.; Maeda, H. *Acta Cryst. B* **1976**, *32*, 1283–1285.

[359] Haisa, M.; Kashino, S.; Maeda, H. *Acta Cryst. B* **1974**, *30*, 2510–2512.

[360] Lin, S.; Li, M.; Dujardin, E.; Girard, C.; Mann, S. *Adv. Mater.* **2005**, *17*, 2553–2559.

[361] Han, D. H.; Wang, J. P.; Luo, H. L. *J. Magn. Magn. Mater.* **1994**, *136*, 176–182.

[362] Collier, C. P.; Vossmeyer, T.; Heath J. R. *Annu. Rev. Phys. Chem.* **1998**, *49*, 371–404.

[363] Erb, R. M.; Libanori, R.; Rothfuchs, N.; Studart, A. R. *Science* **2012**, *335*, 199–204.

[364] Kodama, R. H.; Berkowitz, A. E.; McNiff, Jr., E. J.; Foner, S. *Phys. Rev. Lett.* **1996**, *77*, 394–397.

[365] Shulga, O. V.; Jefferson, K.; Khan, A. R.; D'Souza, V. T.; Liu, J.; Demchenko, A. V.; Stine, K. J. *Chem. Mater.* **2007**, *19*, 3902–3911.

[366] Min, Y. J.; Akbulut, M.; Kristiansen, K.; Golan, Y.; Israelachvili, J. *Nat. Mater.* **2008**, *7*, 527–538.

[367] Zhang, Z. L.; Glotzer, S. C. *Nano Lett.* **2004**, *4*, 1407–1413.

[368] Balazs, A. C. *Annu. Rev. Phys. Chem.* **2007**, *58*, 211–233.

Publications

1. Das, S.; Murugadoss, A.; Sarkar, S.; Chattopadhyay, A. *J. Chem. Sci.* **2008**, *120*, 547–555.
2. Das, S.; Sahoo, A. K.; Ghosh, S. S.; Chattopadhyay, A. *Langmuir* **2010**, *26*, 15714–15717.
3. Das, S.; Chattopadhyay, A. *RSC Advances* **2012**, *2*, 10245–10250.
4. Das, S.; Paul, A.; Chattopadhyay, A. *Nanoscale* **2013**, *5*, 9247–9254.
5. Das, S.; Dutta, A.; Chattopadhyay, A. **2013** (To be submitted)

RSC | Advancing the Chemical Sciences

Royal Society of Chemistry
Thomas Graham House
Science Park
Milton Road
Cambridge
CB4 0WF

Tel: +44 (0)1223 420 066
Fax: +44 (0)1223 423 623
Email: contracts-copyright@rsc.org

www.rsc.org

Acknowledgements to be used by RSC authors

Authors of RSC books and journal articles can reproduce material (for example a figure) from the RSC publication in a non-RSC publication, including theses, without formally requesting permission providing that the correct acknowledgement is given to the RSC publication. This permission extends to reproduction of large portions of text or the whole article or book chapter when being reproduced in a thesis.

The acknowledgement to be used depends on the RSC publication in which the material was published and the form of the acknowledgements is as follows:

- For material being reproduced from an article in *New Journal of Chemistry* the acknowledgement should be in the form:
  - [Original citation] - Reproduced by permission of The Royal Society of Chemistry (RSC) on behalf of the Centre National de la Recherche Scientifique (CNRS) and the RSC
- For material being reproduced from an article *Photochemical & Photobiological Sciences* the acknowledgement should be in the form:
  - [Original citation] - Reproduced by permission of The Royal Society of Chemistry (RSC) on behalf of the European Society for Photobiology, the European Photochemistry Association, and RSC
- For material being reproduced from an article in *Physical Chemistry Chemical Physics* the acknowledgement should be in the form:
  - [Original citation] - Reproduced by permission of the PCCP Owner Societies
- For material reproduced from books and any other journal the acknowledgement should be in the form:
  - [Original citation] - Reproduced by permission of The Royal Society of Chemistry

The acknowledgement should also include a hyperlink to the article on the RSC website.

The form of the acknowledgement is also specified in the RSC agreement/licence signed by the corresponding author.

Except in cases of republication in a thesis, this express permission does not cover the reproduction of large portions of text from the RSC publication or reproduction of the whole article or book chapter.

A publisher of a non-RSC publication can use this document as proof that permission is granted to use the material in the non-RSC publication.

Order Completed

Thank you very much for your order.

This is a License Agreement between Subhojit Das ("You") and Springer ("Springer"). The license consists of your order details, the terms and conditions provided by Springer, and the payment terms and conditions.

Get the printable license.

License Number	3266630910416
License date	Nov 12, 2013
Licensed content publisher	Springer
Licensed content publication	Journal of Chemical Sciences
Licensed content title	p-Aminoacetanilide mediated formation of assembly of Au nanoparticles
Licensed content author	Subhojit Das
Licensed content date	Jan 1, 2008
Volume number	120
Issue number	6
Type of Use	Thesis/Dissertation
Portion	Full text
Number of copies	1
Author of this Springer article	Yes and you are a contributor of the new work
Title of your thesis / dissertation	Inorganic-Organic Hybrid Nanocrystalline Materials in Zero to Three Dimensions
Expected completion date	Nov 2013
Estimated size(pages)	120
Total	0.00 USD

CLOSE WINDOW

Copyright Clearance Center RightsLink®

Home Account Info Help

ACS Publications High quality. High impact.

Title: Plasmonic Signatures in the Composite Crystals of Gold Nanoparticles and p-Hydroxyacetanilide (Paracetamol)

Author: Subhojit Das, Amaresh Kumar Sahoo, Siddhartha Sankar Ghosh, and Arun Chattopadhyay

Publication: Langmuir

Publisher: American Chemical Society

Date: Oct 1, 2010

Logged in as:
Subhojit Das

LOGOUT

PERMISSION/LICENSE IS GRANTED FOR YOUR ORDER AT NO CHARGE

This type of permission/license, instead of the standard Terms & Conditions, is sent to you because no fee is being charged for your order. Please note the following:

- Permission is granted for your request in both print and electronic formats, and translations.
- If figures and/or tables were requested, they may be adapted or used in part.
- Please print this page for your records and send a copy of it to your publisher/graduate school.
- Appropriate credit for the requested material should be given as follows: "Reprinted (adapted) with permission from (COMPLETE REFERENCE CITATION). Copyright (YEAR) American Chemical Society." Insert appropriate information in place of the capitalized words.
- One-time permission is granted only for the use specified in your request. No additional uses are granted (such as derivative works or other editions). For any other uses, please submit a new request.

BACK CLOSE WINDOW

TH-1220_07612221